Methodologies for Virtual Sensing Applied to Aeronautical and Ship Structures

Francesco Saltari

Department of Mechanical and Aerospace Engineering
Sapienza University of Rome

Advisors:
Prof. Franco Mastroddi
Prof. Daniele Dessi

A dissertation submitted in fulfillment of the requirements for the degree of
Doctor of Philosophy in Aeronautical and Space Engineering

February 14th, 2019

[Page intentionally left blank]

A chi rende la vita
meno amara

Abstract

In this thesis the problem of achieving a full, experimentally based, representation of the load and elastic deflection response of aeronautical and ship structures is concerned by the development of numerical procedures and their assessment via related experimental activities. The objective is to provide reliable estimations of elastic deflections and external forces throughout the structure using noisy pointwise measurements. This issue is critical for some important structural engineering applications such as Structural Health Monitoring and Condition-Based Maintenance.

The most important tools generally used for this purpose (*e.g*, Kalman filter) have been first reviewed, pointing strengths and critical issues out. Then, an approach based on an optimal second-order natural observer has been proposed also integrating this with signal processing approaches like discrete wavelet transform and finite-element component analysis approaches like dynamics condensation. The developed and integrated numerical framework was finally applied to the state estimation of two specific structures, namely, an aircraft and surface vessel operating under unsteady environmental conditions featured by wind gust or sea waves, respectively. More in detail, a scaled physical model of a fast catamaran, tested in the towing-tank, and a numerical model of a flexible aircraft were studied as significant test cases for assessing the introduced methodologies. Both the structures involved are interesting in their respective research fields.

The accurate and complete estimation of the structural dynamics behavior of the fast catamaran is particularly interesting since in real world it might be exposed to critical slamming phenomena on the wetdeck region. The experimental set-up and in particular the choice of the structural measurements were crucial to have a minimum but reliable database for the reconstruction of the structural deflection field. By applying the above methodologies, it was also possible to provide a deeper insight relative to violent fluid-structure interaction phenomena and to evaluate possible fatigue-life reduction for components where direct monitoring was not possible.

The other case study consists of an aircraft research model that experiences a particular kind of instability involving both aeroelasticity and flight dynamics. In such aeronautical application, the structural measurements are virtually obtained by means of simulations based on a flight dynamics and aeroelasticity toolbox developed for the present purpose and featured by an accurate description of the coupling caused by aerodynamic and inertial forces. This case has been performed to investigate numerically the technique proposed in this thesis by integrating the methodology with multi-resolution analysis.

Contents

List of Figures

List of Tables

Nomenclature

Latin symbols

$\mathbf{a}$ = absolute acceleration

A = state matrix

B = input-to-state matrix

D = modal damping matrix

$\check{\mathsf{D}}$ = nodal damping matrix

D_{cb} = Craig-Bampton damping matrix

d_r = *r-th* modal damping

$\mathcal{E}$ = elastic energy

e = state error with only displacements

$\mathbf{f}$ = force per unit volume

f = unknown modal forces

f_r = *r-th* unknown modal force

$FRAC_{\diamond\bullet}$ = frequency response assurance criterion between $\diamond$ and $\bullet$

G = state-to-output matrix

h_r = *r-th* mode response function

H_{S} = Structural (modal) response matrix

H_{O} = Observation response matrix

J = input-to-output matrix

K = modal stiffness matrix

$\check{\mathsf{K}}$ = nodal stiffness matrix

K_{cb} = Craig-Bampton stiffness matrix

k_r = *r-th* modal stiffness

L = observer gain matrix applied to second order equation (*i.e.*, the gain of second order observer)

$\check{\mathsf{L}}$ = observer gain matrix applied to kinematic equation

$\bar{\mathsf{L}}$ = observer gain matrix of first order observer

M = modal mass matrix

$\check{\mathsf{M}}$ = nodal mass matrix

M_{cb} = Craig-Bampton mass matrix

m_r = *r-th* modal mass

N_{dof} = number of nodal DoFs

N_q = number of modes

p = vector of nodal DoFs

p_M = master DoFs
p_k = *k-th* component of p
P = covariance of state error
q = modal coordinates vector
q_cb = Craig-Bampton coordinates vector
q_r = *r-th* modal coordinate
Q = process noise covariance matrix
r = residual measurements vector
r_s = residual vector of stored measurements
E = measurement noise covariance matrix
S = condensed selection matrix
$\mathsf{S}_a, \mathsf{S}_v, \mathsf{S}_d$ = output selection matrices of accelerations, velocities and displacements
t = time
$\mathbf{T}$ = stress tensor
$\mathcal{T}$ = kinetic energy
$TRAC_{\diamond\bullet}$ = time response assurance criterion between $\diamond$ and $\bullet$
u = input vector
$\bar{\mathsf{u}}$ = unknown input vector
$\mathbf{u}_\mathsf{E}$ = elastic displacement
U = covariance matrix between process and measurement noise
$\mathbf{v}$ = absolute velocity
v = measurement noise
w = process noise
w_r = *r-th* component of w
W_o = observability Gramian
$\mathbf{x}$ = absolute position in deformed configuration
$\mathring{\mathbf{x}}$ = absolute position in undeformed configuration
x = state vector
y = output vector
$\mathsf{z}^{(r)}$ = *r-th* eigenvector
Z = modal eigenvector matrix
Z_I = boundary modes matrix
Z_S = fixed-boundary modes matrix
Z_cb = Craig-Bampton transformation matrix

Greek symbols

δ_{rs} = Kronecker delta
ε = state error with only displacements
ε_{f} = force error
η = fixed-boundary modes Lagrangian coordinates vector
λ = vector of design variables
ω_r = *r-th* natural angular frequency
ρ = material density
ξ^{α} = material coordinates
$\breve{\boldsymbol{\varphi}}^{(r)}$ = *r-th* tent shape function
$\boldsymbol{\varphi}^{(r)}$ = *r-th* modal shape function
$\boldsymbol{\varphi}_{\mathsf{cb}}^{(r)}$ = *r-th* Craig-Bampton shape function
$\Phi_{\bullet\bullet}$ = Power spectral density matrix of $\bullet$
$\Sigma_{\bullet\bullet}$ = Covariance matrix of $\bullet$
Ξ_a, Ξ_v, Ξ_d = diagonal matrices weighting accel., vel. and displ. measurements
$\Lambda_a, \Lambda_v, \Lambda_d$ = diagonal matrices weighting state estimation w.r.t. accel., vel. and displ. measurements

Operators

$\frac{D}{Dt}(\bullet)$ = absolute time derivative
$\mathrm{div}(\bullet)$ = divergence
$\diamond * \bullet$ = convolution product

Subscripts

$(\bullet)_e$ = equilibrium quantity

Superscripts

$(\bullet)^{RM}$ = residual modes quantity
$(\bullet)^{[a]}$ = partition w.r.t. acceleration measurements of the matrix/vector $\bullet$
$(\bullet)^{[v]}$ = partition w.r.t. velocity measurements of the matrix/vector $\bullet$
$(\bullet)^{[d]}$ = partition w.r.t. displacement measurements of the matrix/vector $\bullet$

Stacking symbols

$\breve{\bullet}$ = quantities associated to nodal DoFs

$\hat{\bullet}$ = estimation of $\bullet$

$\tilde{\bullet}$ = Fourier/Laplace transform of $\bullet$

Acronyms

FE, FEM = Finite Element, Finite Element Method

DoF, DoFs = Degree of Freedom, Degrees of Freedom

SHM = Structural Health Monitoring

PSD = Power Spectral Density

KF = Kalman Filter

WMRA, MRA = Wavelet Multi-Resolution Analysis, Multi-Resolution Analysis

Introductory remarks

The virtual sensing problem

The topic of the present thesis is closely concerned to the problem of transportation safety. Although addressed on aeronautical and marine vehicles, the thesis aims at providing the technological tools for enhancing the Structural Health Monitoring (SHM) strategies for a wider range of engineering sectors, such as automotive, energy production facilities and civil buildings. The main social challenge is to reduce as much as possible fatalities that can cause the loss of human life by monitoring the structure and identifying the presence of an anomalous behavior before the failure occurs. Both in the aeronautical and ship engineering field, enormous efforts are underway to improve the prevention tools and to reduce the number of incidents year by year, thus reducing the number of victims and/or the economic consequences that an accident causes.

Structural Health Monitoring thus denotes a new engineering field which includes all the non-destructive methodologies, that point to monitor the health of the structure in real time rather than performing periodic inspections. In particular, the missions concerning the SHM are *i)* warning about exceeding the maximum loads that can be admissible from the structure under certain conditions, thus requiring guidance actions; *ii)* providing an estimate of the damage accumulated by the structure during its operative lifetime in order to optimize maintenance strategies and *iii)* providing, if possible, an estimate of any damage on the structure in terms of identification, location and extension in order to predict the timing of maintenance. For this purpose we distinguish between: local identification techniques, based on the modification of mechanical properties detectable by arrays of sensors present in the area affected by the damage and global identification approaches that look for consequences at a general level, such as vibration-based methods [1].

Vibration-based methods are characterized by the presence of sensors spread throughout the structure, all contributing together to the estimation of changes in the localized mechanical behavior of the structure. However, these methods are validated and easy to apply only to non-complex 1D or 2D structures. When the topology of the structure starts to get complicated these methods are generally inaccurate.

When dealing with vibration-based SHM of complex structures such as aircrafts or ships (but even bridges and wind turbines), the lack of information that can lead to wrong estimation of the position and the severity of the damage is one of main issues. The thesis tries to contribute positively to the above mentioned issue (see Fig. 1): it aims at expanding the set of data necessary to develop SHM strategies. The research field that aims at expansion of data from experimental measurements (knowing the physical variables where they are not measured) is generally referred as *virtual sensing*. Thus, an accurate estimation of elastic deflections and internal and external loads throughout the structure can lead to:

- an enhancement in the estimation of fatigue life reduction as it is based on virtual measurements of the stress tensor field; an application based on a fast catamaran case study will be illustrated in this dissertation;
- an improvement in the position and severity prediction of the damage that represents the next step beyond this thesis activity.

For this purpose, in this thesis an approach based on hybrid model, that is, the combination of the mathematical model and the experimentally collected data, is carried out. Thus, it is necessary a numerical model of the structure representing its topology and its mechanical properties, and, consequently, a toolbox able to integrate the measurements collected with the information available from the numerical model. This can be done in principle by means of several strategies, including interpolation of data, modal filters or state observers. The system state, generally made up by a set of Lagrangian coordinates (and, in case, their time-derivatives), represents the minimum information basis that can be considered to describe the behavior of the structure under consideration at different levels of detail (based on the number of states considered). Subsequently, the shape functions obtainable from the numerical model allow expanding at any point of the structure the information condensed in the state estimation. It is thus possible to estimate the external loads, displacements, the stress and strain field, and the elastic energy density at each point. Through these reconstructions, it is therefore possible to support and enhance the several methodologies proposed in structural monitoring literature.

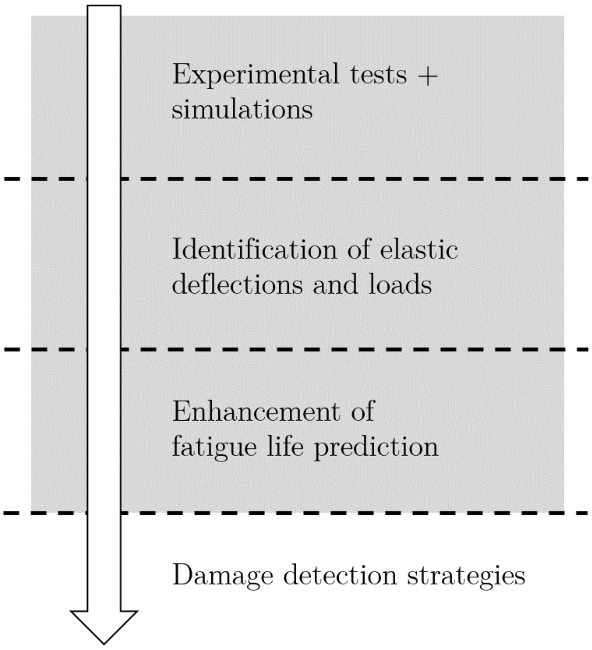

Figure 1: State of the work and future perspective scheme.

Literature review

The problem of virtual sensing has been much debated in recent years and is still an open problem. The aim is to optimize the quality and quantity of information on the structural behavior that can be achieved through a limited number of measurements. With respect to the present literature analysis it must be considered that some methods that are applicable for certain types of structure may not be for other types that operate in different environments.

The more information is given to the observer, the more accurate the estimate will be. On the contrary, the less information you have the more the problem is challenging. In order to understand this concept, let us consider the example concerning the knowledge of external forces, under the assumption of having an accurate numerical model. Indeed, methods that use direct knowledge of external forces provide better estimates than the methods in which external forces are completely unknown. However,even if the force input is unknown, some minimal information can be provided. There are therefore methods that assign a covariance to the external forces or a power spectral density (PSD). Each structure is excited in a specific way, and, net of the effectiveness of each method, the type of observer suitable for each structure must depend on the type of information provided. Note that in the aircraft and ship cases, there are spectral statistical models that describe the environment in terms of turbulence and oceanic waves, respectively based on the informations that are provided to the state observer, all the methods below are summarized in Tab. 1.

Furthermore, the virtual sensing methodology must be supported by a good sensor placement strategy. This last problem, however, is not addressed in the work of this thesis, but may help the development of the proposed methodologies.

The first approach possible to virtual sensing consists of the interpolation of data by means of appropriate shape functions. However, this method is not applicable when the topology of the structure is complex and its application is relevant only when dealing with beams or plates.

The problem of virtual sensing of complex structures has traditionally been addressed through modal filters [2, 3]. Although optimal sensor placement can aid to capture an adequate amount of information by reducing the problem of leakage and spatial aliasing, this is not very robust when system order and measurement noise increase. From this, different approaches have been inferred aimed at improving the estimation of the displacement and load fields.

Avitabile and Pingle [4] presented a methodology based on the SEREP reduction method. The goal was to provide an estimate of the stress and strain field on wind turbines. The displacement data obtained from patches and targets used, respectively, for digital image correlation and dynamic photogrammetry were used to expand the displacement field over the entire structure. The use of a direct SEREP method has some drawbacks due to the least squares numerical approximation carried out to explicit the unmeasured degrees of freedom, and above all, no control on measurement and process noise. Kullaa [5] applied dynamic substructuring to estimate the displacement field throughout the structure. A dynamic condensation was used where displacement measurements were applied on the structure interfaces enabling to estimate the displacement on a numerical case study of plane frame and a vehicle crane. Albeit this procedure avoids the least-square approximation, again it doesn't consider the effects of the process and measurement noises.

Hwang et al. [6] proposed the use of Kalman filter to estimate modal elastic deflections. The state vector used for the estimate was made up by modal coordinates and velocities. Subsequently, the virtually estimated modal coordinates were used to estimate wind loads on a numerical case study of five-story building. Papadimitriou et al. [7] proposed to predict fatigue-life reduction of metallic structures by using the stress field obtained by means of Kalman filter.

Lourens et al. [8] introduced the augmented Kalman filter. In this work, the state vector to be estimated by means of Kalman filter was augmented with the external forces that, in this way, were directly estimated. From the dynamic modelling point of view, these external forces, though unknown, were provided of a random walk dynamics with an own process noise. Naets et al. [9] suggested the use of dummy measurements to avoid drift whenever only accelerations were used.

Relying on the work of Gillijns and De Moor [10], Lourens et al. [11] proposed to use a joint input-response estimation to estimate at the same time the state (made up by modal coordinates and velocities) and the input to the system. The joint input-response estimation exploits an algorithm similar to Kalman filter that, besides the steps of *measurement update* and *time update* considers a further step of *input estimation*. In this step the input is recursively estimated by means of an unbiased minimum-variance process. Practically, the input is estimated by linear combination of the measurements by considering a gain matrix that minimizes the error of the prediction of input. One of the limits of this approach is that it can be used only in the situation where the measured quantities are accelerations. The stated advantage of this methodology is that there is no prior information to be provided on the statistics of external forces. However, as it will be shown in Sec. 1.2.1 all the methods that exploit Kalman filtering are not natural for second order system, such as the structural systems [12]. This is an application limit that is revealed when unknown external forces are dominant with respect to process and measurement noises. In this case the natural relationship of derivation between the estimation of modal velocities and modal coordinates is lost.

To this end, Balas [12] proposed a first order observer that, besides to make the state error converge, pursues also to make converge the naturality of the observation process in a relative finite time. Hashemipour et al. [13] readapted the Kalman filter formulation to second order systems. Belvin [14] presented a method of estimation of dynamic states for feedback control of structural systems. The observation of the state, which includes also additional states to integrate accelerometer measurements, is performed by synthesizing the state observer by means of pole placement. Demetriou [15] presented a natural second order observer that utilizes a parameter-dependent Lyapunov function to ensure the asymptotic convergence of the state error. Demetriou [16] adapted the formulation of the unknown input observer for second-order systems. The formulation aims to fault detection of mechanical systems. Azad et al. [17] proposed an observer-type H_∞ filter designed for structural systems.

Hernandez [18] presented a second-order natural observer based on velocity measurements. The peculiarities of this observer rely on that it is synthesized by expressing the error dynamics in frequency domain, although it works in time-domain. This increases the capability of the proposed observer since the statistics of measurement and process noise are not considered by means of covariance matrices as in Kalman filter, but they are defined directly in frequency domain. This feature, that is not particularly stressed in the paper, can help the observation of systems when dealing with structural problems that are intrinsically featured by their frequency domain behavior. The main drawback consists in the synthesis of the observer that must be designed through an optimization problem that may involve several design variables. In [19], Hernandez directly implemented the observer in a finite element framework, whereas Erazo and Hernandez [20] validated experimentally the approach by means of a cantilever test beam.

Methodology

The thesis work falls among the methods of structural health monitoring and presents methodologies to obtain an optimal observer able to reconstruct the load and elastic deflection field of structural systems. The aim is to yield much more tailored state observers for structural dynamics problems, providing the second-order observers of some extensions that make them more customizable according to the user's engineering sensitivity and the interested structural problem.

The state estimators most used in literature obtain the estimates by condensing the precious information of the different frequency behavior of the external forces and the measurements into normal distributions. These features, that are good for systems in which external forces are known and dominant with respect to process and measurement noises, do not make these types of observers appealing for processes in which external forces are generally unknown and, above all, have a well defined frequency content.

On the other hand, the methodology presented in this thesis uses the power spectral density of external loads for state estimation. The description of the ambient loads is thus provided through the identification of the power spectral densities obtainable by performing experimental tests and/or numerical simulations. This information is then integrated into a complex numerical framework that combines output from finite element models even with the power spectral densities of measurement and process noise to synthesize an optimal observer in accordance with the formulation in [18] by means of an appropriate optimization process. The observer obtained is then applied to the current experimental measurements to provide an estimate of the generalized coordinates (the state of the system) for each time instant.

Nevertheless, two main improvements of the formulation in [18] are proposed:

- the use of the *measurements stored* in a foregoing stage to the observer synthesis to enhance the observation capabilities and yield the state observer adaptive with the stored measurements. This observer will be referred as *learning phase driven observer*. Here, it is worth noticing that these measurement data could belong to a set of sensors that are no longer installed on the structure;

- the use of *wavelet multi-resolution analysis* (WMRA) [21] to decompose the state observation in a multi-scale problem and synthesize the state observer for each specific scale. Splitting the signal out in different scales means that we can express the signal by means of a summation of different contributions each having a different frequency content. This method can be performed in real time and allows designing a *multi-scale observer*. Similar applications have been performed in [22] by applying WMRA to design a frequency-band adaptive controller.

The extensions have been applied to two different case studies, that are, *i)* an *experimental* scaled model of a surface vessel and *ii)* a *numerical* model of flexible aircraft. These application cases are chosen based on the complementary training of the three years of doctoral activity, specially in naval experimental testing through the partecipation in experimental campaigns in towing-tank and in theoretical/numerical apects of integrated modeling of flight dynamics and aeroelasticity that provided the tools to perform virtual tests in aeronautical field. Although it is recommended to start with a numerical model rather than an experimental model, in this case it was decided to privilege an increasing order of the complexity of the proposed methods rather than of the applications.

The surface vessel is a *fast catamaran* that experiences critical slamming phenomena. This model, that is built with the technique of segmented model with continuous backbone, presents concentrated forces at the interfaces between the backbone and the hulls that make helpful the use of different Lagrangian coordinates rather than the modal-ones. In particular the dynamic condensation (also known as Craig-Bampton reduction [23]) was used for this end.

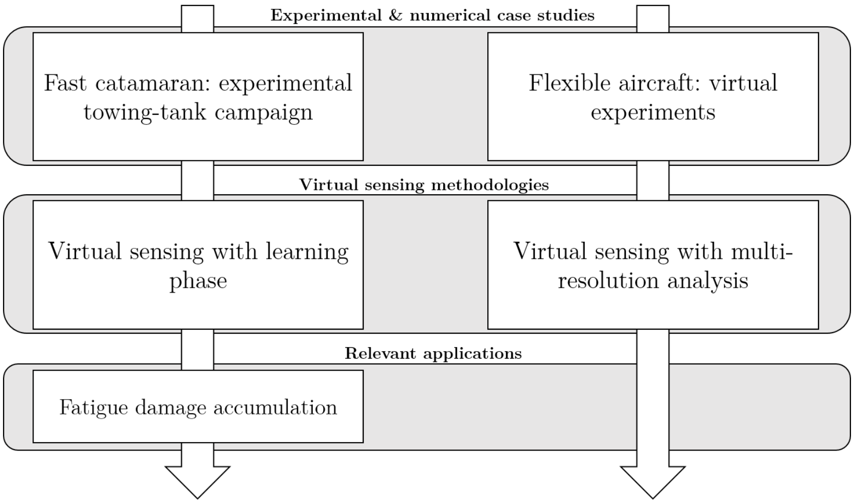

Figure 2: Thesis flowchart.

For this type of application we rely on the first proposed extension, namely, the learning-phase-driven observer. The results provide an estimate of the concentrated forces and space-continuous displacements of the structure in the time-frequency domain to underline some typical behaviors of the ship structures that can be highlighted through an accurate estimate of the elastic deflections. Three different trials in different sea conditions have been considered to assess the state observation. In this regard, it is highlighted how the methodology provides important scientific informations on the behavior of the structure and its response to the slamming phenomena [24].

Subsequently, the stress field obtained has been used to evaluate the reduction of fatigue life at any point of the structural frame for each of the considered trial cases. Even if applied to a structure that experiences loads not leading to fatigue damage during its use in towing tank, it gives the areas of the structure comparatively most exposed to fatigue in the considered test conditions. Therefore, this procedure has the potential to improve the estimation of fatigue life reduction of vessel structures where the internal loads are of a greater order of magnitude. [25].

The numerical aeronautical model is freely inspired by Lockheed Martin X56-a *Body Freedom Flutter* [26], that is, a experimental aircraft used to study a specific kind of instabilities that involves the first bending mode of the wings with the short period mode. The problem of estimating elastic deflections is a current study problem for flutter control of this type of aircraft [3]. This model has been tested to validate the multi-scale observer.

Thesis outline

The thesis is organized as follows:

In Chap. 1 the theoretical background concerning the numerical modeling of structural systems and the methods generally used in literature to observe their dynamics are introduced and discussed. Specially, the modeling of structural dynamic system through a general finite element theory is provided. Then, virtual sensing traditional formulations are introduced, thus pointing out advantages and application limits.

Chap. 2 describes the methodology in depth. First of all, the toolbox necessary for the virtual sensing of the structural dynamics is introduced together with the practical issues to be overcome. Subsequently the declared extensions of second order observer are proposed concerning precisely the use of data recorded during the learning phase and the use of multi-resolution analysis.

In Chap. 3, it is performed the first application concerning the estimation of loads and deflections of a fast catamaran scaled model, by applying the state observer synthesized by using experimental recorded data. The Chapter includes also a sensitivity analysis on the number of sensors involved.

In Chap. 4, the numerical case study will be illustrated concerning the estimation of elastic deflections of a flexible aircraft obtained by virtual experiments. The observation is performed by using the multi-scale observer.

In Appendix A the theoretical background on wavelet multi-resolution analysis will be illustrated.

In appendix B the theoretical development of a method that aims at providing an optimal estimation of the external forces is introduced.

In appendix C an application on fatigue life reduction is presented for the experimental catamaran case study.

In appendix D the integrated modeling of aeroelasticity and flight dynamics used to generate data for the flexible aircraft virtual experiment is explained.

Methods	Natural	*Is the Input known?*	Prior statistics			References
			measurement noise	process noise	unknown forces	
Modal filters	Yes	No	No	No	No	[2, 3]
Reduction/expansion (SEREP, Guyan, Dynamic condensation)	Yes	No	No	No	No	[4, 5]
Kalman filter	No	Yes	Covariance	Covariance	No	[6, 7]
Augmented Kalman filter	No	No	Covariance	Covariance	Covariance (of the derivative of forces)	[8, 9]
Joint input-state estimation	No	No	Covariance	Covariance	No	[10, 11]
Unknown input second-order observer	Yes	No	No	No	No	[16]
Other second order observers	Yes	No	Yes	Covariance	Covariance	[12, 13, 14, 15, 17]
Second order observer with frequency domain synthesis	Yes	No	PSD	PSD	PSD	[18, 19, 20]

Table 1: Virtual sensing strategies in literature.

Chapter 1

Theoretical issues on structural dynamics systems and their state observers

The approach developed in this thesis to assess the structural behavior of ship and aeronautical structures is based on advanced concepts from structural dynamics and the theory of state observers. This toolbox allows for the development of the required numerical procedures which implement the present approach. The chapter is organized as follows: Sec. 1.1 refers to the main useful notions related to Finite Element Analysis, that is, the numerical tool used to generate an *a priori* knowledge of the structures being objects of the present thesis, along with reduced order modeling; Sec. 1.2 reviews the optimal state observers.

1.1 Numerical modeling

The aim of this thesis is to perform the estimation of the loads and elastic deflection field for aircrafts and ships. To this end, we need to introduce the concepts related to continuous-space elastic displacements and external forces. Denoting with $\xi^\alpha (\alpha = 1, 2, 3)$ the material coordinates of the structure and with $\mathbf{x}(\xi^\alpha, t)$ and $\mathring{\mathbf{x}}(\xi^\alpha)$, respectively, the actual and initial positions of the material point, it is possible to express the displacements of the material point at each instant t as

$$\mathbf{u}_{\mathsf{E}}(\xi^\alpha, t) = \mathbf{x}(\xi^\alpha, t) - \mathring{\mathbf{x}}(\xi^\alpha) \tag{1.1}$$

The elastic continuum is featured by the principles of conservation of mass and momentum that lead to the well-known *Cauchy equations of motion*:

$$\rho \frac{\mathrm{D}\mathbf{v}}{\mathrm{D}t} = \mathrm{div}(\mathbf{T}) + \rho \mathbf{f} \tag{1.2}$$

where $\frac{\mathrm{D}\bullet}{\mathrm{D}t}$ indicates the material derivative symbol, $\mathbf{v}$ is the material derivative of $\mathbf{u}_\mathsf{E}$, $\mathbf{T}$ is the stress tensor and $\mathbf{f}$ are the volume forces. Because of the complexity of such structures, the discretization into finite element (FE) model is the only way forward. With FE model we pursue to describe as best as possible the true structure, identifying the numerical model as its virtual twin. In FE description, the structure is discretized into a certain number of nodes and elements. Discretizing by means of finite elements means assume a set of Lagrangian coordinates $\mathsf{p} = [p_1 \cdots p_k \cdots p_{N_{dof}}]^\mathsf{T}$ able to reconstruct the elastic deflection field as follows:

$$\mathbf{u}_\mathsf{E}(\xi^\alpha, t) = \sum_{k=1}^{N_{dof}} p_k(t) \breve{\boldsymbol{\varphi}}^{(k)}(\xi^\alpha) \tag{1.3}$$

where $\breve{\boldsymbol{\varphi}}^{(k)}(\xi^\alpha)$ is generally a space-dependent tent function that coincides with elastic deflection field when only p_k is non null. According with the kind of discretization (*e.g.* solid, shell, linear elements or concentrated mass), the Lagrangian coordinates p_k, namely the DoFs of the FE model, assume the meaning of physical displacements and rotations of the nodes. Consequently, the field associated to external forces $\mathbf{f}$ is given by:

$$\mathbf{f}(\xi^\alpha, t) = \sum_{k=1}^{N_{dof}} \breve{f}_k \breve{\boldsymbol{\varphi}}^{(k)}(\xi^\alpha) \tag{1.4}$$

where $\breve{f}_k$ are nodal forces. It is worth recalling that, while the nodes provide the DoFs to reconstruct the displacement field, the elements which are defined assuming the nodes at the corners, elaborate the density and the constitutive laws to get the mass, damping and stiffness properties of the structure. In this way, the discretization of the structure into finite elements allows to get a detailed picture of the structure in terms of static and dynamic behavior. An example of discretization in finite elements is illustrated in Fig. 1.1. The figure shows the scaled catamaran (namely, one of the case study of the present thesis). The elements that form the structure are characterized by user assigned properties such as, for instance, the definition of material and the thickness of the shell elements.

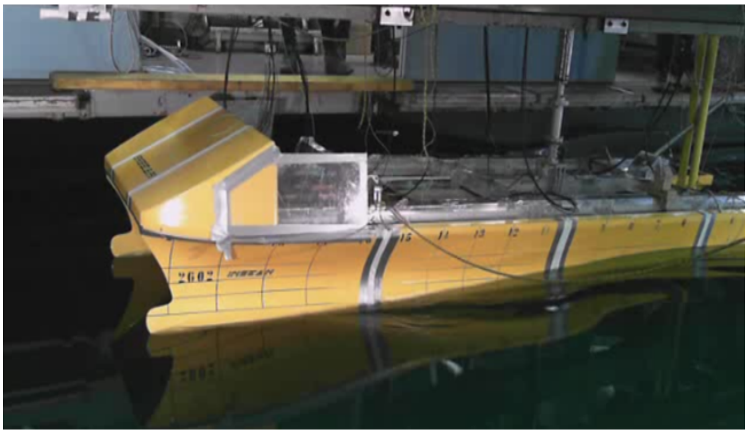

(a) Experimental model

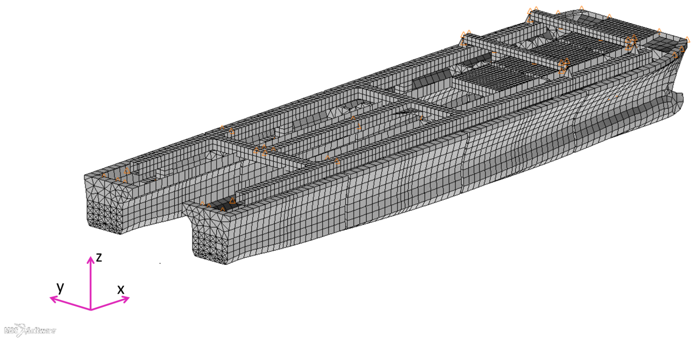

(b) Finite element model

Figure 1.1: Scaled catamaran: experimental and numerical models.

The FE analysis, by means of a weak form procedure and considering the stress tensor split up in a conservative portion depending on the material deformations and non-conservative one depending on velocity of deformation, provides a description of the structure in terms of mass $\breve{\mathsf{M}}$, damping $\breve{\mathsf{D}}$ and stiffness $\breve{\mathsf{K}}$ matrices

$$\breve{\mathsf{M}}\ddot{\mathsf{p}} + \breve{\mathsf{D}}\dot{\mathsf{p}} + \breve{\mathsf{K}}\mathsf{p} = \breve{\mathsf{f}} + \breve{\mathsf{w}} \qquad \mathsf{p}(0) = \mathsf{p}_0,\ \dot{\mathsf{p}}(0) = \dot{\mathsf{p}}_0 \tag{1.5}$$

where p is the vector of nodal degrees of freedom (displacements and rotations according to the FE modelling, *i.e.*, $p_k \quad k = 1, ..., N_{dof}$), whereas $\breve{\mathsf{f}}$ is the vector collecting the external forces on each DoF and $\breve{\mathsf{w}}$ is the process noise. The challenge of the present work is not providing simulations in numerical environments, but dealing with the real structures. The process noise $\breve{\mathsf{w}}$ is already introduced in order to consider any kind of uncertainties with respect to real structure to be investigated.

The measurements concerning the structural behavior of the structure are data arrays that depend on structural dynamics. In this section, without considering the internal dynamics of the sensors we can state that this data can always be expressed as a function of the displacement field, and, in turn, of the Lagrangian coordinates. For instance, consider the specific material point $\bar{\xi}^{\alpha}$. If we install a displacement sensor about it (*e.g.* a potentiometer), we assume that the output $y(t_k)$ at the specific time t_k is expressed as the projection of $\mathbf{u}_{\mathsf{E}}(\bar{\xi}^{\alpha}, t_k)$ along the axis of the sensor represented with the versor $\mathbf{g}(\bar{\xi}^{\alpha})$ of the local reference system. In this way, a dependency of the measurements from the Lagrangian coordinates is obtained as:

$$y(t_k) = \mathbf{u}_{\mathsf{E}}(\bar{\xi}^{\alpha}, t_k) \cdot \mathbf{g}(\bar{\xi}^{\alpha}) = \sum_{n=1}^{N_{dof}} p_n(t_k) \breve{\boldsymbol{\varphi}}^{(n)}(\bar{\xi}^{\alpha}) \cdot \mathbf{g}(\bar{\xi}^{\alpha}) \tag{1.6}$$

This equation mathematically expresses a displacement measure. However, similar expressions can be derived to consistently express any type of structural output including accelerations and strains. Hence, generalizing the concept above, the outputs can be expressed according to the DoFs of FE model:

$$\mathsf{y} = \breve{\mathsf{S}}_a \ddot{\mathsf{p}} + \breve{\mathsf{S}}_v \dot{\mathsf{p}} + \breve{\mathsf{S}}_d \mathsf{p} + \breve{\mathsf{v}} \tag{1.7}$$

where $\breve{\mathsf{S}}_a$, $\breve{\mathsf{S}}_v$ and $\breve{\mathsf{S}}_d$ are the selection matrices able to express the measurements by means of vector p and its derivatives (*e.g.* accelerometer and strain gage data can be expressed, respectively, as a function of $\breve{\mathsf{S}}_a$ and $\breve{\mathsf{S}}_d$) and $\breve{\mathsf{v}}$ is the measurement noise. To understand the meaning of the selection matrices above, it is worth to notice that in presence of strain gage measurements, $\breve{\mathsf{S}}_d$ would assume the meaning of finite difference between the displacements and rotations of the element nodes involved.

If the structure has a linear behavior, $\breve{\mathsf{M}}$ and $\breve{\mathsf{K}}$ are symmetric. Moreover, defined as

$$\mathcal{T} = \frac{1}{2}\dot{\mathsf{p}}^{\mathsf{T}}\breve{\mathsf{M}}\dot{\mathsf{p}} > 0 \qquad \forall \dot{\mathsf{p}} \neq \mathsf{0} \tag{1.8a}$$

$$\mathcal{E} = \frac{1}{2}\mathsf{p}^{\mathsf{T}}\breve{\mathsf{K}}\mathsf{p} \geq 0 \qquad \forall \mathsf{p} \neq \mathsf{0} \tag{1.8b}$$

respectively, the kinetic and elastic energy, it is possible to state that $\breve{\mathsf{M}}$ is positive definite matrix whereas $\breve{\mathsf{K}}$ is a semi-positive definite matrix.

The problem in Eq. 1.5 is associated to the well-known *eigenproblem* such that:

$$\breve{\mathsf{K}}\mathsf{z}^{(r)} = \omega_r^2 \breve{\mathsf{M}}\mathsf{z}^{(r)} \tag{1.9}$$

where ω_r and $\mathsf{z}^{(r)}$ are, respectively, the *r-th* natural frequency and eigenvector. It can be demonstrated that ω_r is always real and, that the eigenvectors ensure the following relationships [1]:

$$\mathsf{z}^{(r)\mathsf{T}}\breve{\mathsf{K}}\mathsf{z}^{(s)} = k_r\delta_{rs} \tag{1.10a}$$

$$\mathsf{z}^{(r)\mathsf{T}}\breve{\mathsf{M}}\mathsf{z}^{(s)} = m_r\delta_{rs} \tag{1.10b}$$

$$\mathsf{z}^{(r)\mathsf{T}}\breve{\mathsf{D}}\mathsf{z}^{(s)} = d_r\delta_{rs} \tag{1.10c}$$

Hence, by means of the eigenproblem and defining q_r $(r = 1, ..., N_{dof})$ the set of generalized modal coordinates, it is possible to express p as

$$\mathsf{p} = \sum_{r=1}^{N_{dof}} \mathsf{z}^{(r)} q_r \tag{1.11}$$

and, thus, obtain a decoupled set of equations such that

$$m_r\ddot{q}_r + d_r\dot{q}_r + k_r q_r = f_r + w_r \qquad q_r(0) = q_{r0},\ \dot{q}_r(0) = \dot{q}_{r0} \tag{1.12}$$

where the modal force and noise are expressed as follows:

$$f_r = \mathsf{z}^{(r)} \cdot \breve{\mathsf{f}} \tag{1.13a}$$

$$w_r = \mathsf{z}^{(r)} \cdot \breve{\mathsf{w}} \tag{1.13b}$$

In this respect the load and elastic deflection fields associated to the vibration modes

---

[1] where the simplifying assumption of Rayleigh or modal damping has been considered [27]:

$$d_r = \frac{\alpha}{2\omega_r} + \frac{2\omega_r}{\beta} \qquad \text{if Rayleigh damping}$$

$$d_r = 2\xi_r m_r \omega_r \qquad \text{if modal damping}$$

where α and β are the coefficients of Rayleigh model whereas ξ_r is the *r-th* damping ratio of the modal damping model.

can be expressed as

$$\mathbf{u}_{\mathsf{E}}(\xi^\alpha, t) = \sum_{r=1}^{N_{dof}} q_r(t)\boldsymbol{\varphi}^{(r)}(\xi^\alpha) \tag{1.14a}$$

$$\mathbf{f}(\xi^\alpha, t) = \sum_{r=1}^{N_{dof}} f_r(t)\boldsymbol{\varphi}^{(r)}(\xi^\alpha) \tag{1.14b}$$

where the vibration mode shape functions $\boldsymbol{\varphi}^{(r)}$ are expressed as linear combination of the tent functions $\breve{\boldsymbol{\varphi}}^{(k)}$ expressed in Eq. (1.3) in the following way:

$$\boldsymbol{\varphi}^{(r)}(\xi^\alpha) = \sum_{k=1}^{N_{dof}} \breve{\boldsymbol{\varphi}}^{(k)}(\xi^\alpha) z_k^{(r)} \tag{1.15}$$

It is worth to introduce here the *driven response* problem in frequency domain.

$$\tilde{q}_r = \tilde{h}_r(\omega)\Big(\tilde{f}_r + \tilde{w}_r\Big) \tag{1.16}$$

where the symbol $\tilde{\bullet}$ is used to represent the Fourier transform, and, subsequently, $\tilde{h}_r(\omega)$ is the frequency response function of the *r-th* mode defined as

$$\tilde{h}_r(\omega) = \Big(-\omega^2 m_r + i\omega d_r + k_r\Big)^{-1} \tag{1.17}$$

By introducing $h_r(t)$ as the inverse transform of $\tilde{h}_r(\omega)$, the driven response in time domain is provided by the following convolution product:

$$q_r(t) = h_r(t) * (f_r + w_r) = \int_0^t h_r(t-\tau)(f_r(\tau) + w_r(\tau))\mathrm{d}\tau \tag{1.18}$$

The number of equations in Eq. (1.18) necessary to describe the structural dynamics of discretized structures is theoretically equal to the number of degrees of freedom of the problem. However, although the number of DoFs of a FE model is highly influenced by the discretization, the number of DoFs of a sufficiently refined model is still too high for the aim of force and elastic deflections estimation. This well-known issue can be solved by reducing the problem size and finding a reduced basis of generalized coordinates able to get the best picture possible of structural behavior.

1.1.1 Reduced order modeling

Modal truncation

Modal truncation techniques over finite-element analysis is usually the way to obtain a computationally cost-effective model. When the structural behavior of interest is limited in a certain frequency band, it is possible to consider just a limited number of modes. Firstly, the user should spot the frequency range of interest. Usually, the choice is made upon the frequency range of the external forces. Then, relying on the expected frequency response as in Eq. (1.17), one can think to truncate the summation in Eq. (1.11) to those modes that should not be excited. Hence, the following modal transformation allows to get the diagonal mass, stiffness and damping matrices along with a new description of the selection matrices expressed as a function of the generalized modal coordinates:

$$\mathsf{Z}^{\mathsf{T}}\breve{\mathsf{M}}\mathsf{Z} = \mathsf{M} \qquad (1.19a) \qquad\qquad \breve{\mathsf{S}}_a\mathsf{Z} = \mathsf{S}_a \qquad (1.20a)$$

$$\mathsf{Z}^{\mathsf{T}}\breve{\mathsf{K}}\mathsf{Z} = \mathsf{K} \qquad (1.19b) \qquad\qquad \breve{\mathsf{S}}_v\mathsf{Z} = \mathsf{S}_v \qquad (1.20b)$$

$$\mathsf{Z}^{\mathsf{T}}\breve{\mathsf{D}}\mathsf{Z} = \mathsf{D} \qquad (1.19c) \qquad\qquad \breve{\mathsf{S}}_d\mathsf{Z} = \mathsf{S}_d \qquad (1.20c)$$

where

$$\mathsf{Z} = \begin{bmatrix} \mathsf{z}^{(1)} & \cdots & \mathsf{z}^{(r)} & \cdots & \mathsf{z}^{(N_q)} \end{bmatrix} \qquad (1.21)$$

and N_q is the number of modes considered to reduce the problem size. In this case Z is usually a rectangular matrix. Therefore, M,D and K are diagonal matrices with size $N_q \times N_q$. It follows:

$$\mathsf{p} = \mathsf{Z}\mathsf{q} + \mathsf{p}^{RM} \qquad (1.22a)$$

$$\mathsf{f} = \mathsf{Z}^{\mathsf{T}}\breve{\mathsf{f}} \qquad (1.22b)$$

$$\mathsf{w} = \mathsf{Z}^{\mathsf{T}}\breve{\mathsf{w}} \qquad (1.22c)$$

where p^{RM} is the displacements due to residual modes dynamics [2] and f and w are

---

[2] The dynamics of residual modes is described as follows:

$$\mathsf{p}^{RM} = \sum_{r=N_q+1}^{N_{dof}} \mathsf{z}^{(r)} q_r$$

modal forces and process noise. Thus, it is possible to rearrange Eqs. (1.5,1.7) by means of truncated modal transformation [3]

$$\begin{aligned} \mathsf{M}\ddot{\mathsf{q}} + \mathsf{D}\dot{\mathsf{q}} + \mathsf{K}\mathsf{q} &= \mathsf{f} + \mathsf{w} \\ \mathsf{y} &= \mathsf{S}_a\ddot{\mathsf{q}} + \mathsf{S}_v\dot{\mathsf{q}} + \mathsf{S}_d\mathsf{q} + \mathsf{v} \end{aligned} \tag{1.23}$$

where v includes also effects owing to modal truncation.

$$\mathsf{v} = \breve{\mathsf{v}} + \breve{\mathsf{S}}_a\ddot{\mathsf{p}}^{RM} + \breve{\mathsf{S}}_v\dot{\mathsf{p}}^{RM} + \breve{\mathsf{S}}_d\mathsf{p}^{RM} \tag{1.24}$$

Therefore, reduction of order size results in an increase of measurement noise. In particular, it means that the useful signal of y can be considered in a frequency band lower than ω_{N_q}. Now it is possible to introduce the frequency response function matrix:

$$\tilde{\mathsf{H}}_S(\omega) = [-\omega^2\mathsf{M} + i\omega\mathsf{D} + \mathsf{K}]^{-1} = \begin{bmatrix} \tilde{h}_1(\omega) & & \\ & \ddots & \\ & & \tilde{h}_{N_q}(\omega) \end{bmatrix} \tag{1.25}$$

along with impulsive response of the structural system:

$$\mathsf{H}_S(t) = \mathfrak{F}^{-1}\{\tilde{\mathsf{H}}_S(\omega)\} = \begin{bmatrix} h_1(t) & & \\ & \ddots & \\ & & h_{N_q}(t) \end{bmatrix} \tag{1.26}$$

In a similar way, we introduce an uncommon operator that assort in frequency

---

[3] Pre-multiplying Eq.(1.5) with the transpose of Z we get:

$$\mathsf{Z}^{\mathsf{T}}\left(\breve{\mathsf{M}}\ddot{\mathsf{p}} + \breve{\mathsf{D}}\dot{\mathsf{p}} + \breve{\mathsf{K}}\mathsf{p} = \breve{\mathsf{f}} + \breve{\mathsf{w}}\right)$$

that, considering the above modal expansion can be written as follows:

$$\mathsf{M}\ddot{\mathsf{q}} + \mathsf{D}\dot{\mathsf{q}} + \mathsf{K}\mathsf{q} + \mathsf{Z}^{\mathsf{T}}\breve{\mathsf{M}}\ddot{\mathsf{p}}^{RM} + \mathsf{Z}^{\mathsf{T}}\breve{\mathsf{D}}\dot{\mathsf{p}}^{RM} + \mathsf{Z}^{\mathsf{T}}\breve{\mathsf{K}}\mathsf{p}^{RM} = \mathsf{f} + \mathsf{w}$$

Being the residual modes orthogonal to the considered modes the following quantities are null:

$$\mathsf{Z}^{\mathsf{T}}\breve{\mathsf{M}}\ddot{\mathsf{p}}^{RM} = \mathsf{Z}^{\mathsf{T}}\breve{\mathsf{D}}\dot{\mathsf{p}}^{RM} = \mathsf{Z}^{\mathsf{T}}\breve{\mathsf{K}}\mathsf{p}^{RM} = 0$$

domain the selection matrices S_a, S_v and S_d:

$$\tilde{\mathsf{S}}(\omega) = -\omega^2 \mathsf{S}_a + i\omega \mathsf{S}_v + \mathsf{S}_d \tag{1.27}$$

namely, a frequency-condensed state-to-output matrix, whose its inverse transform is defined as $\mathsf{S}(t) = \mathfrak{F}^{-1}(\tilde{\mathsf{S}})$ such that:

$$\mathsf{y} = \mathsf{S}(t) * \mathsf{q} + \mathsf{w} \tag{1.28}$$

Dynamic condensation

The dynamic condensation, also known as Craig-Bampton method [23], is a technique that allows for reduction of the number of degrees of freedom p of a structural problem if the dynamic response is limited to a certain frequency range. This method differs from the modal truncation by the capability to include physical displacements in the set of generalized coordinates; this provides a set of reduced DoFs on which the decomposition depends, which are called *master* and hereafter denoted by p_M. Besides the master DoFs, an additional set of modal DoFs η is considered to complete structural dynamics behavior in the interest frequency range. By taking into account this reduction technique, the physical DoFs p can be expressed by superimposition as:

$$\begin{aligned} \mathsf{p} &= \begin{Bmatrix} \mathsf{p}_\mathsf{M} \\ \mathsf{p}_\mathsf{S} \end{Bmatrix} = \begin{Bmatrix} \mathsf{p}_\mathsf{M} \\ \mathsf{Z}_\mathsf{I}\mathsf{p}_\mathsf{M} + \mathsf{Z}_\mathsf{S}\eta + \mathsf{p}_\mathsf{S}^{(RM)} \end{Bmatrix} \\ &= \begin{bmatrix} \mathsf{I} & 0 \\ \mathsf{Z}_\mathsf{I} & \mathsf{Z}_\mathsf{S} \end{bmatrix} \begin{Bmatrix} \mathsf{p}_\mathsf{M} \\ \eta \end{Bmatrix} + \begin{Bmatrix} 0 \\ \mathsf{p}_\mathsf{S}^{(RM)} \end{Bmatrix} = \mathsf{Z}_\mathsf{cb} \begin{Bmatrix} \mathsf{p}_\mathsf{M} \\ \eta \end{Bmatrix} + \begin{Bmatrix} 0 \\ \mathsf{p}_\mathsf{S}^{(RM)} \end{Bmatrix} \end{aligned} \tag{1.29}$$

where Z_cb is the Craig-Bampton transformation matrix. The dynamics of the slave DoFs p_S depends on the *master* DoFs by means of the *boundary modes* Z_I obtained by a static condensation, as well as the dynamics associated to the *fixed-boundary modes* Z_S. There are several reasons why one could use Craig-Bampton reduction. Generally, in aerospace design, this technique is used to enable the partition of models into superelements, allowing the reduction of computational cost for the analyses whenever only some parts of the structure are under process, and, thus, the separation of the design stage between multiple offices.

For the present aim, Craig-Bampton technique is used as a smart tool to provide a suitable description of the external forces by using as Master DoFs those where concentrated loads at interfaces are exchanged. In fact, if only concentrated forces are present on the substructure of interest, we can consider the forcing terms of the master DoFs as interface forces. Then, a user dependent number of fixed-boundary modes is considered in order to have also a displacement span complete enough for the interest frequency range. Thus, the transformation matrix in Eq. (1.29) allows to get a reduced order system whose dynamic behavior is described by the following mass and stiffness matrices:

$$\mathsf{M}_{\mathsf{cb}} = \begin{bmatrix} \breve{\mathsf{M}}_{\mathsf{MM}} + \mathsf{Z}_{\mathsf{I}}^{\mathsf{T}}\breve{\mathsf{M}}_{\mathsf{SS}}\mathsf{Z}_{\mathsf{I}} & \mathsf{Z}_{\mathsf{I}}^{\mathsf{T}}\breve{\mathsf{M}}_{\mathsf{SS}}\mathsf{Z}_{\mathsf{S}} \\ \mathsf{Z}_{\mathsf{S}}^{\mathsf{T}}\breve{\mathsf{M}}_{\mathsf{SS}}\mathsf{Z}_{\mathsf{I}} & \mathsf{I} \end{bmatrix} \qquad \mathsf{K}_{\mathsf{cb}} = \begin{bmatrix} \breve{\mathsf{K}}_{\mathsf{MM}} + \breve{\mathsf{K}}_{\mathsf{MS}}\mathsf{Z}_{\mathsf{I}} & 0 \\ 0 & \Omega_{\mathsf{S}} \end{bmatrix}$$

The second order linear dynamic system can be expressed as follows:

$$\mathsf{M}_{\mathsf{cb}}\ddot{\mathsf{q}}_{\mathsf{cb}} + \mathsf{D}_{\mathsf{cb}}\dot{\mathsf{q}}_{\mathsf{cb}} + \mathsf{K}_{\mathsf{cb}}\mathsf{q}_{\mathsf{cb}} = \mathsf{f}_{\mathsf{cb}} + \mathsf{w}_{\mathsf{cb}} \tag{1.30}$$

where $\mathsf{q}_{\mathsf{cb}}^{\mathsf{T}} = \left\{\mathsf{p}_{\mathsf{M}}^{\mathsf{T}} \quad \eta^{\mathsf{T}}\right\}$ is the vector of the reduced generalized coordinates, D_{cb} is the structural damping matrix [4] expressed by means of Craig-Bampton modes, f_{cb} is the vector of the external forces and w_{cb} is the process noise [5].

Similarly to the modal transformation, also in this case it is possible to reconstruct the load and deflection fields by means of physical mode shapes $\boldsymbol{\varphi}_{\mathsf{cb}}^{(r)}$ associated to this Lagrangian coordinates:

$$\mathbf{u}_{\mathsf{E}}(\xi^{\alpha}, t) = \sum_{r=1}^{N_{dof}} q_{\mathsf{cb}_r}(t)\boldsymbol{\varphi}_{\mathsf{cb}}^{(r)}(\xi^{\alpha}) \tag{1.31a}$$

$$\mathbf{f}(\xi^{\alpha}, t) = \sum_{r=1}^{N_{dof}} f_{\mathsf{cb}_r}(t)\boldsymbol{\varphi}_{\mathsf{cb}}^{(r)}(\xi^{\alpha}) \tag{1.31b}$$

---

[4] The damping matrix D_{cb} is rebuilt from the modal damping matrix D by means of modal expansion on nodal degrees of freedom:

$$\mathsf{D}_{\mathsf{cb}} = \mathsf{Z}_{\mathsf{cb}}^{\mathsf{T}}\breve{\mathsf{D}}\mathsf{Z}_{\mathsf{cb}} = \mathsf{Z}_{\mathsf{cb}}^{\mathsf{T}}\mathsf{Z}^{-\mathsf{T}}\mathsf{D}\mathsf{Z}^{-1}\mathsf{Z}_{\mathsf{cb}}$$

[5] If we define as $\mathsf{p}^{(RM)} = \left\{0^{\mathsf{T}} \quad \mathsf{p}_{\mathsf{S}}^{(RM)\mathsf{T}}\right\}^{\mathsf{T}}$ the residual vector, the process noise would become:

$$\mathsf{w}_{\mathsf{cb}} = \mathsf{Z}_{\mathsf{cb}}^{\mathsf{T}}\left(\breve{\mathsf{w}} + \breve{\mathsf{M}}\ddot{\mathsf{p}}^{RM} + \breve{\mathsf{D}}\dot{\mathsf{p}}^{RM} + \breve{\mathsf{K}}\mathsf{p}^{RM}\right)$$

However, if the number of added modes is enough to describe the entire frequency range of the excitation, we can assert that:

$$\mathsf{w}_{\mathsf{cb}} \approx \mathsf{Z}_{\mathsf{cb}}^{\mathsf{T}}\breve{\mathsf{w}}$$

where, defining as $\mathsf{z}_{\mathsf{cb}}^{(r)}$ the *r-th* column of Z_{cb}, the $\boldsymbol{\varphi}_{\mathsf{cb}}^{(r)}$ are expressible in such a following way:

$$\boldsymbol{\varphi}_{\mathsf{cb}}^{(r)}(\xi^{\alpha}) = \sum_{k=1}^{N_{dof}} \breve{\boldsymbol{\varphi}}^{(k)}(\xi^{\alpha}) z_{\mathsf{cb}_k}^{(r)} \tag{1.32}$$

In the rest of dissertation the equations concerning the state-observer will be developed by considering a generic modal truncation. However, all the equations below could be used with any reduced order model like dynamic condensation.

1.2 State observers

In this section, the theory of the most important state observer will be discussed. At the beginning, first-order observers are introduced along with Kalman filter and Kalman-based approaches that will be reviewed for structural dynamics problems. These observers are introduced to show why it is necessary to consider more suitable tools for the mechanical problems under consideration.

1.2.1 First order observer

In control theory, it is defined as *state observer* a dynamic system able to estimate the evolution of a state under observation. The evolution of a system with state $\mathsf{x} \in \mathbb{R}^{N_x}$ and output $\mathsf{y} \in \mathbb{R}^{N_y}$ (with N_x and N_y sizes of state and measurement vectors) is given by

$$\begin{aligned} \dot{\mathsf{x}}(t) &= f(\mathsf{x}(t), \mathsf{u}(t)) + \mathsf{w}(t) \\ \mathsf{y} &= g(\mathsf{x}(t), \mathsf{u}(t)) + \mathsf{v}(t) \end{aligned} \tag{1.33}$$

where f and g represent the evolution of state and output as a nonlinear function of the state, $\mathsf{u} \in \mathbb{R}^{N_u}$ is the input vector (with N_u number of inputs), and w and v represent, respectively, the process and measurements noises. If we consider applications in the range of linearized time-invariant systems, the Eq. (1.33) can be arranged as follows:

$$\begin{aligned} \dot{\mathsf{x}}(t) &= \mathsf{A}\mathsf{x}(t) + \mathsf{B}\mathsf{u}(t) + \mathsf{w}(t) \\ \mathsf{y}(t) &= \mathsf{G}\mathsf{x}(t) + \mathsf{J}\mathsf{u}(t) + \mathsf{v}(t) \end{aligned} \tag{1.34}$$

where the following time-invariant matrices are introduced: A state matrix, B output matrix, G state-to-output matrix and J input-to-output matrix. When dealing with state-observation an important issue concerns the observability of the system, namely the possibility to observe the state evolution given the active measurement set $\mathsf{y}(t)$. For linear time-invariant systems like the previous-one, the observability condition is ensured when the observation Gramian

$$\mathsf{W}_o(t_f, t_0) = \int_{t_0}^{t_f} e^{\mathsf{A}^\mathsf{T}(\tau - t_0)} \mathsf{G}^\mathsf{T} e^{\mathsf{A}(\tau - t_0)} \mathrm{d}\tau$$

is full rank. Generally, the observation is performed by introducing an additional term in the Eq. (1.34) that updates the state estimation relying on the knowledge of the measurements. The observer must ensure the convergence of estimation to the state of the plant in Eq. (1.34). Hereafter, we will use the symbol $\hat{\bullet}$ to mark estimations of quantities already introduced. The observation of system in Eq. (1.34) is generally expressed as

$$\begin{aligned} \dot{\hat{\mathsf{x}}}(t) &= \mathsf{A}\hat{\mathsf{x}}(t) + \mathsf{B}\mathsf{u}(t) + \bar{\mathsf{L}}(t)\mathsf{r}(t) \\ \hat{\mathsf{y}}(t) &= \mathsf{G}\hat{\mathsf{x}}(t) + \mathsf{J}\mathsf{u}(t) \end{aligned} \tag{1.35}$$

where, without loss of generality, $\bar{\mathsf{L}}(t)$ is the time-dependent gain matrix that ensures the asymptotically convergence of the error $\mathsf{e} = \mathsf{x} - \hat{\mathsf{x}}$ to zero, and $\mathsf{r} = \mathsf{y} - \hat{\mathsf{y}}$ is the measurement residual between the measured quantities and the ones estimated by means of the observation process itself. When the gain matrix $\bar{\mathsf{L}}$ is constant in time, the state observers are generally referred as Luenberger observers. Then, if the system is observable, the necessary condition to get a convergent observation

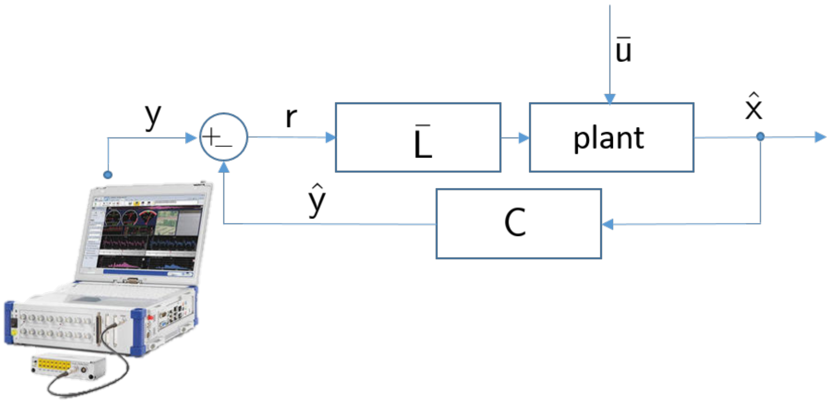

Figure 1.2: Block diagram of state observers.

is that $\mathsf{A} - \bar{\mathsf{L}}\mathsf{G}$ has stable poles. Therefore, the gain matrix $\bar{\mathsf{L}}$ can be computed by means of pole-placing and the poles of $\mathsf{A} - \bar{\mathsf{L}}\mathsf{G}$ can be chosen arbitrarily. The rate of convergence depends on the choice of the poles. Frequently, it leads to choose high-gain observers that have as main drawbacks the sensitivity to noise (see Eq. (1.34)) and the peaking phenomena at beginning of the estimation process.

Kalman Filter

Kalman filter (KF) is a recursive observation process that estimates the state of the system by considering noisy measurements and process [29]. Even though KF is not used in this thesis, its theory is illustrated in order to outline the state of the art. In this framework the continuous-time version of KF, also known as Kalman-Bucy filter, will be considered as the limit of the discrete case [29, 30]. KF assigns to the evolution of the system a multivariate normal distribution that depends on process and measurement noises. The idea behind KF is to compute recursively a gain matrix able to minimize the error covariance $\mathsf{P}(t) = E[(\mathsf{x}(t) - \hat{\mathsf{x}}(t))\,(\mathsf{x}(t) - \hat{\mathsf{x}}(t))(t)^{\mathsf{T}}]$ in order to get always the most likely value of the state, that is the reason why KF is referred as optimal estimator. Therefore, consider a zero-mean Gaussian process and measurement noises such that:

$$E[\mathsf{w}(t)\,\mathsf{w}(\tau)^{\mathsf{T}}] = \mathsf{Q}\delta(t-\tau) \tag{1.36a}$$

$$E[\mathsf{v}(t)\,\mathsf{v}(\tau)^{\mathsf{T}}] = \mathsf{R}\delta(t-\tau) > 0 \tag{1.36b}$$

$$E[\mathsf{w}(t)\,\mathsf{v}(\tau)^{\mathsf{T}}] = \mathsf{U}\delta(t-\tau) \tag{1.36c}$$

$$\begin{bmatrix} \mathsf{Q} & \mathsf{U} \\ \mathsf{U}^{\mathsf{T}} & \mathsf{R} \end{bmatrix} \geq 0 \tag{1.36d}$$

and initial condition given by the expected value of the state $\hat{\mathsf{x}}_0 = E[x_0]$ and its uncertainty $\mathsf{P}_0 = \mathrm{cov}(\mathsf{x}_0)$. From Eq. (1.34), under the hypothesis above, it is possible to consider the propagation of state covariance $\Pi(t) = \mathrm{cov}(\mathsf{x})$ as [6]

$$\begin{aligned} &\dot{\Pi}(t) = \mathsf{A}\Pi(t) + \Pi(t)\mathsf{A} + \mathsf{Q} \qquad (1.37) \\ &\Pi_0 = \mathrm{cov}(\mathsf{x}_0) \quad \text{Initial conditions} \end{aligned}$$

Now, considering a state observer like the one in Eq. (1.35) and the error defined as $\mathsf{e}(t) = \mathsf{x}(t) - \hat{\mathsf{x}}(t)$, it is possible to define the state error dynamics as

$$\dot{\mathsf{e}}(t) = (\mathsf{A} - \bar{\mathsf{L}}(t)\mathsf{G})\hat{\mathsf{x}}(t) + \mathsf{w}(t) - \bar{\mathsf{L}}(t)\mathsf{v}(t) \qquad (1.38)$$

Similarly to Eq. (1.37), by means of Eq. (1.38) it is possible to get the dynamics of $\mathsf{P}(t)$:

$$\begin{aligned} \dot{\mathsf{P}}(t) = (\mathsf{A} - \bar{\mathsf{L}}(t)\mathsf{G})\mathsf{P}(t) + \mathsf{P}(t)(\mathsf{A} - \bar{\mathsf{L}}(t)\mathsf{G})^{\mathsf{T}} + \mathsf{Q} + \qquad (1.39) \\ \bar{\mathsf{L}}(t)\mathsf{R}\bar{\mathsf{L}}^{\mathsf{T}}(t) - \mathsf{U}\bar{\mathsf{L}}^{\mathsf{T}}(t) - \bar{\mathsf{L}}(t)\mathsf{U}^{\mathsf{T}} \end{aligned}$$

with initial condition P_0 assigned. It can be demonstrated that the optimal solution of Eq. (1.39) is obtained when

$$\bar{\mathsf{L}}(t) = (\mathsf{P}(t)\mathsf{G}^{\mathsf{T}} + \mathsf{U})\mathsf{R}^{-1} \qquad (1.40)$$

Substituting the expression in Eq. (1.40) in Eq. (1.39), the quadratic differential equation below is obtained

$$\dot{\mathsf{P}}(t) = \mathsf{A}\mathsf{P}(t) + \mathsf{P}(t)\mathsf{A}^{\mathsf{T}} + \mathsf{Q} - \bar{\mathsf{L}}(t)\mathsf{R}\bar{\mathsf{L}}^{\mathsf{T}}(t) \qquad (1.41)$$

that is also known as Lyapunov Equation. This equation is asymptotically stable and, a stationary value of P_{ss} (and in turn also the steady state gain $\bar{\mathsf{L}}_{ss}$) can be

---

[6] To obtain the propagation of state covariance, consider to proceed with the limit of difference quotient:

$$\begin{aligned} \lim_{\epsilon\to 0} \hat{\mathsf{x}}(k\epsilon) &= \lim_{\epsilon\to 0}(\mathsf{I} + \mathsf{A}\epsilon)\hat{\mathsf{x}}((k-1)\epsilon) + \mathsf{w}((k-1)\epsilon)\epsilon \\ \lim_{\epsilon\to 0} \Pi(k\epsilon) &= \lim_{\epsilon\to 0}(\mathsf{I} + \mathsf{A}\epsilon)\Pi((k-1)\epsilon)(\mathsf{I} + \mathsf{A}\epsilon)^{\mathsf{T}} + \mathsf{Q}((k-1)\epsilon)\epsilon \end{aligned}$$

computed by solving the following quadratic equation [7]:

$$0 = \mathsf{A}\mathsf{P}_{\mathsf{ss}} + \mathsf{P}_{\mathsf{ss}}\mathsf{A}^{\mathsf{T}} + \mathsf{Q} - \bar{\mathsf{L}}_{\mathsf{ss}}\mathsf{R}\bar{\mathsf{L}}_{\mathsf{ss}}^{\mathsf{T}} \tag{1.43a}$$

$$\bar{\mathsf{L}}_{ss} = (\mathsf{P}_{ss}\mathsf{G}^{\mathsf{T}} + \mathsf{U})\mathsf{R}^{-1} \tag{1.43b}$$

If the idea is to monitor along time the response of a linear time-invariant system like the ones being object of this thesis, the use of the unsteady KF could result in a loss of computational power, thus the steady state KF can fit better the purpose. KF, in case the system is observable and the conditions in Eq. (1.36a) are respected, is always computable by means of the closed formula in Eq. (1.43a) that admits only two solutions, of which only one stable solution.

However, KF is not a suitable tool to study second-order mechanical systems [12, 18], namely it does not ensure the kinematic relationship present within these problems. Indeed, consider the following second-order linear dynamic system recast in first order form [8] :

$$\begin{aligned} \begin{Bmatrix} \mathsf{q} \\ \dot{\mathsf{q}} \end{Bmatrix}^{\cdot} &= \begin{bmatrix} 0 & \mathsf{I} \\ -\mathsf{M}^{-1}\mathsf{K} & -\mathsf{M}^{-1}\mathsf{D} \end{bmatrix} \begin{Bmatrix} \mathsf{q} \\ \dot{\mathsf{q}} \end{Bmatrix} + \begin{bmatrix} 0 \\ \mathsf{M}^{-1} \end{bmatrix} \mathsf{u} + \mathsf{w} \\ \mathsf{y} &= \mathsf{G}_d\mathsf{q} + \mathsf{G}_v\dot{\mathsf{q}} + \mathsf{J}\mathsf{u} + \mathsf{v} \end{aligned} \tag{1.44}$$

where q and $\dot{\mathsf{q}}$ represent, respectively, the displacement and velocity vectors, $\mathsf{w} = [0 \ \mathsf{w}_{\mathsf{v}}^{\mathsf{T}}]^{\mathsf{T}}$ the process noise, $\mathsf{M}, \mathsf{D}, \mathsf{K}$, respectively, general mass, damping and stiffness matrices, y the output, v the process noise and $\mathsf{G}_d, \mathsf{G}_v$ and J, respectively, matrices that express the output through $\mathsf{q}, \dot{\mathsf{q}}$ and u. The state estimation equation associated

---

[7] It is worth to remind that combining the two equations in Eq. (1.43a), the well known Riccati equation is obtained:

$$0 = \mathsf{A}\mathsf{P}_{\mathsf{ss}} + \mathsf{P}_{\mathsf{ss}}\mathsf{A}^{\mathsf{T}} + \mathsf{Q} - (\mathsf{P}_{\mathsf{ss}}\mathsf{G}^{\mathsf{T}} + \mathsf{S})\mathsf{R}^{-1}(\mathsf{P}_{\mathsf{ss}}\mathsf{G}^{\mathsf{T}} + \mathsf{S})^{\mathsf{T}} \tag{1.42}$$

[8] By taking into account Eq. (1.23) it is possible to get G_d, G_v, J by taking into account also accelerations

$$\mathsf{G}_d = \mathsf{S}_d - \mathsf{S}_a\mathsf{M}^{-1}\mathsf{K} \qquad \mathsf{G}_v = \mathsf{S}_v - \mathsf{S}_a\mathsf{M}^{-1}\mathsf{D} \qquad \mathsf{J} = \mathsf{S}_a\mathsf{M}^{-1}$$

to the dynamics in Eq. (1.44) is generally expressed as follows:

$$\begin{aligned}\begin{Bmatrix} \hat{\mathsf{q}} \\ \hat{\dot{\mathsf{q}}} \end{Bmatrix}^{\boldsymbol{\cdot}} = \; & \begin{bmatrix} \mathsf{0} & \mathsf{I} \\ -\mathsf{M}^{-1}\mathsf{K} & -\mathsf{M}^{-1}\mathsf{D} \end{bmatrix} \begin{Bmatrix} \hat{\mathsf{q}} \\ \hat{\dot{\mathsf{q}}} \end{Bmatrix} + \begin{bmatrix} \mathsf{0} \\ \mathsf{M}^{-1} \end{bmatrix} \mathsf{u} + \\ & \begin{bmatrix} \check{\mathsf{L}} \\ \mathsf{M}^{-1}\mathsf{L} \end{bmatrix} (\mathsf{y} - \mathsf{G}_d\hat{\mathsf{q}} - \mathsf{G}_v\hat{\dot{\mathsf{q}}} - \mathsf{J}\mathsf{u}) \end{aligned} \tag{1.45}$$

KF provides a gain matrix such that $\dot{\hat{\mathsf{q}}} \neq \hat{\dot{\mathsf{q}}}$, except if $\check{\mathsf{L}} = \mathsf{0}$ (never possible [18]) or the residual $\mathsf{y} - \mathsf{G}_d\hat{\mathsf{q}} - \mathsf{G}_v\hat{\dot{\mathsf{q}}} - \mathsf{J}\mathsf{u} \to \mathsf{0}$. The last case is only possible when there are no unknown inputs and the modeling uncertainties are negligible.

Other optimal estimators

Moreover, KF has another fundamental problem, that is it requires the knowledge of the external input. Consider the case where $\mathsf{u} = \bar{\mathsf{u}} + \mathsf{f}$ where $\bar{\mathsf{u}}$ and f represent, respectively, the known and unknown inputs. Here, two different assumptions could be made: *i)* consider the unknown input as Gaussian and consequently as part of the process noise (that is a hypothesis too restrictive on the behavior of the inputs) or *ii)* modify KF in order to estimate also the unknown inputs. The first considerable approach, referred as Augmented Kalman Filter (AKF), was to include the unknown input in the state vector along with an associated user-defined stable random walk dynamics [8, 9]

$$\dot{\mathsf{f}} = -\alpha\mathsf{f} + \mathsf{w}_\mathsf{f} \qquad \alpha \geq 0 \tag{1.46}$$

eventually having the following state vector

$$\mathsf{x}^\mathsf{T} = \begin{Bmatrix} \mathsf{q}^\mathsf{T} & \dot{\mathsf{q}}^\mathsf{T} & \mathsf{f}^\mathsf{T} \end{Bmatrix}$$

and system

$$\begin{aligned} \begin{Bmatrix} \mathsf{q} \\ \dot{\mathsf{q}} \\ \mathsf{f} \end{Bmatrix}^{\boldsymbol{\cdot}} &= \begin{bmatrix} \mathsf{0} & \mathsf{I} & \mathsf{0} \\ -\mathsf{M}^{-1}\mathsf{K} & -\mathsf{M}^{-1}\mathsf{D} & \mathsf{I} \\ \mathsf{0} & \mathsf{0} & -\alpha\mathsf{I} \end{bmatrix} \begin{Bmatrix} \mathsf{q} \\ \dot{\mathsf{q}} \\ \mathsf{f} \end{Bmatrix} + \begin{bmatrix} \mathsf{0} \\ \mathsf{M}^{-1} \\ \mathsf{0} \end{bmatrix} \bar{\mathsf{u}} + \begin{bmatrix} \mathsf{0} & \mathsf{0} \\ \mathsf{I} & \mathsf{0} \\ \mathsf{0} & \mathsf{I} \end{bmatrix} \begin{Bmatrix} \mathsf{w}_v \\ \mathsf{w}_\mathsf{f} \end{Bmatrix} \\ \mathsf{y} &= \begin{bmatrix} \mathsf{G}_d & \mathsf{G}_v & \mathsf{J} \end{bmatrix} \begin{Bmatrix} \mathsf{q} \\ \dot{\mathsf{q}} \\ \mathsf{f} \end{Bmatrix} + \mathsf{J}\bar{\mathsf{u}} + \mathsf{v} \end{aligned} \tag{1.47}$$

The augmented system is then observed by means of the same procedure shown above in KF theory. It works by assigning an *a priori* covariance matrix to the derivative of external forces. Another important tool used for this purpose is the one presented in [10, 11, 28], that is originally known as *Unbiased minimum-variance input and state estimation* and recently referred as *Joint Input-State estimator*. This algorithm is inspired by the discrete-time KF and consists of three different steps: *i)* time update of the state (expressed in a similar way w.r.t. KF considering an unknown input to be estimate), *ii)* input update where a minimum variance and unbiased gain matrix is synthesized to update the input at each step and *iii)* the measurement update (also similar to the one in discrete KF). It is worth to notice that also this procedure, like KF, converges for $t \to \infty$ providing a steady state observer. The stated advantage of this method concern the estimation of external forces without any prior knowledge of inputs. However, it works only with acceleration measurements and, consequently, it is highly dependent on sensor placement. It is worth noticing that both the mentioned methods are still not natural for mechanical systems.

1.2.2 Second order observer

Considerations that the first order observer is not natural for mechanical systems have been made since the last years of nineties [12]. If we consider a mechanical system like the one in Eq. (1.23) (without considering the known external inputs), a second order natural observer can be written as follows:

$$\begin{aligned} \mathsf{M}\ddot{\hat{\mathsf{q}}} + \mathsf{D}\dot{\hat{\mathsf{q}}} + \mathsf{K}\hat{\mathsf{q}} &= \mathsf{L}\mathsf{r} \\ \mathsf{y} &= \mathsf{S}_d\hat{\mathsf{q}} + \mathsf{S}_v\dot{\hat{\mathsf{q}}} + \mathsf{S}_a\ddot{\hat{\mathsf{q}}} \end{aligned} \tag{1.48}$$

In the natural observer defined above the relationship $\dot{\hat{\mathsf{q}}} = \hat{\dot{\mathsf{q}}}$ is always ensured. Unfortunately there exists no closed formula to find an optimal state observer and the gain matrix must always be synthesized by means of a numerical optimization procedure. The definition of state error is critical for this end. In KF and other first order observers the error is defined by the difference between the predicted state and the true unknown state. From the definition of state error, there follows the Riccati equation and, consequently, a closed relationship that allows to define the optimal gain matrix. It is worth to notice that, in a general second order observer the state is not necessarily made up by velocities and displacements. The definition of state relies on the user choice. In case we define the state error ε taking into account only

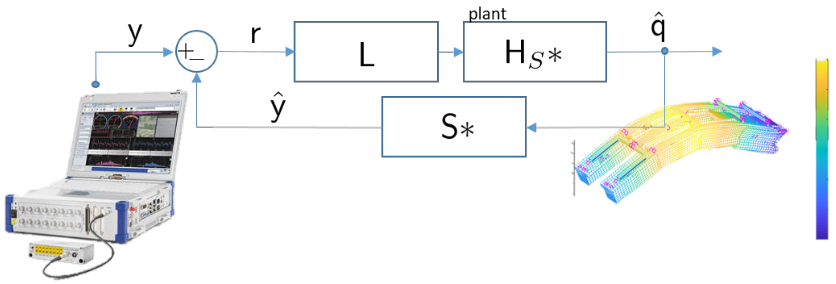

Figure 1.3: Block diagram of second order observers.

the displacements such as follows:

$$\varepsilon = \mathsf{q} - \hat{\mathsf{q}} \tag{1.49}$$

it is possible to obtain the error dynamics from Eqs. (1.44, 1.48):

$$\mathsf{M}\ddot{\varepsilon} + \mathsf{D}\dot{\varepsilon} + \mathsf{K}\varepsilon + \mathsf{LS}_a\ddot{\varepsilon} + \mathsf{LS}_v\dot{\varepsilon} + \mathsf{LS}_d\varepsilon = \mathsf{f} + \mathsf{w} + \mathsf{Lv} \tag{1.50}$$

The Fourier transform of Eq. 1.50 yields

$$\left[-\omega^2(\mathsf{M} + \mathsf{LS}_a) + i\omega(\mathsf{D} + \mathsf{LS}_v) + (\mathsf{K} + \mathsf{LS}_d)\right]\tilde{\varepsilon}(\omega) = \tilde{\mathsf{f}}(\omega) + \tilde{\mathsf{w}}(\omega) + \mathsf{L}\tilde{\mathsf{v}}(\omega) \tag{1.51}$$

By defining

$$\tilde{\mathsf{H}}_O(\omega) = [-\omega^2(\mathsf{M} + \mathsf{LS}_a) + i\omega(\mathsf{D} + \mathsf{LS}_v) + (\mathsf{K} + \mathsf{LS}_d)]^{-1} \tag{1.52}$$

Eq. 1.51 provides the frequency response of the state error as

$$\tilde{\varepsilon} = \tilde{\mathsf{H}}_O(\tilde{\mathsf{f}} + \tilde{\mathsf{w}} + \mathsf{L}\tilde{\mathsf{v}}) \tag{1.53}$$

If the statistical features of the forcing terms and process and measurement noises are stochastic, known and uncorrelated each other, the system response to stochastic inputs is easily obtained by means of Eq. (1.53):

$$\Phi_{\varepsilon\varepsilon}(\omega) = \tilde{\mathsf{H}}^*_O(\omega)(\Phi_{\mathsf{ff}}(\omega) + \Phi_{\mathsf{ww}}(\omega) - \mathsf{L}\Phi_{\mathsf{vv}}(\omega)\mathsf{L}^\mathsf{T})\tilde{\mathsf{H}}^\mathsf{T}_O(\omega) \tag{1.54}$$

where $\Phi_{\bullet\bullet}$ indicates the power spectral densities. Finaly, Eq. (1.54) yields the covariance of the state error

$$\Sigma^2_{\varepsilon\varepsilon} = \int_{-\infty}^{+\infty} \Phi_{\varepsilon\varepsilon}(\omega)\mathrm{d}\omega \tag{1.55}$$

Note that the quantity above depends on the gain matrix L. Given the power spectral densities of external forces and the process and measurement noises, the goal is to find the optimal free parameters that minimize the trace of $\Sigma^2_{\varepsilon\varepsilon}$ making this observer optimal. However, the synthesized observer should be such that the stability of the observation system is ensured. Indeed, all the poles of $\tilde{\mathsf{H}}_O$ must have negative real part.

This approach is similar to the one of KF. The main differences consist in the different definition of $\bar{\mathsf{L}}$ and state error. In the present case $\breve{\mathsf{L}}$ portion is constrained to be zero ensuring a natural observation of the system. Although the error definition is different, note that it is possible to consider the same definition of the P trace used in the Kalman filter. Indeed if we consider the error e such that

$$\mathsf{e} = \begin{Bmatrix} \varepsilon \\ \dot{\varepsilon} \end{Bmatrix}$$

the following relationship is valid:

$$tr(\mathsf{P}) = tr\Big(\int_{-\infty}^{+\infty} \Phi_{\mathsf{ee}}(\omega)\mathrm{d}\omega\Big) \equiv tr\Big(\int_{-\infty}^{+\infty} (1+\omega^2)\Phi_{\varepsilon\varepsilon}(\omega)\mathrm{d}\omega\Big)$$

It is worth noting that it is not the integration to be equivalent. We obtain the equivalence only when the trace is performed. The choice of the function to be minimized at this point is completely user-dependent. If the state consists of modal coordinates in which the mass matrix and the stiffness are diagonal, an energetic meaning could be assigned to the covariance function. In fact, by defining an error such that:

$$\bar{\mathsf{e}} = \begin{Bmatrix} \mathsf{K}^{1/2}\varepsilon \\ \mathsf{M}^{1/2}\dot{\varepsilon} \end{Bmatrix} = \begin{Bmatrix} \sqrt{k_1}\varepsilon_1 \\ \vdots \\ \sqrt{k_{N_q}}\varepsilon_{N_q} \\ \sqrt{m_1}\dot{\varepsilon}_1 \\ \vdots \\ \sqrt{m_{N_q}}\dot{\varepsilon}_{N_q} \end{Bmatrix}$$

the function to be minimized would become

$$tr(\bar{\mathsf{P}}) \equiv tr\Big(\int_{-\infty}^{+\infty}\Big[\mathsf{K}\Phi_{\varepsilon\varepsilon}+\omega^2\mathsf{M}\Phi_{\varepsilon\varepsilon}\Big]\mathrm{d}\omega\Big)$$

With this approach we go completely out of the rigid Kalman filter patterns. The objective function becomes customizable according to the user's engineering sensitivity. The main drawback of this approach relies on the fact that this gain matrix can be computed only by means of an optimization procedure that involves a large design variables space. In Sec. 2.2 we will investigate how to get this gain matrix despite the so many variables involved.

Chapter 2

Methodological approach for virtual sensing

The aim of the thesis is to develop a numerical procedure for the estimation of load and elastic deflection field from a discrete set of experimental data. To do this, interpolation methods can be used, but if the topology of the structure is complex, some issues arise in the construction of the basis functions with respect to the nodes. However, in general, a large number of sensors is welcome to minimize these problems. Furthermore, another common requirement is that these sensors should be homogeneous in type.

In this thesis, to overcome these issues, the proposed approach relies on state observers. There are several reasons to follow an approach based on state observers. First, these involve additional information about the underlying physics, that is, the theoretical model of the observed system. Interpolation methods exploit only indirectly and rather weakly some knowledge about the system. Second, the state concept is a more general concept with respect to the raw information available at sensor nodes. The state, obtained by modal truncation (or other transformations in Lagrangian terms, such as the Craig-Bampton reduction method) is able to describe the structural dynamics behavior of a complex structure rather efficiently by means of a minimum number of parameters. Consequently, the state observers are able to estimate the system dynamics by means of measurements also in presence of noise provided that its statistical features are provided by user.

In particular, a second order natural observer will be used for this purpose. This observer, as explained in the Chap. 1, has great advantages compared to the generally used approaches but demands for an optimization process that unfortunately involves a great number of free parameters. To overcome this issue, in Sec. 2.2 it is presented a technique to reduce the number of free parameters along with details about the optimization process and further arising considerations. The main novelties of the present thesis are introduced in the extensions proposed in Sec. 2.3.

The chapter is ended by a section that introduces the quality indicators generally used in state observation.

2.1 Description of the methodology

In this section, the main steps of the approach are reviewed. Fig. 2.1 illustrates synthetically the methodology work-flow. To get a full picture of the behavior of the structure we need an updated numerical model along with a-priori statistical informations of the system. These informations combined with measurement data and a good estimation algorithm are able to provide the real-time digital twin of the structure which informs the crew (or an expert system) about dynamic behavior and loads.

In Sec. 2.1.1 the model updating phase will be reviewed. whereas the way the *a priori* statistical informations are obtained will be explained in Sec. 2.1.2, on the other hand, points out how to get the *a priori* statistical informations needful for the synthesis of the observer. Secs. 2.1.3 and 2.1.4 will provide a more comprehensive classification of the sensor data.

2.1.1 Model updating phase

First of all, an updated numerical model is fundamental. This step is particularly challenging since obtaining a finite element model with an elastic behavior similar to the one of the real structure is not straightforward. There are several strategies to perform model updating. The easier way pursues for convergence of modes and natural frequency, whereas a more complicated approach aim to the convergence of experimental frequency response functions. However, with the increasing complexity of the structure topology full convergence is not ensured.

A robust structural updating requires an optimization process that can involve a large number of free parameters that must be carefully identified. Anisotropic materials, bonding, welds and sensor layouts can make the structural updating process very complicated. Furthermore, it is recommended that the final model still has a physical meaning, *i.e.* that the model updating design variables have final values that are within the uncertainty range. The procedure that is used in this

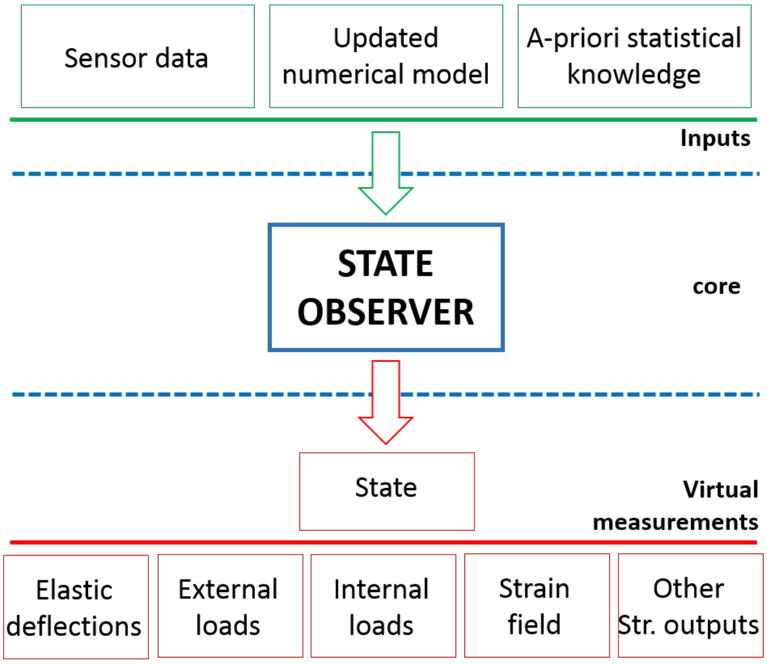

Figure 2.1: Methodology flowchart.

thesis activity to perform model updating exploits the MSC Nastran gradient-based optimization solver [32], by defining the following user dependent objective function [1] :

$$f = \sqrt{\sum_{n=1}^{N_f} \left(c_{f_n} \Delta\omega_n^2 + c_{MAC_n} MAC_n^2 \right)}$$

where $\Delta\omega_n$ and MAC_n are, respectively, the difference between the measured n-*th* modal angular frequency and the numerical-one and the n-*th* diagonal element of MAC matrix, whereas c_{f_n} and c_{MAC_n} are their user assigned weights.

---

[1] MAC is defined as follows:

$$MAC_n = \frac{|\phi_{E_n}\phi_{N_n}|^2}{|\phi_{E_n}\phi_{E_n}||\phi_{N_n}\phi_{N_n}|}$$

where ϕ_{E_n} is the n-*th* experimental modal vector and ϕ_{N_n} is the n-*th* numerical-one.

2.1.2 A priori statistical informations

In addition to the FE model, the approach presented in Sec. 1.2 needs for the statistical properties of the measurements, process noise and the external loads. A correct description of this statistical quantities is essential for the synthesis of a consistent state observer. Providing non-coherent statistical properties results in the design of an observer that aims to observe a different physical process, thus yielding a sub-optimal estimate.

In this regard, there are several ways to get the statistical information about the external loads in the form of their PSD Φ_{ff}. Among these we recognize the possibility to use *i)* numerical simulations, or, *ii)* experimental trials. Indeed, before their operational life, aerospace and marine vehicles go through a whole design phase that involves the numerical and experimental simulations of their dynamic behavior under different external loads. These simulations can be used to obtain the statistical properties of the structure in different cells (*i.e.* operating conditions of the structure). Otherwise, if the structure is available to undergo to a learning phase stage with a sufficient number of sensors, numerical regression methods can be used to get the statistics of external forces.

The statistical properties associated with the measurement noise Φ_{vv} are generally given by specifications provided by the sensor manufacturers. The sensor noise is generally weakly correlated to external forces. Thus, for sake of simplicity, this allows for assuming that the external forces and measurement noise are uncorrelated for the present applications.

On the other hand, the statistical description of process noise Φ_{ww} is not easy to define. Generally, this depends on:

- incorrect modeling of the PSD of external forces.
- numerical modeling uncertainties (mass, stiffness and damping matrices);

Concerning the external forces, it is necessary to provide accurately their PSD by adjusting the gain at every variation of the operating conditions. Regarding the process noise relative to the structural modeling uncertainties, the experimental tests can be used to estimate the difference between the numerical and real transfer functions. For the sake of clarity, the latter contribution to the process noise is also dependent on the intensity of the external forces, which adds a further complication that is not addressed in this thesis activity. The common practice in virtual sensing applications is to introduce a modal diagonal process noise PSD matrix, which

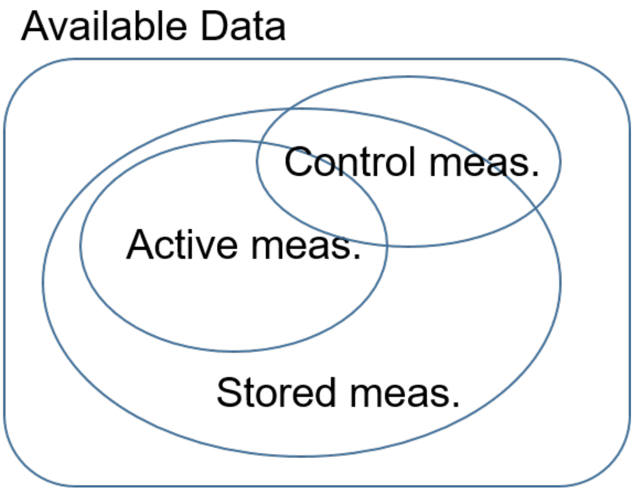

Figure 2.2: Classification of sensor datasets.

means assuming process noise that is uncorrelated to the external forces and to the measurement noise. In this thesis this process noise has been set constant up to the sampling frequency, proportional to the intensity of the external forces.

2.1.3 Classification of sensor datasets

Not all measurements are generally used to update and estimate the state. In this regard, in this section a more comprehensive classification of the available data is provided. Indeed, the available measurements are split up into three different groups:

- **Active measurements** y. This is the input processed by the presented method to build the approximation model. These data are provided by sensors constituting the permanent sensor array upon which the expert monitoring system will be permanently based and coincide with the data used in Chap. 1.

- **Stored measurements** y_s. The use of this type of data will be introduced in Sec. 2.3.1 when it will be proposed to use the data already stored to improve the synthesis of the state observer. It includes the data upon which the procedure internally tries to minimize its errors, or conversely to refine its capability to predict the correct values.

- **Control measurements** y_c. These are available measurements used to check the final performances but which do not drive the optimization procedure.

The introduction of the Stored meas. set corresponds to perform the so-called “learning phase” when the system is installed on-board the vehicle or in the monitored structure; the Stored Measurements are obtained by means of an array of sensors some of which, after the “learning phase”, are removed (see $\mathsf{y_r}$ in Sec. 2.3.1). These concepts are further explained in the diagram in Fig. 2.2. The Stored and the Control Measurements are distinct sets because we are specifically interested in evaluating the performances also in points which does not take part to the optimization process. The introduced available measurement sets can be expressed as a function of the state:

$$\mathsf{y} = \mathsf{S}_a\ddot{\mathsf{q}} + \mathsf{S}_v\dot{\mathsf{q}} + \mathsf{S}_d\mathsf{q} + \mathsf{v} \tag{2.1a}$$

$$\mathsf{y_s} = \mathsf{S}^{\mathsf{s}}_a\ddot{\mathsf{q}} + \mathsf{S}^{\mathsf{s}}_v\dot{\mathsf{q}} + \mathsf{S}^{\mathsf{s}}_d\mathsf{q} + \mathsf{v_s} \tag{2.1b}$$

$$\mathsf{y_c} = \mathsf{S}^{\mathsf{c}}_a\ddot{\mathsf{q}} + \mathsf{S}^{\mathsf{c}}_v\dot{\mathsf{q}} + \mathsf{S}^{\mathsf{c}}_d\mathsf{q} + \mathsf{v_c} \tag{2.1c}$$

where the selection matrices $\mathsf{S}_a, \mathsf{S}_v$ and S_d are specialized for the considered type of output by means of apexes $\bullet^{\mathsf{s}}$ and $\bullet^{\mathsf{c}}$.

2.1.4 Virtual measurements

Virtual measurements consist of the new information (not directly recorded) that is desirable to get. It is up to the state observer provide these data. This information is obtained *a posteriori* once the state is evaluated, and, similarly to Eq. (2.1a) can be expressed as follows:

$$\hat{\mathsf{y}}_{\mathsf{v}} = \mathsf{S}^{\mathsf{v}}_a\ddot{\hat{\mathsf{q}}} + \mathsf{S}^{\mathsf{v}}_v\dot{\hat{\mathsf{q}}} + \mathsf{S}^{\mathsf{v}}_d\hat{\mathsf{q}} \tag{2.2}$$

Example of virtual measurements are:

- the elastic deflections
- the external loads
- the internal loads (stress field)
- the strain field
- other structural output that can be obtained through finite elements

These quantities can subsequently be used for other purposes (see Appendix C).

2.2 Application issues on observer synthesis

In this section we will discuss the practical issues concerning the second order observers. Among these we recognize: *i)* the reduction of the design variables by means of an opportune decomposition strategy, and *ii)* the optimization procedure that involves the reduced design variables space. Then, some practical considerations are introduced concerning the meaning of the proposed observer.

2.2.1 Gain decomposition

The estimate of optimal gain matrix represents a complex optimization problem, where the set of design variables is made up by all the elements of L. In this section, a generalized approach based on the one presented in [15] and [18] is introduced. Usually, the measurements of accelerations, velocities and displacements are uncorrelated each other so having that the output y can be partitioned as

$$\mathsf{y} = \begin{Bmatrix} \mathsf{y}^{[a]} \\ \mathsf{y}^{[v]} \\ \mathsf{y}^{[d]} \end{Bmatrix} \tag{2.3}$$

where $\mathsf{y}^{[a]}$, $\mathsf{y}^{[v]}$ and $\mathsf{y}^{[d]}$ are the partition of measurements vector into accelerations (*e.g.*, accelerometers), velocities (*e.g.*, potentiometers) and displacements (*e.g.*, strain gages), respectively, with size $N^{[a]}$, $N^{[v]}$ and $N^{[d]}$. In a similar way we can express the selection matrices as it follows:

$$\mathsf{S}_a = \begin{bmatrix} \mathsf{S}^{[a]} \\ 0 \\ 0 \end{bmatrix} \qquad \mathsf{S}_v = \begin{bmatrix} 0 \\ \mathsf{S}^{[v]} \\ 0 \end{bmatrix} \qquad \mathsf{S}_d = \begin{bmatrix} 0 \\ 0 \\ \mathsf{S}^{[d]} \end{bmatrix} \tag{2.4}$$

where the partitions of selection matrices $\mathsf{S}^{[a]}$, $\mathsf{S}^{[v]}$ and $\mathsf{S}^{[d]}$ have, respectively, size $N^{[a]} \times N_q$, $N^{[v]} \times N_q$ and $N^{[d]} \times N_q$. Consequently, the gain matrix is defined as

$$\mathsf{L} = \begin{bmatrix} \mathsf{L}^{[a]} & \mathsf{L}^{[v]} & \mathsf{L}^{[d]} \end{bmatrix} \tag{2.5}$$

By taking into account the decompositions in [15] and [18], the gain matrices $\mathsf{L}^{[a]}$,$\mathsf{L}^{[v]}$ and $\mathsf{L}^{[d]}$ can be synthesized as it follows:

$$\mathsf{L}^{[a]} = \mathsf{S}^{[a]^{\mathsf{T}}}\Xi_a \tag{2.6a}$$

$$\mathsf{L}^{[v]} = \mathsf{S}^{[v]^{\mathsf{T}}}\Xi_v \tag{2.6b}$$

$$\mathsf{L}^{[d]} = \mathsf{S}^{[d]^{\mathsf{T}}}\Xi_d \tag{2.6c}$$

where Ξ_a $(N^{[a]} \times N^{[a]})$, Ξ_v $(N^{[v]} \times N^{[v]})$ and Ξ_d $(N^{[d]} \times N^{[d]})$ are assumed to be diagonal matrices. Their diagonal elements (whose number is the same of active measurements) could be in a sufficient number to get a good compromise for an optimal observer. In addition, the particular shape assumed by the gain matrix ensures the symmetry of the problem since

$$\tilde{\mathsf{H}}_O(\omega) = [-\omega^2(\mathsf{M} + \mathsf{S}^{[a]^{\mathsf{T}}}\Xi_a\mathsf{S}^{[a]}) + i\omega(\mathsf{D} + \mathsf{S}^{[v]^{\mathsf{T}}}\Xi_v\mathsf{S}^{[v]}) + (\mathsf{K} + \mathsf{S}^{[d]^{\mathsf{T}}}\Xi_d\mathsf{S}^{[d]}]^{-1} \tag{2.7}$$

This observer is such that a weight for each sensor is assigned by means of the diagonal elements of Ξ_a $(N^{[a]} \times N^{[a]})$, Ξ_v $(N^{[v]} \times N^{[v]})$ and Ξ_d $(N^{[d]} \times N^{[d]})$. However, this approach may be too restrictive to achieve a good optimum since it relies only on a weight assigned to each sensor [18]. Albeit it is still possible to perform the optimization of the full gain matrix L (although it is unlikely to find a global optimum owing to high number of free parameters involved), in this work another observer decomposition is proposed:

$$\mathsf{L}^{[a]} = \Lambda_a\mathsf{S}^{[a]^{\mathsf{T}}}\Xi_a \tag{2.8a}$$

$$\mathsf{L}^{[v]} = \Lambda_v\mathsf{S}^{[v]^{\mathsf{T}}}\Xi_v \tag{2.8b}$$

$$\mathsf{L}^{[d]} = \Lambda_d\mathsf{S}^{[d]^{\mathsf{T}}}\Xi_d \tag{2.8c}$$

where Λ_a, Λ_v and Λ_d (each having size $N_q \times N_q$) are matrices that weigh the generalized coordinates according to how these modes are supposed to be influenced by external forces and their own dynamics. In this way, we pursue to get the best observer possible by considering a reduced number of variables.

2.2.2 Optimization technique

Generally speaking, an optimal estimator is obtained by minimizing the state error through an optimization problem subject to stability constraints. The problem can

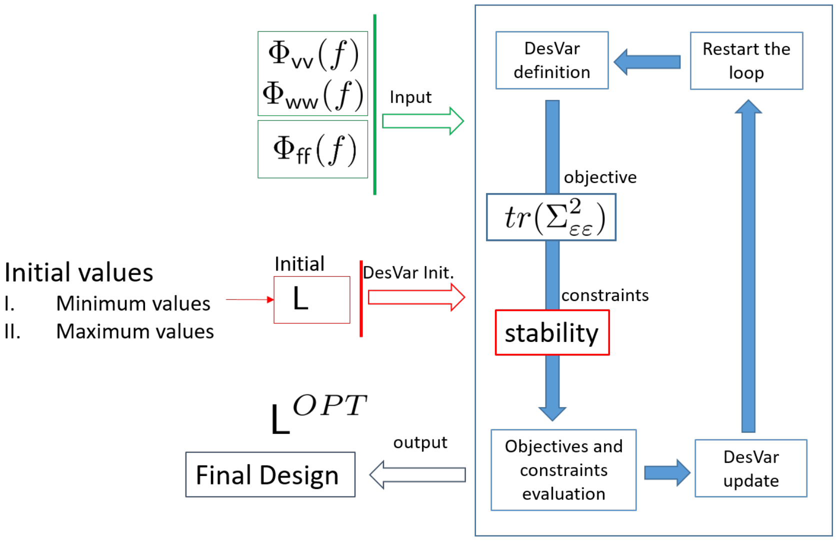

Figure 2.3: Optimization process loop.

be stated as follows:

- **design variables**. $\lambda \in \mathbb{R}^{N_o}$ (with N_o number of variables) lists the diagonal elements of $\Xi_a, \Xi_v, \Xi_d, \Lambda_a \Lambda_v$ and Λ_d;
- **objective**. The trace of $\Sigma^2_{\varepsilon\varepsilon}$ is assumed as objective function although it has been pointed out that P or $\bar{\mathsf{P}}$ can be used as well

$$\min_{\lambda \in \mathbb{R}^{N_o}} tr(\Sigma^2_{\varepsilon\varepsilon})(\lambda)$$

- **constraints**. The observer system must be stable, such that:

$$Re\Big[poles(\tilde{\mathsf{H}}_O^{-1})\Big] < 0$$

The optimization process is implemented within *Matlab*® Framework [31] and illustrated in Fig. 2.3. The optimization framework requires for the specific inputs of this problem, such as the mass, damping and stiffness matrices along with the PSDs of noises and external forces.

To enhance the process, several factors must be considered. First of all, the number of variables involved. When dealing with a consistent number of design variables (such as in the case the observer were designed by considering all the elements of L), it is unlikely to reach a global optimum with any type of optimization algorithm. *Deterministic* algorithms (*e.g.* gradient or pattern search methods) would stagnate too early on local minima. Furthermore, there are stability constraints to be respected that greatly limit the applicability of some gradient methods. The issue of *heuristic* algorithms concerns the vastness of space to be explored.

Although the evaluation of the objective function is fast (it is possible to carry out tens or hundreds of evaluations per second, in accordance with the number of spectral lines that are used to compute $\Sigma_{\varepsilon\varepsilon}$), this issue, along with the stability constraint, also makes these last algorithms inefficient in presence of too many free parameters. However, the gain matrix decomposition proposed above allows to manage the optimization in a easier way with both deterministic and heuristic algorithms. With this decomposition, considering tens of modal coordinates and measurements, the number of free parameters, generally, does not exceed 50. The best practice found out in this thesis is to use a genetic algorithm followed by a pattern search.

2.2.3 Data transformation

The second order observer, as it is possible to notice from Eq. (1.48) results in the estimation of the generalized coordinates by means of structural dynamics measurements. The values of the gain matrices influence the estimation dynamics. Stating that the poles of the state observer must be stable means that the estimation must not diverge. In addition, it is recommended that the natural frequencies associated to the observer are out of the excitation frequency range. Otherwise, if that poles are not sufficiently damped, the estimate becomes incorrect due to numerical resonance (that does not depend on the physical response of the system).

However, the estimation process introduced above is perfectly able to avoid this issue since resonance phenomena are recognized as an increase of spectral density of state error. As a consequence, this phenomenon is taken into account in the trade off performed by the optimizer.

Let's consider the case that the measurement data consist of strain gages and accelerations, as in the general sensor layouts. Eq. (1.52) shows how these measurements result in new mass and stiffness of the observation system.

$$\begin{aligned} \text{Observer mass matrix:} &\quad \mathsf{M} + \Lambda_a \mathsf{S}^{[a]^\mathsf{T}} \Xi_a \mathsf{S}^{[a]} \\ \text{Observer stiffness matrix:} &\quad \mathsf{K} + \Lambda_d \mathsf{S}^{[d]^\mathsf{T}} \Xi_d \mathsf{S}^{[d]} \end{aligned}$$

By imposing the natural constraint of positive definite mass and stiffness matrices it can be noticed that: *i)* positive values of Ξ_d results in an increase of observer frequencies whereas *ii)* positive values of Ξ_a produces a decrease of the observer frequencies. Generally speaking, accelerations make the observer slower to follow the physical dynamics. This last consideration highlights a great issue: the optimizer can not give importance to acceleration measurements since it may lead to numerical resonances. The easiest way to proceed is to integrate accelerations in displacements numerically, even if this causes an initial condition problem along with a possible signal drift.

In such applications where we deal with accelerations and strains, the output vector is recast as follows:

$$\mathsf{y} = \begin{Bmatrix} \bar{\mathsf{y}}^{[a]} \\ \mathsf{y}^{[d]} \end{Bmatrix} \tag{2.9}$$

where

$$\bar{\mathsf{y}}^{[a]}(t) = \int_0^t \int_0^s \mathsf{y}^{[a]}(\tau)\mathrm{d}\tau\mathrm{d}s \tag{2.10}$$

thus implying a modification of the observer mass and stiffness matrices:

$$\begin{array}{rc} \text{Observer mass matrix:} & \mathsf{M} \\ \text{Observer stiffness matrix:} & \mathsf{K} + \Lambda_d \mathsf{S}^{[d]^\mathsf{T}} \Xi_d \mathsf{S}^{[d]} + \Lambda_a \mathsf{S}^{[a]^\mathsf{T}} \Xi_a \mathsf{S}^{[a]} \end{array}$$

2.2.4 Considerations on second-order observers

In aeronautical and ship engineering applications the external forces are generally unknown, except for the ones produced by actuators and engines that can be introduced in a straightforward way in the observer equations.

Let us consider the case in which we have only displacements (or we integrate the accelerations as presented in section above). In such a scenario, the idea of an observer that filters experimental measurements through the expected dynamics of the system (see Kalman filter) falls due to the lack of knowledge of the external forces. Hence, the following considerations arise:

- the resulting observer tends to be practically ON/OFF type, where with ON it is meant the observer is high-gain and with OFF that is practically null. The dynamics with a level of excitation (or process noise) dominant compared to the measurements noise will be featured by a high gain observer (ON), whereas the others will have a low gain (OFF). In practice, the observer discerns between the visible or not visible dynamics;

- the observer assigns more weight to the sensors able to describe the most likely dynamics (depending on its position, each sensor will be able to observe some dynamics better than others).

It is recommended that the low damping poles of the observer (*i.e.* the poles of $\tilde{\mathsf{H}}_O$) come out of the excitation spectrum of the external forces. This happens if the number and positioning of the sensors are appropriate. If this happens the state estimation $\hat{\mathsf{q}}$ is instantaneous with respect to the measurements y.

2.3 Second-order observer extensions

All the observer introduced in 1.2 are obtained by searching for the free parameters of gain matrix that minimize the state error. This feature makes those observers optimal. The second order observer introduced in 1.2.2 expands the capabilities of KF since it allows to introduce frequency dependent noise and force statistics. In this section, we pursue to improve the features of second-order observers by proposing at first in Sec. 2.3.1 the use of data stored in a stage previous to the observer synthesis and installation (making the observer adaptive to stored data). Subsequently, passing by an intermediate passage in which a frequency-adaptive observer is defined (see Sec. 2.3.2), we get to the synthesis of the multi-scale observer in Sec. 2.3.3. A further extension is introduced in Appendix B where an optimal estimation of external forces is proposed.

2.3.1 Learning-phase-driven observer

Let us consider the second order observer in Sec. 1. If a set of stored data y_s were recorded in a system learning stage, one could use these measurements to enhance the synthesis of the observer for the state estimation problem. The state estimation can be rewritten as it follows:

$$\tilde{\hat{\mathsf{q}}} = \tilde{\mathsf{H}}_O(\omega)\mathsf{L}\tilde{\mathsf{y}} = \tilde{\mathsf{H}}_O(\omega)\begin{bmatrix}\mathsf{L} & 0\end{bmatrix}\begin{Bmatrix}\tilde{\mathsf{y}}\\ \tilde{\mathsf{y}}_\mathsf{r}\end{Bmatrix} = \tilde{\mathsf{H}}_O(\omega)\mathsf{L}^\mathsf{s}\tilde{\mathsf{y}}_\mathsf{s} \tag{2.11}$$

where $\tilde{\mathsf{y}}_\mathsf{r}$ is the vector of the stored measurements of removed sensors, that are no longer active for state observation. It follows that it is possible to define also the post-fit measurement residual by means of Eq. 2.1b:

$$\tilde{\mathsf{r}}_\mathsf{s} = \tilde{\mathsf{y}}_\mathsf{s} - \tilde{\hat{\mathsf{y}}}_\mathsf{s} = [\mathsf{I} - \tilde{\mathsf{S}}^\mathsf{s}(\omega)\tilde{\mathsf{H}}_O(\omega)\mathsf{L}^\mathsf{s}]\tilde{\mathsf{y}}_\mathsf{s} \tag{2.12}$$

This relationship is however influenced by the noise present in y_s and from non-optimal estimation of state. In a way similar to Eq. 1.54, the power spectral density of the post-fit measurement residual can be processed using the data gathered in the learning phase [2]:

$$\Phi_{\mathsf{r}_\mathsf{s}\mathsf{r}_\mathsf{s}}(\omega) = \left[\mathsf{I} - \tilde{\mathsf{S}}^\mathsf{s}(\omega)\tilde{\mathsf{H}}_O(\omega)\mathsf{L}^\mathsf{s}\right]^* \Phi_{\mathsf{y}_\mathsf{s}\mathsf{y}_\mathsf{s}}(\omega) \left[\mathsf{I} - \tilde{\mathsf{S}}^\mathsf{s}(\omega)\tilde{\mathsf{H}}_O(\omega)\mathsf{L}^\mathsf{s}\right]^\mathsf{T} \tag{2.14}$$

Finaly, Eq. (2.14) yields the covariances of the post-fit residual

$$\Sigma^2_{\mathsf{r}_\mathsf{s}\mathsf{r}_\mathsf{s}} = \int_{-\infty}^{+\infty} \Phi_{\mathsf{r}_\mathsf{s}\mathsf{r}_\mathsf{s}}(\omega)\mathrm{d}\omega \tag{2.15}$$

Note that this quantity depends on the gain matrix L. The aim is to assess and minimize also the trace of covariance in Eq. (2.15) along with the trace of covariance of the state $\Sigma^2_{\varepsilon\varepsilon}$ to obtain the *learning phase driven observer.*

Refinement of optimization process

Minimizing $tr(\Sigma^2_{\mathsf{r}_\mathsf{s}\mathsf{r}_\mathsf{s}})$ means designing an observer that makes the post-fit residues converge to zero. This information must be managed carefully since it does not ensure the convergence of displacements throughout the structure and, generally, it may be conditioned by measurement noise. However, the minimization of $tr(\Sigma^2_{\mathsf{r}_\mathsf{s}\mathsf{r}_\mathsf{s}})$ could be very helpful in the case some measurements are available only in a learning stage since the resulting state observer would address the estimation to converge also in that points that are no longer directly monitored. Moreover, in a structural system it is also very difficult to quantify the process error and the minimization of the post-fit measurement residue can be used to guide towards a synthesis of an observer that also takes into account the collected data. The natural second-order

---

[2] The same PSD expressed in Eq. 2.14 can be expressed without defining y_r:

$$\begin{aligned}\Phi_{\mathsf{r}_\mathsf{s}\mathsf{r}_\mathsf{s}}(\omega) \quad &= \quad \Phi_{\mathsf{y}_\mathsf{s}\mathsf{y}_\mathsf{s}}(\omega) + \left(\tilde{\mathsf{S}}^\mathsf{s}(\omega)\tilde{\mathsf{H}}_O(\omega)\mathsf{L}\right)^* \Phi_{\mathsf{y}\mathsf{y}}(\omega)\left(\tilde{\mathsf{S}}^\mathsf{s}(\omega)\tilde{\mathsf{H}}_O(\omega)\mathsf{L}\right)^\mathsf{T} + \\ &\left(\tilde{\mathsf{S}}^\mathsf{s}(\omega)\tilde{\mathsf{H}}_O(\omega)\mathsf{L}\right)^* \Phi_{\mathsf{y}\mathsf{y}_\mathsf{s}}(\omega) + \Phi_{\mathsf{y}_\mathsf{s}\mathsf{y}}(\omega)\left(\tilde{\mathsf{S}}^\mathsf{s}(\omega)\tilde{\mathsf{H}}_O(\omega)\mathsf{L}\right)^\mathsf{T}\end{aligned} \tag{2.13}$$

observer proposed in such a way is synthesized by minimizing $tr(\Sigma^2_{\varepsilon\varepsilon})$ as well as $tr(\Sigma^2_{\mathsf{r_s r_s}})$ in a bi-objective optimization framework and can be stated as it follows:

- **design variables**. $\lambda \in \mathbb{R}^{N_o}$ lists the diagonal elements of $\Xi_a, \Xi_v, \Xi_d, \Lambda_a \Lambda_v$ and Λ_d;
- **objective functions**. The trace of $tr(\Sigma^2_{\mathsf{r_s r_s}})$ is considered along with $\Sigma^2_{\varepsilon\varepsilon}$:

$$\min_{\lambda \in \mathbb{R}^{N_o}} tr(\Sigma^2_{\varepsilon\varepsilon})(\lambda)$$
$$\min_{\lambda \in \mathbb{R}^{N_o}} tr(\Sigma^2_{\varepsilon\varepsilon})(\lambda)$$

- **constraints**. Again, the state observer must be stable:

$$Re\Big[poles(\tilde{\mathsf{H}}_O^{-1})\Big] < 0$$

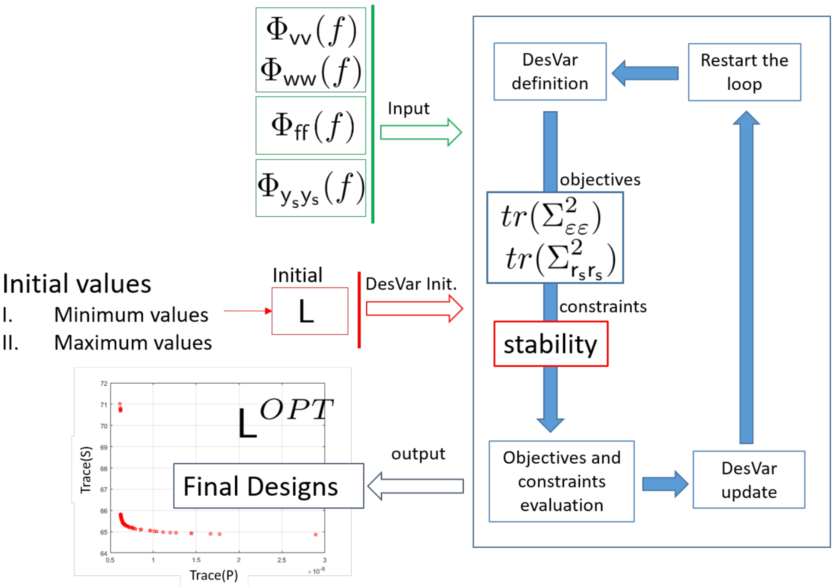

Figure 2.4: Bi-objective optimization process loop.

In Fig. 2.4 some differences arise than Fig. 2.3. Indeed, according to Eq. (2.14), also $\Phi_{\mathsf{y_s y_s}}(\omega)$ should be provided. Moreover, being two objectives, the optimal designs will be distributed on the Pareto frontier. It is worth stating that the engineering sensitivity will guide the choice of the best final design among all the solutions. The user criteria depends on the reliance on the description of the statistics assigned to noises and external forces with respect to experimental data.

2.3.2 Frequency-adaptive optimal observer

The other proposed approach concerns the design of a frequency-dependent observer. In Sec. 1.2.2, the covariance is obtained by integrating the PSDs of the state error over the frequencies. If the gain matrix is constant in time (and consequently in frequency), this implies that the optimization tends to minimize the state error globally by giving more weight to the most excited frequencies. Consequently, some dynamics result extremely penalized. This issue can be summarized by the following preposition:

- if the predicted input (assigned by means of $\Phi_{\mathsf{ff}}(\omega)$) has a dominant frequency-band, it means that the observer will be synthesized by only focusing on that band, thus neglecting the others.
- if the sensor noise is frequency-dependent (*e.g.* accelerometers have an operating range that excludes low frequencies), a constant observer is not able to give more gain to those sensors that are less noisy for a specific frequency value. Rather, the importance of measurements is averaged over the frequency domain.

Considering a general second order system in the form of Eq. (1.23) and the observer in Eq. (1.48), two possible approaches to overcome the previous issue will be introduced. Defining a gain matrix as a function of the frequency, the observer in Eq. (1.48) is recast by means of convolution product:

$$\mathsf{M}\ddot{\hat{\mathsf{q}}} + \mathsf{D}\dot{\hat{\mathsf{q}}} + \mathsf{K}\hat{\mathsf{q}} = \mathfrak{F}^{-1}\left(\tilde{\mathsf{L}}(\omega)(\tilde{\mathsf{y}} - \tilde{\mathsf{S}}\tilde{\hat{\mathsf{q}}})\right) \tag{2.16}$$

Consequently, the error dynamics $\varepsilon = \mathsf{q} - \hat{\mathsf{q}}$ is expressed by

$$\mathsf{M}\ddot{\varepsilon} + \mathsf{D}\dot{\varepsilon} + \mathsf{K}\varepsilon + \mathfrak{F}^{-1}\left(\tilde{\mathsf{L}}(\omega)\tilde{\mathsf{S}}\tilde{\varepsilon}\right) = \mathsf{f} + \mathsf{w} - \mathfrak{F}^{-1}\left(\tilde{\mathsf{L}}(\omega)\tilde{\mathsf{v}}\right) \tag{2.17}$$

and its Fourier transform yields

$$\tilde{\varepsilon} = \tilde{\mathsf{H}}_O(\omega)(\tilde{\mathsf{f}} + \tilde{\mathsf{w}} - \tilde{\mathsf{L}}(\omega)\tilde{\mathsf{v}}) \tag{2.18}$$

where the transfer function depends on the frequency dependent gain matrix $\tilde{\mathsf{L}}(\omega)$:

$$\tilde{\mathsf{H}}_O(\omega) = [-\omega^2\mathsf{M} + i\omega\mathsf{D} + \mathsf{K} + \tilde{\mathsf{L}}(\omega)\tilde{\mathsf{S}}]^{-1} \tag{2.19}$$

Under the assumption of uncorrelated noises and external forces, Eq. 2.18 yields the following PSD:

$$\Phi_{\varepsilon\varepsilon}(\omega) = \tilde{\mathsf{H}}_O^*(\omega)(\Phi_{\mathsf{ff}}(\omega) + \Phi_{\mathsf{ww}}(\omega) - \tilde{\mathsf{L}}(\omega)^*\Phi_{\mathsf{vv}}(\omega)\tilde{\mathsf{L}}(\omega)^{\mathsf{T}})\tilde{\mathsf{H}}_O^{\mathsf{T}}(\omega) \tag{2.20}$$

where Φ_{ff} , Φ_{ww} and Φ_{vv} are identified as in Sec. 2.1.1. Again, the gain is synthesized by minimizing the trace of $\Sigma^2_{\varepsilon\varepsilon}$ in Eq. (1.55). The inverse transform of Eq. (2.16) the time domain observation system

$$\mathsf{M}\ddot{\hat{\mathsf{q}}} + \mathsf{D}\dot{\hat{\mathsf{q}}} + \mathsf{K}\hat{\mathsf{q}} = \mathsf{L}(t) * \mathsf{r}(t) = \int_0^t \mathsf{L}(t-\tau)\mathsf{r}(\tau)\mathrm{d}\tau \tag{2.21}$$

where

$$\mathsf{L}(t) = \mathfrak{F}^{-1}\{\tilde{\mathsf{L}}(\omega)\} \tag{2.22}$$

The convolution in Eq. (2.21) implies a causal relationship between the residual vector r and the estimation $\hat{\mathsf{q}}$. The causality is ensured only if $\tilde{\mathsf{H}}_O$ respects the Kramers-Kronig principle. For this purpose, $\tilde{\mathsf{L}}(\omega)$ must be defined by means of an analytic function. Indeed, it is not possible to define a gain matrix independently for each frequency line. Generally, an analytical expression of $\tilde{\mathsf{L}}(\omega)$ can be obtained by means a rational-polynomial expansion as follows:

$$\tilde{\mathsf{L}}(\omega) = \left(\sum_{n=0}^{N}(i\omega)^n\mathsf{D}_n\right)^{-1}\left(\sum_{m=0}^{M}(i\omega)^m\mathsf{N}_m\right) \qquad N < M \tag{2.23}$$

where D_n and N_m are the coefficient matrices of this approximation.

Although the approach seems to be appealing, it results to be inapplicable since $N + M$ gain matrices are required, thus obtaining an excessive number of free parameters to perform the optimization. In practical applications, the shape of the observer could be suggested by control theory by using a *Proportional Integrative Derivative* (PID) observer as it follows

$$\tilde{\mathsf{L}}(\omega) = \mathsf{L}_P + \mathsf{L}_I/(i\omega) + i\omega\mathsf{L}_D \tag{2.24}$$

2.3.3 A multi-scale observer

To overcome the previous issue, the multi-scale observer is presented below. As first, the basic notions about wavelet multi-resolution analysis (WMRA) will be provided. Then this decomposition technique will be exploited to synthesize an observer tailored for each characteristic time scale of the response.

Introduction to multi-resolution analysis

In the last decades, wavelet transform has revealed as one of the most important tools for signal processing and its use have involved a great number of applications. In this context, the so called wavelet multi-resolution analysis is an appealing tool able to decompose in real time a generic signal into a certain number of orthogonal sub-signals defined in different time-scales. It follows that each of these sub-signals are defined in a precise frequency range. In control theory, wavelet multi-resolution analysis has been employed as signal decomposition tool in order to get an effective frequency-dependent control strategy. Especially, Parvez et al. [22] used WMRA to decompose the error signal (the residue in control theory) in different scales so obtaining a controller that behaves much better than classical PID in terms of its ability to provide smooth control signal, better disturbance and noise rejection.

The section goal concerns the use of WMRA for a state observation strategy based on the synthesis of several observers, each specific for the different measurement time-scale. In the main body of the thesis only the basic concepts of WMRA will be provided. However, a deeper description of wavelet multi-resolution analysis is provided in Appendix A.

According with the level N of the decomposition, WMRA provides a decomposition of the signal $x(t)$ in one approximation $x^{(a_N)}$, that is, the sub-signal at lower frequency and N several details $x^{(d_j)}$ with different time-scales, such that:

$$x(t) = x^{(a_N)} + \sum_{j=1}^{N} x^{(d_j)} \tag{2.25}$$

These signals are obtained through Quadrature Mirror Filters, that is, a discrete-time Finite Impulse Response (FIR) filters that employs the definition of discrete wavelet transform. Fig. 2.5 shows the frequency content of the filters associated to a 3-level decomposition. By observing Fig. 2.5, the main features of WMRA are here summarized:

- according to the level N required, the mechanism works by recursively splitting the approximation (*e.g.*, , $x = x^{(a_1)} + x^{(d_1)}$, $x^{(a_1)} = x^{(a_2)} + x^{(d_2)}$, $x^{(a_2)} = x^{(a_3)} + x^{(d_3)}$, and so on).
- The increase of the scale parameter corresponds to a shift to a lower frequency

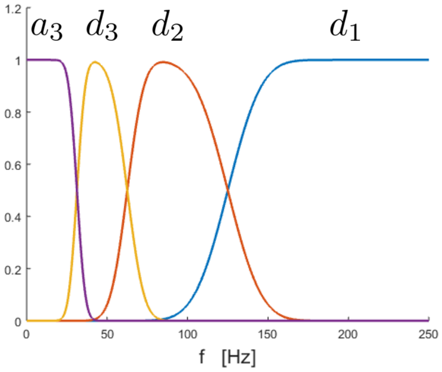

Figure 2.5: Frequency domain representation of 3-level WMRA with *db12* wavelets.

band with a halved width. This is due to the dyadic nature of the discrete wavelet transform.

- Although the signals are orthogonal to each other, there is an overlap between the various scales. This detail must be taken into account for further considerations following.

Error dynamics

The system dynamics in Eq. (1.48) is recast by means of WMRA decomposition of Eq. (2.25) as it follows:

$$\begin{aligned}
&\mathsf{M}\left(\ddot{\mathsf{q}}^{(a_N)}+\sum_{j=1}^{N}\ddot{\mathsf{q}}^{(d_j)}\right)+\mathsf{D}\left(\dot{\mathsf{q}}^{(a_N)}+\sum_{j=1}^{N}\dot{\mathsf{q}}^{(d_j)}\right)+\mathsf{K}\left(\mathsf{q}^{(a_N)}+\sum_{j=1}^{N}\mathsf{q}^{(d_j)}\right)=\\
&\left(\mathsf{f}^{(a_N)}+\sum_{j=1}^{N}\mathsf{f}^{(d_j)}\right)+\left(\mathsf{w}^{(a_N)}+\sum_{j=1}^{N}\mathsf{w}^{(d_j)}\right)\\
&\left(\mathsf{y}^{(a_N)}+\sum_{j=1}^{N}\mathsf{y}^{(d_j)}\right)=\mathsf{S}(t)*\left(\mathsf{q}^{(a_N)}+\sum_{j=1}^{N}\mathsf{q}^{(d_j)}\right)+\left(\mathsf{v}^{(a_N)}+\sum_{j=1}^{N}\mathsf{v}^{(d_j)}\right)
\end{aligned} \tag{2.26}$$

In a similar way, an observation strategy based on WMRA is introduced where the residues at different time-scales are applied to several gain matrices tailored for each time scale as it follows:

$$\mathsf{M}\Big(\ddot{\hat{\mathsf{q}}}^{(a_N)}+\sum_{j=1}^{N}\ddot{\hat{\mathsf{q}}}^{(d_j)}\Big)+\mathsf{D}\Big(\dot{\hat{\mathsf{q}}}^{(a_N)}+\sum_{j=1}^{N}\dot{\hat{\mathsf{q}}}^{(d_j)}\Big)+\mathsf{K}\Big(\hat{\mathsf{q}}^{(a_N)}+\sum_{j=1}^{N}\hat{\mathsf{q}}^{(d_j)}\Big)=$$
$$\Big(\mathsf{L}^{(N+1)}(t)*\mathsf{r}^{(a_N)}+\sum_{j=1}^{N}\mathsf{L}^{(j)}(t)*\mathsf{r}^{(d_j)}\Big) \tag{2.27}$$

To get an optimal observer we need to design $\mathsf{L}^{(N+1)}$ (associated to the approximation) and $\mathsf{L}^{(j)}$ (associated to the details) able to minimize the state error for each residual sub-signal $\mathsf{r}^{(d_j)}$. Eqs. (2.26,2.27) provide the state error dynamics in the following form:

$$\Big[\mathsf{M}\ddot{\varepsilon}^{(a_N)}+\mathsf{D}\dot{\varepsilon}^{(a_N)}+\mathsf{K}\varepsilon^{(a_N)}+\mathsf{L}^{(N+1)}(t)*(\mathsf{S}(t)*\varepsilon^{(a_N)})-\mathsf{f}^{(a_N)} \tag{2.28}$$
$$-\mathsf{w}^{(a_N)}-\mathsf{L}^{(N+1)}(t)*\mathsf{v}^{(a_N)}\Big]+\sum_{j=1}^{\infty}\Big[\mathsf{M}\ddot{\varepsilon}^{(d_j)}+\mathsf{D}\dot{\varepsilon}^{(d_j)}+\mathsf{K}\varepsilon^{(d_j)}+$$
$$\mathsf{L}^{(j)}(t)*(\mathsf{S}(t)*\varepsilon^{(d_j)})-\mathsf{f}^{(d_j)}-\mathsf{w}^{(d_j)}-\mathsf{L}^{(j)}(t)*\mathsf{v}^{(d_j)}\Big]=0$$

The rest of the section aims to provide a methods to synthesize the gain matrices.

Hypothesis on the spectral decomposition

Next, the following conjecture is assumed. In order to obtain an observer able to feel the vibration dynamics at the different time-scales involved, it is desirable to assume all the quantities in squared brackets in Eq. (2.28) equal to zero. Under this hypothesis, all $\mathsf{L}^{(j)}$ can be estimated in a straightforward way, since Eq. (2.28) can be decomposed as follows:

$$\mathsf{M}\ddot{\varepsilon}^{(a_N)}+\mathsf{D}\dot{\varepsilon}^{(a_N)}+\mathsf{K}\varepsilon^{(a_N)}+\mathsf{L}^{(N+1)}(t)*(\mathsf{S}(t)*\varepsilon^{(a_N)})= \tag{2.29a}$$
$$\mathsf{f}^{(a_N)}+\mathsf{w}^{(a_N)}+\mathsf{L}^{(N+1)}(t)*\mathsf{v}^{(a_N)}$$
$$\mathsf{M}\ddot{\varepsilon}^{(d_j)}+\mathsf{D}\dot{\varepsilon}^{(d_j)}+\mathsf{K}\varepsilon^{(d_j)}+\mathsf{L}^{(j)}(t)*(\mathsf{S}(t)*\varepsilon^{(d_j)})= \tag{2.29b}$$
$$\mathsf{f}^{(d_j)}+\mathsf{w}^{(d_j)}+\mathsf{L}^{(j)}(t)*\mathsf{v}^{(d_j)} \qquad j=1...N$$

Fourier transforms of Eqs. (2.29a, 2.29b) are:

$$\tilde{\varepsilon}^{(a_N)}=\tilde{\mathsf{H}}_O^{(N+1)}(\omega)(\tilde{\mathsf{f}}^{(a_N)}+\tilde{\mathsf{w}}^{(a_N)}-\tilde{\mathsf{L}}^{(N+1)}(\omega)\tilde{\mathsf{v}}^{(a_N)}) \tag{2.30a}$$
$$\tilde{\varepsilon}^{(d_j)}=\tilde{\mathsf{H}}_O^{(j)}(\omega)(\tilde{\mathsf{f}}^{(d_j)}+\tilde{\mathsf{w}}^{(d_j)}-\tilde{\mathsf{L}}^{(j)}(\omega)\tilde{\mathsf{v}}^{(d_j)}) \tag{2.30b}$$

If the hypothesis of uncorrelated forces and noises is verified, Eqs. (2.30a, 2.30b) yield the PSDs of the approximation $\varepsilon^{(a_N)}$ and details $\varepsilon^{(d_j)}$ errors:

$$\begin{aligned}\Phi_{\varepsilon^{(a_N)}\varepsilon^{(a_N)}}(\omega) = \tilde{\mathsf{H}}_O^{(N+1)*}(\omega)(\Phi_{\mathsf{f}^{(a_N)}\mathsf{f}^{(a_N)}}(\omega) + \Phi_{\mathsf{w}^{(a_N)}\mathsf{w}^{(a_N)}}(\omega) - \\ \tilde{\mathsf{L}}^{(N+1)*}(\omega)\Phi_{\mathsf{v}^{(a_N)}\mathsf{v}^{(a_N)}}(\omega)\tilde{\mathsf{L}}^{(N+1)\mathsf{T}}(\omega))\tilde{\mathsf{H}}_O^{(N+1)\mathsf{T}}(\omega)\end{aligned} \tag{2.31a}$$

$$\begin{aligned}\Phi_{\varepsilon^{(d_j)}\varepsilon^{(d_j)}}(\omega) = \tilde{\mathsf{H}}_O^{(j)*}(\omega)(\Phi_{\mathsf{f}^{(d_j)}\mathsf{f}^{(d_j)}}(\omega) + \Phi_{\mathsf{w}^{(d_j)}\mathsf{w}^{(d_j)}}(\omega) - \\ \tilde{\mathsf{L}}^{(j)*}(\omega)\Phi_{\mathsf{v}^{(d_j)}\mathsf{v}^{(d_j)}}(\omega)\tilde{\mathsf{L}}^{(j)\mathsf{T}}(\omega))\tilde{\mathsf{H}}_O^{(j)\mathsf{T}}(\omega)\end{aligned} \tag{2.31b}$$

where $\tilde{\mathsf{H}}_O^{(j)}$ is the $j-th$ observer transfer function obtained by means of the $j-th$ gain $\mathsf{L}^{(j)}$.

The power spectral densities $\Phi_{\mathsf{f}^{(d_j)}\mathsf{f}^{(d_j)}}$, $\Phi_{\mathsf{v}^{(d_j)}\mathsf{v}^{(d_j)}}$, $\Phi_{\mathsf{w}^{(d_j)}\mathsf{w}^{(d_j)}}$ (and the ones for the approximation) can be obtained by knowing the filter transfer function associated to each level ($\tilde{\varphi}^{(a_N)}$ and $\tilde{\varphi}^{(d_j)}$ in Fig. A.3), so having that the PSDs of subsignals are provided by:

$$\Phi_{\bullet^{(a_N)}\bullet^{(a_N)}}(\omega) = ||\tilde{\varphi}^{(a_N)}(\omega)||^2\Phi_{\bullet\bullet}(\omega) \tag{2.32a}$$

$$\Phi_{\bullet^{(a_N)}\bullet^{(d_j)}}(\omega) = ||\tilde{\varphi}^{(d_j)}(\omega)||^2\Phi_{\bullet\bullet}(\omega) \tag{2.32b}$$

The gain matrices $\mathsf{L}^{(j)}$ can be thus obtained by minimizing the covariances:

$$\Sigma_{\varepsilon\varepsilon}^{2(a_N)} = \int_{-\infty}^{+\infty} \Phi_{\varepsilon^{(a_N)}\varepsilon^{(a_N)}}(\omega)\mathrm{d}\omega \tag{2.33a}$$

$$\Sigma_{\varepsilon\varepsilon}^{2(d_j)} = \int_{-\infty}^{+\infty} \Phi_{\varepsilon^{(d_j)}\varepsilon^{(d_j)}}(\omega)\mathrm{d}\omega \tag{2.33b}$$

By respecting the hypothesis above it is possible to decompose Eq. (2.27) thus performing the following multi-scale observation:

$$\begin{aligned}\mathsf{M}\ddot{\hat{\mathsf{q}}}^{(a_N)} + \mathsf{D}\dot{\hat{\mathsf{q}}}^{(a_N)} + \mathsf{K}\hat{\mathsf{q}}^{(a_N)} + \mathsf{L}^{(N+1)}(t) * (\mathsf{S}(t) * \hat{\mathsf{q}}^{(a_N)}) = \\ \mathsf{L}^{(N+1)}(t) * \mathsf{y}^{(a_N)}\end{aligned} \tag{2.34a}$$

$$\begin{aligned}\mathsf{M}\ddot{\hat{\mathsf{q}}}^{(d_j)} + \mathsf{D}\dot{\hat{\mathsf{q}}}^{(d_j)} + \mathsf{K}\hat{\mathsf{q}}^{(d_j)} + \mathsf{L}^{(j)}(t) * (\mathsf{S}(t) * \hat{\mathsf{q}}^{(d_j)}) = \\ +\mathsf{L}^{(j)}(t) * \mathsf{y}^{(d_j)} \qquad j = 1...N\end{aligned} \tag{2.34b}$$

However, this conjecture is not mathematically consistent. Indeed, although the following relationships are always valid due to the orthogonality between subspaces of different scales,

$$\langle \varepsilon^{(d_j)}, \varepsilon^{(d_l)} \rangle_t = 0 \qquad \forall j \neq l \tag{2.35a}$$

$$\langle \varepsilon^{(a_N)}, \varepsilon^{(d_j)} \rangle_t = 0 \qquad j = 1, ..., N \tag{2.35b}$$

the following scalar products

$$\langle \varepsilon^{(d_j)}, \dot{\varepsilon}^{(d_l)} \rangle_t \neq 0 \tag{2.36a}$$

$$\langle \varepsilon^{(a_N)}, \dot{\varepsilon}^{(d_j)} \rangle_t \neq 0 \tag{2.36b}$$

$$\langle \varepsilon^{(d_j)}, \ddot{\varepsilon}^{(d_l)} \rangle_t \neq 0 \tag{2.36c}$$

$$\langle \varepsilon^{(a_N)}, \ddot{\varepsilon}^{(d_j)} \rangle_t \neq 0 \tag{2.36d}$$

$$\langle \varepsilon^{(d_j)}, \mathsf{L}^{(l)}(t) * (\mathsf{S}(t) * \varepsilon^{(d_l)}) \rangle_t \neq 0 \tag{2.36e}$$

$$\langle \varepsilon^{(a_N)}, \mathsf{L}^{(j)}(t) * (\mathsf{S}(t) * \varepsilon^{(d_j)}) \rangle_t \neq 0 \tag{2.36f}$$

$$\langle \varepsilon^{(d_j)}, \mathsf{L}^{(l)}(t) * \mathsf{v}^{(d_l)} \rangle_t \neq 0 \tag{2.36g}$$

$$\langle \varepsilon^{(a_N)}, \mathsf{L}^{(j)}(t) * \mathsf{v}^{(d_j)} \rangle_t \neq 0 \tag{2.36h}$$

do not vanish implying that Eqs. (2.34a, 2.34b) and, in turn, Eqs. (2.31a, 2.31b) are provided by a very strong approximation. Generally, any non-constant time-frequency operator applied to a generic signal $x^{(d_j)}(t)$ results in an output that is not orthogonal to the other sub-signals[3]. This issue implies that this synthesis process provides a **sub-optimal** observer.

However, it can be stated that the multi-scale observer will be as optimal as we get a synthesis of the state observers $\mathsf{L}^{(j)}$ such that:

$$\langle \tilde{\varepsilon}^{(d_j)}(\omega), \tilde{\mathsf{H}}_O^{(l)}(\omega)(\tilde{\mathsf{f}}^{(d_l)} + \tilde{\mathsf{w}}^{(d_l)} - \tilde{\mathsf{L}}^{(l)}(\omega)\tilde{\mathsf{v}}^{(d_l)}) \rangle_\omega \to 0 \qquad \forall j \neq l \tag{2.37a}$$

$$\langle \tilde{\varepsilon}^{(a_N)}(\omega), \tilde{\mathsf{H}}_O^{(l)}(\omega)(\tilde{\mathsf{f}}^{(d_l)} + \tilde{\mathsf{w}}^{(d_l)} - \tilde{\mathsf{L}}^{(l)}(\omega)\tilde{\mathsf{v}}^{(d_l)}) \rangle_\omega \to 0 \tag{2.37b}$$

In order to make the above relationships converge making the observer actually **optimal**, the necessary condition is the synthesis of a high-gain observer such that in the frequency range interested by the $j-th$ detail level, it provides an instantaneous estimation with respect to the measurements (see Sec. 1.2.2). It suggests to use a low order gain matrices $\tilde{\mathsf{L}}^{(j)}(\omega)$, besides the assumption in Sec. 2.2.3 However, in order to provide the dynamics of the observer of further damping (in order to smooth the

---

[3] Note that the orthogonality in the previous equations is practically respected only if $|j-l| > 1$, namely, when the scalar product is performed between two signal that do not belong to two contiguous scales.

peaks of the observer dynamics poles), a quasi-steady gain matrix is considered:

$$\tilde{\mathsf{L}}^{(j)}(\omega) = \mathsf{L}_0^{(j)} + i\omega \mathsf{L}_1^{(j)} \tag{2.38}$$

where it is recommended that $\mathsf{L}_0^{(j)} \gg i\omega\mathsf{L}_1^{(j)}$ in the range of frequencies interested by level j. Under the hypothesis in Eq. 2.29, the state estimation can be obtained from the sum of the estimations obtained at the various levels (as illustrated in Fig.2.6):

$$\hat{\mathsf{q}} = \sum_{j=1}^{N+1} \hat{\mathsf{q}}^{(j)} \tag{2.39a}$$

$$\hat{\mathsf{q}}^{(N+1)} = \mathsf{H}_O^{(N+1)} * \left(\mathsf{L}^{(N+1)}(t) * \mathsf{y}^{(a_N)}\right) \tag{2.39b}$$

$$\hat{\mathsf{q}}^{(j)} = \mathsf{H}_O^{(j)} * \left(\mathsf{L}^{(j)}(t) * \mathsf{y}^{(d_j)}\right) \qquad j = 1 \ldots N \tag{2.39c}$$

In Eq. 2.39 it has been referred as $\hat{\mathsf{q}}^{(j)}$ and $\hat{\mathsf{q}}^{(N+1)}$ instead of $\hat{\mathsf{q}}^{(d_j)}$ and $\hat{\mathsf{q}}^{(N+1)}$ since, for the reason mentioned above in this section, $\hat{\mathsf{q}}^{(j)}$ is not necessarily the $j-$th detail of $\hat{\mathsf{q}}$. However, the assumption in Eq. (2.37) is usually respected when dealing with structural systems with an adequate number of sensors with a good signal to noise ratio, thus having that $\hat{\mathsf{q}}^{(j)} \rightarrow \hat{\mathsf{q}}^{(d_j)}$ and $\hat{\mathsf{q}}^{(N+1)} \rightarrow \hat{\mathsf{q}}^{(a_N)}$.

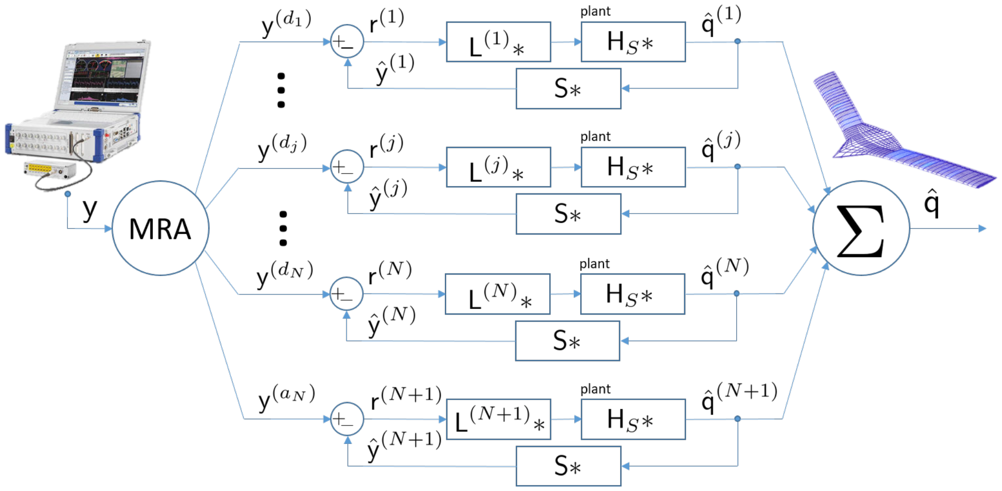

Figure 2.6: Block diagram related to the multi-scale observer.

2.4 Quality indicators

The fidelity level of the observation process is generally addressed by means of two different functions called *Time Response Assurance Criterium* (TRAC) and *Frequency Response Assurance Criterium* (FRAC) introduced in [4, 37]. These functions are a generalization of the concept of modal assurance criterion (MAC) for signal arrays in time and frequency domain. By taking into account two general time dependent arrays $\mathsf{a}(t)$ and $\mathsf{b}(t)$ and their Fourier transform, TRAC and FRAC are defined as below:

$$TRAC_{\mathsf{ab}}(t) = \frac{\| \mathsf{a}(t)^{\mathsf{T}}\ \mathsf{W}\ \mathsf{b}(t) \|^2}{(\mathsf{a}(t)^{\mathsf{T}}\ \mathsf{W}\ \mathsf{a}(t))(\mathsf{b}(t)^{\mathsf{T}}\ \mathsf{W}\ \mathsf{b}(t))} \tag{2.40a}$$

$$FRAC_{\mathsf{ab}}(f) = \frac{\| \tilde{\mathsf{a}}(f)^{\mathsf{H}}\ \mathsf{W}\ \tilde{\mathsf{b}}(f) \|^2}{(\tilde{\mathsf{a}}(f)^{\mathsf{H}}\ \mathsf{W}\ \tilde{\mathsf{a}}(f))(\tilde{\mathsf{b}}(f)^{\mathsf{H}}\ \mathsf{W}\ \tilde{\mathsf{b}}(f))} \tag{2.40b}$$

where W is a user defined weight function. The functions above represent, respectively, the similarity of the signal array a and b with an appropriate indicator in time and frequency domain. The values of these functions are limited in a range between 0 and 1. This property makes these functions good candidates for being considered as quality indicators in time and frequency. The average of the values over time $\overline{TRAC}_{\mathsf{ab}}$ and frequency $\overline{FRAC}_{\mathsf{ab}}$ in the interest range are assumed as global indicators for the quality of the estimation as a function of the interest parameters of the system such as number and distribution of sensors. When the observation process is assessed on simulated data, we know the exact behavior of the system beyond process and measurement noises. In these case studies TRAC and FRAC will be assessed directly on the modal coordinates (our state) that represent a complete and sufficient set of informations to evaluate the quality of the observation process.

$$\begin{aligned} \mathsf{a} &= \mathsf{q} \\ \mathsf{b} &= \hat{\mathsf{q}} \\ \mathsf{W} &= \mathsf{M} \end{aligned}$$

where the mass matrix is used as weight, allowing to give greater importance to those DoFs that are more *massive*. Thus, this leads to give less weight to the degrees of freedom that have less inertia and influence less the structural dynamics.

On the other hand, when the observation is upon experimental cases, the real behavior of the structure is always hidden. In such cases this assessment is carried out on the Control Meas. defined in Sec. 2.1.3:

$$\begin{aligned} \mathsf{a} &= \mathsf{y_c} \\ \mathsf{b} &= \hat{\mathsf{y}}_\mathsf{c} \\ \mathsf{W} &= \mathbf{\mathsf{I}} \end{aligned}$$

where the identity matrix is assumed as weight.

Chapter 3

Application to a scaled elastic model of a catamaran

The developed approach for loads and elastic deflection field estimation is first applied to the test data collected on the catamaran scaled model (see Fig. 3.1). In this chapter, first the reference physical model is introduced in Sec. 3.1 in terms of its principal features and Finite Element description; subsequently in Sec. 3.2 the estimation procedure is customized to fit the needs of the present case study. Finally, the main results concerning three different runs are shown in Sec. 3.3. The chapter ends with a convergence analysis on the number of sensors employed for the observation. An application of cumulative damage estimation based on the results of this chapter is provided in Appendix C where the stress estimation is used to enhance the computation of fatigue life accumulated by the present experimental model during the towing tests taken into consideration.

Figure 3.1: Experimental model under the carriage.

3.1 Physical model description

The elastically scaled model of catamaran that will be the object of this analysis is a model used to study particular fluid-structure interaction phenomena occurring in the naval field. When dealing with hydroelastic behavior of this kind of structure, two main aspects must be considered: *i)* the perturbations to the fluid dynamic field introduced by the structure vibrations are generally orders of magnitude lower than the wave loads and the perturbations introduced by the rigid-body dynamics of the ship. This generally brings to the case of a one-way hydroelastic coupling; *ii)* the structure is submerged in a two-phase fluid. Hence, when a large portion of the hull surface (such as the wetdeck) slams to the free surface, it generates extreme loads to the structure. This phenomenon is referred as slamming (see Fig. 3.2).

The structure in question was built to study particular slamming phenomena that occur in the wetdeck region. The case study is specialized for a structure that has a flat wetdeck that is not able to absorb the impacts with the free surface in an optimal way. This feature makes this structure interesting for the present study due to the high loads involved. Moreover the construction complexity represents a step forward to the study of full-scale structures.

Figure 3.2: Slamming illustrated by combining five consecutive frames to provide an impression of the event in time.

3.1.1 The experimental model

The experimental model of the catamaran is built with the elastic backbone approach, whose goal is to decouple the structural and hydrodynamic functions of the structure. This technique involves the construction of a structural frame that scales the elastic behavior of the full-scale model [33] and a segmented hull, where the segments - rigidly connected to the backbone beams - transmit hydrodynamic forces

Variable	value
Mass	206.8 Kg
Length Overall	3.96 m
CoG	1.628 m
Pitch radius	1.143 m

Table 3.1: Main model parameters.

and moments. Moreover, the experimental model includes a segmented wetdeck connected to the transversal beams of the deck region to transmit the loads generated by slamming impacts. From Fig. 3.1 it is possible to observe the catamaran below carriage with its metallic backbone and hull segments. The main rigid-body characteristics of the model are listed in Tab. (3.1).

The backbone truss is made of aluminum and includes several structural components: two longitudinal beams, two transverse beams, a central beam in the symmetry plane, and two hinged beams near the bow to support the wetdeck as shown in Fig. 3.3.

The truss is connected to the segments by using stiff vertical elements called legs. The role of the hull segments is to transfer concentrated hydrodynamic forces to the elastic backbone via the legs. Each hull is divided into four segments as shown in Fig. 3.1. In order to ensure a certain stiffness and lightness, the segments are made with fiberglass laminate with a stiffening core material. The gaps between adjacent segments is made water-tight by using thin rubber straps. On the other hand, the wetdeck is made up by different materials such as fiberglass, wood and polylactide (PLA) in order to make it robust enough and, in turn, it is segmented in two parts, with length of 1/3 and 2/3 length overall, respectively for the forward and the backward part. The forward part, where all the slamming phenomena occur, is connected to the two hinged beams.

A great number of structural lab tests have been carried out on the model, such as static and vibration tests, that has been used to enhance the numerical model. These tests were performed also during the construction phase, involving different configurations and parts of the catamaran. The results concerning the vibration tests of the final configuration are shown in this dissertation. However, for a deeper insight refer to [35]. The experimental first six elastic mode shapes of the free-free structure with the corresponding natural frequencies and damping ratios are shown in Fig. 3.4. It is worth to notice that the free-free conditions have been reproduced by hanging the present model by means of 8 soft springs in order to keep the rigid-

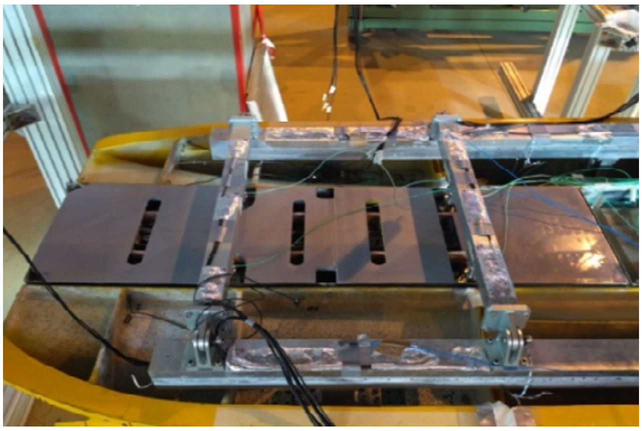

(a) Wetdeck view

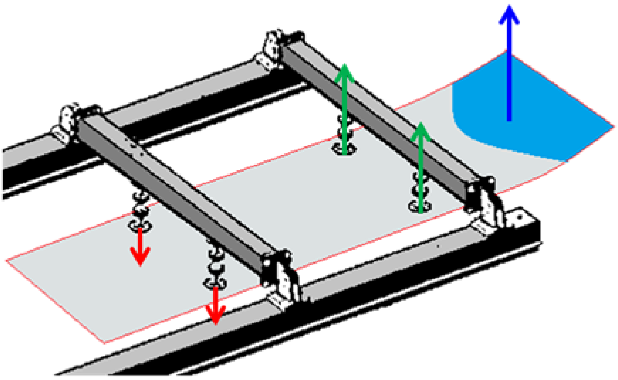

(b) Working principle of wetdeck balance

Figure 3.3: Wetdeck arrangement.

body modes frequencies lower than 2.0 Hz [33]. Finally, natural frequencies and modes have been computed by means of Polymax [1]. Further wet vibration tests have been carried out showing a general decrease of the natural frequencies. Fig. 3.5 shows the shapes of the wet modes associated to the dry-ones in Fig. 3.4. In caption it is possible to notice the change of the values of natural frequencies and damping ratios.

These wet vibration modal characteristics will provide further hints to assess the observation process and the behavior of the structure during the experimental towing tests. Finally, the experimental campaign has been performed at the CNR-INSEAN towing-tank basin Emilio Castagneto in Rome, that is a 220 m long, 9 m wide and

---

[1] Polymax is a standard method used in structural dynamics modal identification [34]

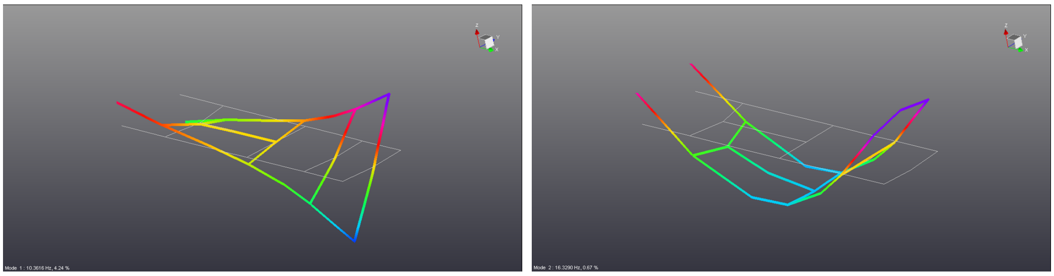

(a) $f_1 = 10.36$ Hz, $\zeta_1 = 0.042$ (b) $f_2 = 16.33$ Hz, $\zeta_2 = 0.007$

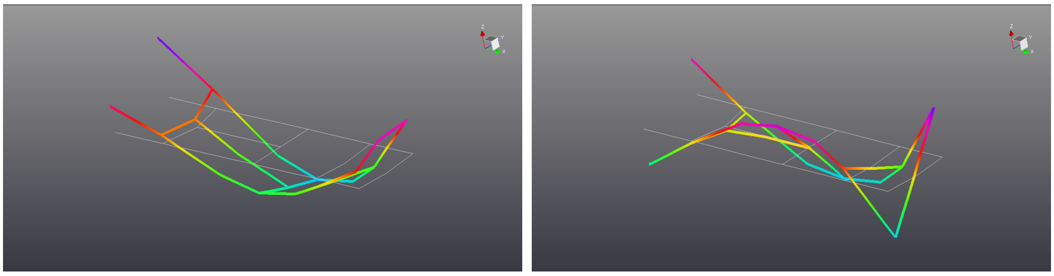

(c) $f_3 = 23.65$ Hz, $\zeta_3 = 0.019$ (d) $f_4 = 29.33$ Hz, $\zeta_4 = 0.015$

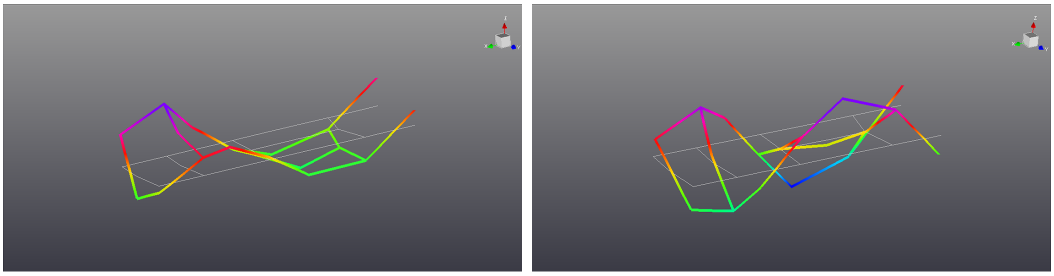

(e) $f_5 = 46.36$ Hz, $\zeta_5 = 0.008$ (f) $f_6 = 55.41$ Hz, $\zeta_6 = 0.01$

Figure 3.4: Natural modes from dry vibration tests.

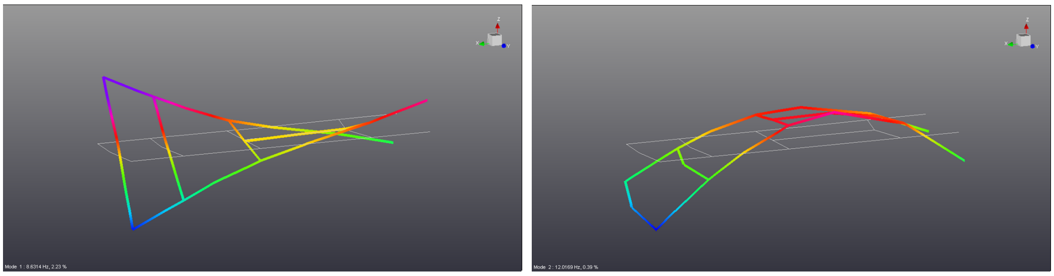

(a) $f_1 = 8.63$ Hz, $\zeta_1 = 0.022$

(b) $f_2 = 12.02$ Hz, $\zeta_2 = 0.004$

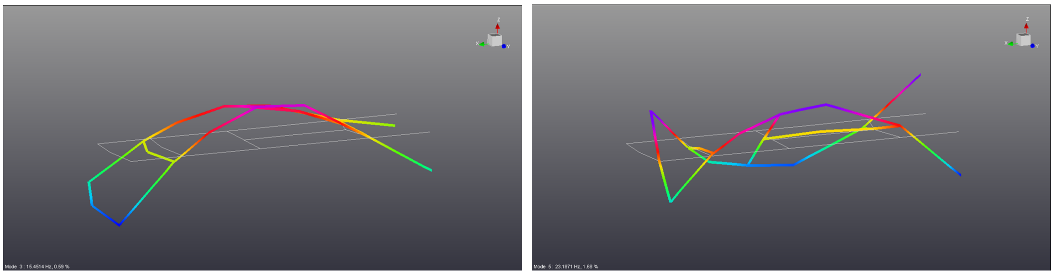

(c) $f_3 = 15.45$ Hz, $\zeta_3 = 0.006$

(d) $f_4 = 23.19$ Hz, $\zeta_5 = 0.017$

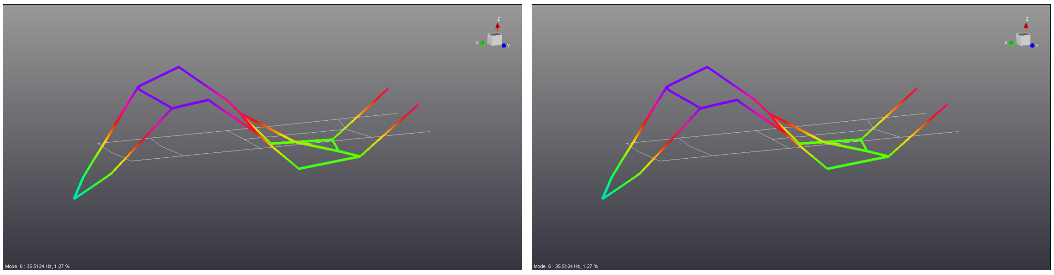

(e) $f_5 = 35.51$ Hz, $\zeta_6 = 0.013$

(f) $f_6 = 38.69$ Hz, $\zeta_6 = 0.011$

Figure 3.5: Natural modes from wet vibration tests.

3.5 m deep linear basin equipped with wavemaker system, able to generate regular waves and irregular sea according to different kind of spectra. The monitoring of the elastic deflections and the hydrodynamic loads is applied to a scaled physical vessel model tested in towing tank with on board acquired data. Some details about the towing system and the sensor layout follows. However, deeper insights about design and model assessments can be found in [33].

The model was towed by an eight-drive wheels carriage moving on a railroad guide. The complex towing system was such that it only allowed for heave and pitch modes by means of a barycentric hinge connected to vertically oriented linear bearing and a fork-type device at the stern.

3.1.2 Sensor layout

Heterogeneous data related to strains and rigid-body motion have been used. This vast amount of data has been recorded by means of a manifold of synchronized DEWE-43 modules. In particular, the sensor used for this analysis consists of 36 HBM strain gages spread to cover the whole backbone (see Fig. 3.6), and Rodymm Krypton optical system to measure all six rigid-body DOFs. The strain gages waterproof protection is shown in Fig. 3.7. The strain gage electrical calibration was carried out to provide the values of the strains. Static tests involving concentrated masses were performed to compare the measurements of local strains with those obtained via the finite element model reproducing the experimental set-up (loads and BCs of the calibration tests). Subsequently, the finite element model also provided conversion factors to obtain directly the local bending moments from the calibration

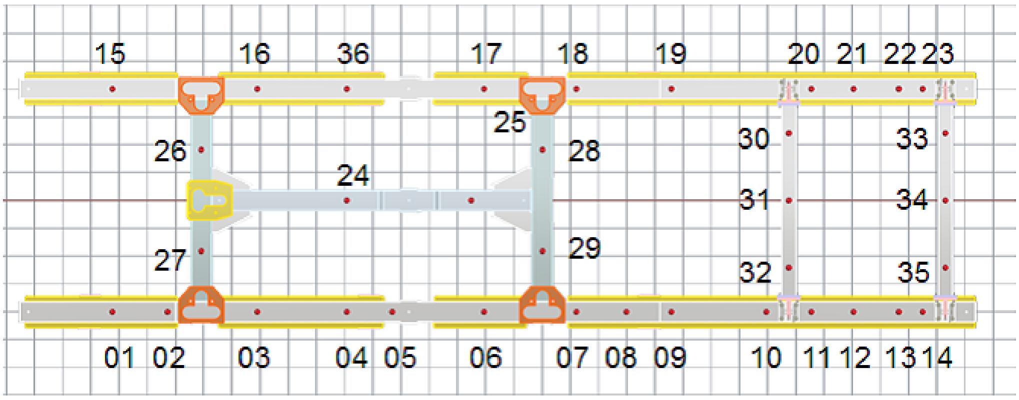

Figure 3.6: Strain gages layout.

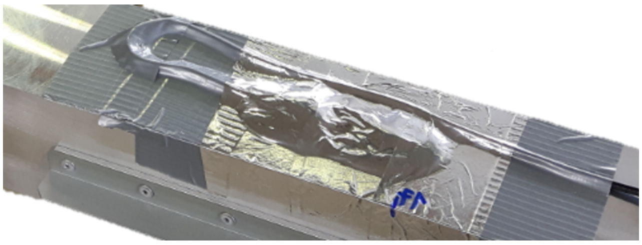

Figure 3.7: Strain gage arrangement with its water-proof protection.

Figure 3.8: Static experimental tests for strain gages calibration assessment.

tests. The experimental set-up for the strain-gages calibration assessment is shown in Fig. 3.8.

3.1.3 Numerical model description

The physical model introduced in Sec. 3.1.1 has been modeled by means of a detailed FE model. The development of present FE model has been particularly challenging since the mass properties are highly influenced by sensor layout and hull mass distribution. In order to obtain a numerical model as close to the experimental-one as possible, a model updating has been carried out in a cascade way by updating the structural components step by step during the model assembly stage. Hence, first the properties of backbone have been update by experimental vibration tests of the bare metallic frame up to a frequency of 120 Hz and then, an equivalent model of wetdeck has been generated in order to model its stiffness and mass. Eventually, a final updating is performed considering the whole structure in order to reach a good matching between the experimental dry modes and the first two numerical vibration modes.

The FE natural modes and frequencies are shown in Fig. 3.9. Notice that the

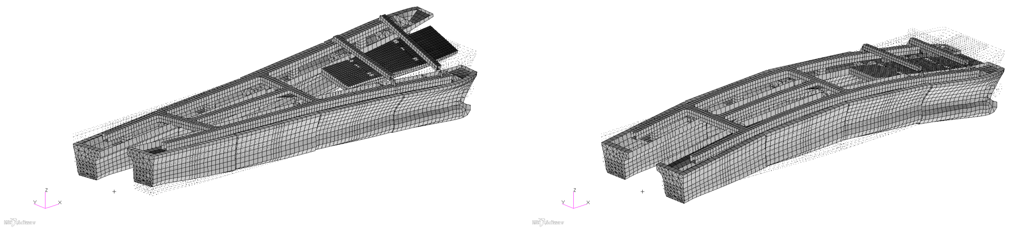

(a) $f_1 = 10.11$ Hz (b) $f_2 = 16.90$ Hz

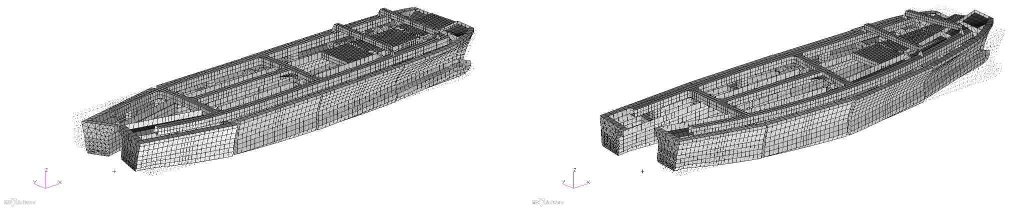

(c) $f_3 = 19.62$ Hz (d) $f_4 = 19.75$ Hz

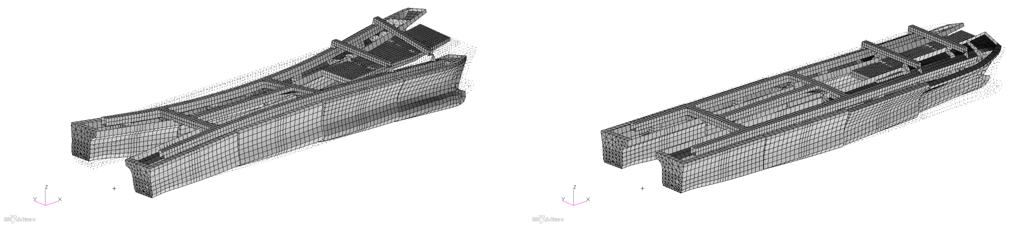

(e) $f_5 = 20.15$ Hz (f) $f_6 = 27.71$ Hz

Figure 3.9: Natural modes from dry numerical modal analysis.

first two modes and frequencies are very close to the experimental ones. Moreover it is possible to notice some vibration modes not identified in the experimental tests, such as the modes of the symmetric torsion of forward part of the trusses with frequency 27.71 Hz. Finally a modal damping matrix has been assumed by taking into account the experimental damping ratios.

3.2 Customization of the technique for the present case

This case study was used to test the first extension of the second-order observer introduced in Sec. 2.3.1, namely the *Learning phase driven observer*. Thus a constant observer in frequency is considered, but introducing the statistics of the stored measurements to enhance the convergence of the estimation.

In this section there will be illustrated how the Craig-Bampton method works for this case study along with the definition of the statistical properties.

3.2.1 The Craig-Bampton method

We have seen in Sec. 1.1.1 how obtaining a reduced order model through modal truncation and Craig-Bampton reduction method. In particular in this case study, we will use the Craig-Bampton method thanks to its ability to keep unchanged the information in some physical points (master DoFs) within the set of the reduced DoFs. These features allows for estimating the elastic deformations even when external forces are concentrated in space and time as in the case the catamaran scaled model where the structural frame exchanges concentrated forces with the segmented hull, the segmented wetdeck and the towing system. It is clear that an effective strategy to choose the master DoFs is to make coincide this DoFs with the characteristic points of the concentrated forces, that is, the interface characteristic points. Fig. 3.10 shows the concentrated loads that we are interested. The red and green arrows represent, respectively, the concentrated forces and moments. Concentrated rolling moments about the barycentric hinge and yaw bar are neglected. The set of generalized coordinates are associated to a set of non-canonical mode shapes, *i.e.* *boundary* and *fixed-boundary* modes. Example of these modes are illustrated in Fig. 3.11. For the present case study an amount of 23 master DoFs have been considered, that are chosen by selecting:

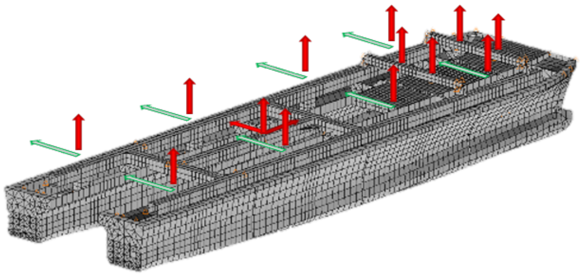

Figure 3.10: Concentrated forces acting on the catamaran scaled model.

- the vertical displacements and rotations about the transversal axis in each connection point between segments and backbone (8 points with DoFs 3 and 5, see Fig. 3.11a-b);

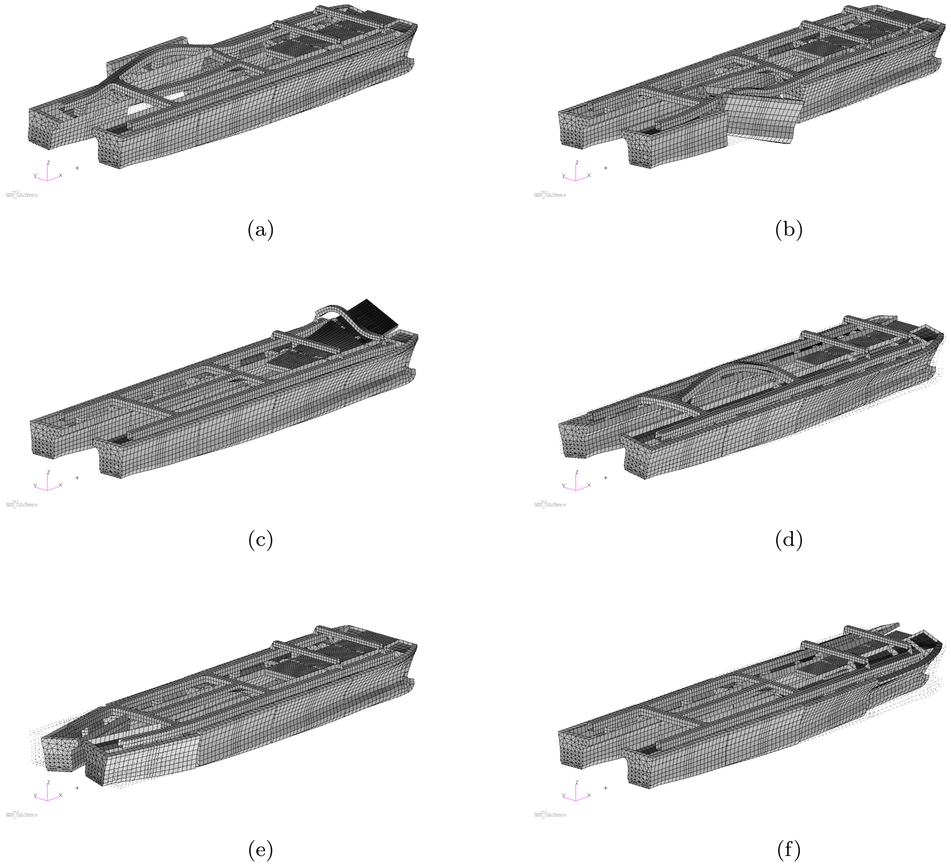

(a) (b)

(c) (d)

(e) (f)

Figure 3.11: Craig-Bampton modes: examples of *boundary modes* (a,b,c,d) and *fixed-boundary modes*(e,f)

- the vertical displacements in each connection point between the forward part of the wetdeck and relative bars (4 points with DoF 3, see Fig. 3.11c);
- the vertical and lateral displacements as well as the rotation about the vertical axis of the hinge point of the CoG (1 point with DoFs 2,3 and 6, see Fig. 3.11d).

These DoFs are introduced in order to have the minimum number of variables able to describe in a complete fashion the concentrated forces exchanged between the segmented hull and the backbone as well as the constraint force exchanged with the seakeeping bar. Then, a user dependent number of fixed-boundary modes is considered in order to have also a displacement space complete enough for the interest frequency range. For this case study an amount of 4 fixed-boundary modes have been considered.

3.2.2 Statistical properties

The spectral densities have been estimated by considering the recorded outputs during the towing tank campaign and recast in order to estimate the structural behavior of the model in an effective way. The **external forces** spectral densities are obtained by estimating the forces in a least-squares sense. To this end, the transfer function has been considered that concerns only the Master DoFs (namely a static condensation) of the system made symmetrical with respect to the xz plane:

$$\tilde{\hat{\mathsf{f}}}_{\mathsf{R}} = \left[-\omega^2 \hat{\mathsf{M}} + \hat{\mathsf{K}}\right]^{-1} \hat{\mathsf{C}}^{\dagger}\, \tilde{\mathsf{y}}$$

where $\hat{\mathsf{M}}$ and $\hat{\mathsf{K}}$ are the mass and stiffness matrices of the statically condensed system with xz plane symmetry constraints and $\hat{\mathsf{f}}_{\mathsf{R}}$ is the rough estimation of external forces that will be used to compute the spectral density. This approach allows to get a rough frequency representation of the external forces, that, subsequently are filtered in order to take into account only the wave loading in the hulls regions (low-pass filtering sufficiently below the first natural frequency $<$ 7 Hz) and the slamming phenomena on the wetdeck (below the first wetdeck local natural frequency $<$ 40 Hz). Once these forces are obtained, the power spectral density of external forces is computed:

$$\Phi_{\mathsf{ff}}(\omega) = \mathfrak{F}\Big\{ \int_0^t \hat{\mathsf{f}}_{\mathsf{R}}(t-\tau)\hat{\mathsf{f}}_{\mathsf{R}}(\tau)\mathrm{d}\tau \Big\}$$

However this power spectral density matrix takes into account only some features of the hydrodynamic forces (for instance the effects of added hydrodynamic mass and damping are not considered). As a consequence, it results into an estimation process that is sub-optimal. The uncertainties related the reconstruction of the external forces are introduced into the user-defined process noise along with other structural uncertainties.

On the other hand, the spectral densities of the **measurements** ($\Phi_{\mathsf{yy}}(f)$) are obtained by considering the rough data without any filtering process. The power spectral density of the **strain gage measurement noise** is assigned equal to $1e-1(\mu\text{strain})^2\text{Hz}^{-1}$ for each value of frequency up to the sampling frequency. This represents an upper limit experienced by observing the strain gages spectral densities of all the 36 sensors. On the other hand, the spectral densities of the **process noise** are such that the 10% of sum of the power of the estimated external forces is spread homogeneously on all the noise components. Since the process noise is artificially inserted and is not linked to any prior knowledge of the system, the assumption is that $||\mathsf{f}|| >> ||\mathsf{w}||$, so having that:

$$\hat{\mathsf{f}} = \mathsf{Lr}$$

For further detail about this assumption see Eq. (B.1) in Appendix B.

3.3 Illustrative results

The method presented in Sec. 3.2 have been applied on the experimental model of Sec. 3.1.1. The results that are shown below concern three runs for different sea condition that cause different dynamic responses. In towing-tank two different kind of sea conditions are considered. We will refer to regular sea conditions for those run where mono-frequency waves propagate along the tank. The main features are the wave height and the wave period. The response of the ship also depends on the speed. On the other hand, irregular sea conditions are featured by specific kind of spectra. Usually, for this type of trials, characteristic spectra are considered. In particular in this case the so called *JONSWAP* spectrum [36] has been considered that is featured by some parameters that approximate the oceanic sea conditions such as significant wave period and height.

$$\Phi_J(\omega) = 320\frac{H_{1/3}^2}{T_p^4}\omega^{-5}\exp\Big(\frac{-1950}{T_p^4}\omega^{-4}\Big)\gamma^A \tag{3.1}$$

Run	Speed [m/s]	wave height [m]	Period [s]	Type	Impact
1	1.779	0.1053	0.798	irregular	yes
2	1.779	0.035	2.410	regular	No
3	1.779	0.04	2.114	regular	yes

Table 3.2: Sea condition related to the considered runs.

where $H_{1/3}$ is the characteristic wave height, T_p is the peak period, γ is an opportune parameter whilst

$$A = \exp\left\{ -\left(\frac{\frac{\omega T_p}{2\pi} - 1}{\sigma\sqrt{2}} \right)^2 \right\} \tag{3.2}$$

where σ is another parameter that fits the PSD experimentally obtained in [36].

The runs that have been considered are listed in Tab. 3.2. Note that for irregular sea, wave properties refer to significant wave period/height $(T_p, H_{1/3})$. The three contemplated runs were performed by using the velocity of $1.779\, m/s$. The statistical properties concerning the responses of heave and pitch motions in each run are shown in Fig. 3.12 by means of their power spectral densities. On the other hand, the strain gage responses are shown in Fig. 3.13 considering the sum of the PSDs of the strain gage data. Rigid-body response shows peaks in correspondence of the encounter frequency and its multiples due to the nonlinearities introduced by the hull shape (see Fig. 3.12a). The seakeeping response may lead to intense slamming phenomena as illustrated in Fig. 3.2.

3.3.1 Estimation of forces and elastic deflections

In this section the response of the catamaran in terms of forces and elastic deflections to the sea conditions pointed out in Tab. 3.2 is analyzed and discussed. The results are illustrated with the best sensor configuration possible, *i.e.*, by considering that the sets of active, stored and control measurements coincide. In this way all measurements are used for the synthesis of gain matrix, state-updating and for evaluating the elastic displacements by means of quality indicators. Albeit the observer gain matrix can be computed for each of the sea condition above, the observer is synthesized by considering the statistical properties obtained from the irregular sea case (Run 1). In this way, the results relating the other two tests in regular sea conditions represent a qualitative assessment of the methodology robustness.

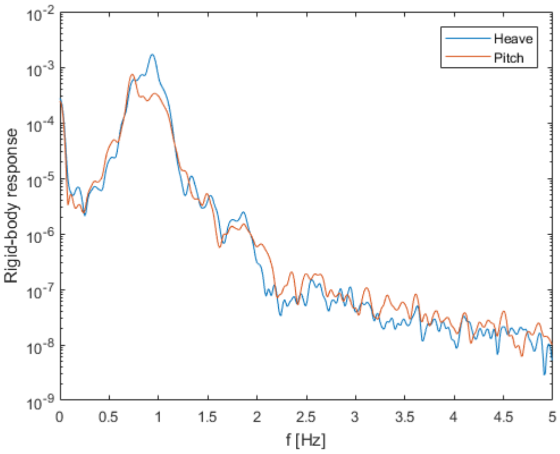

(a) Run 1

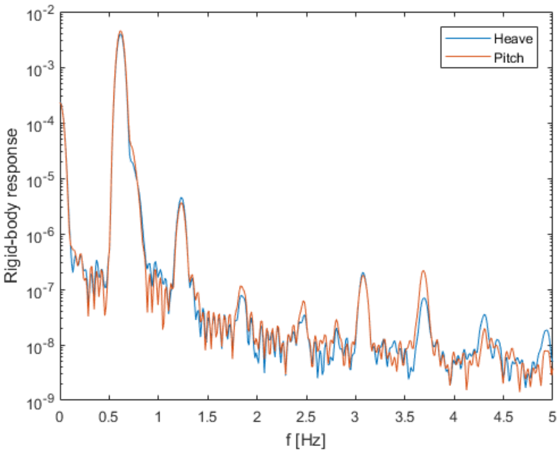

(b) Run 2

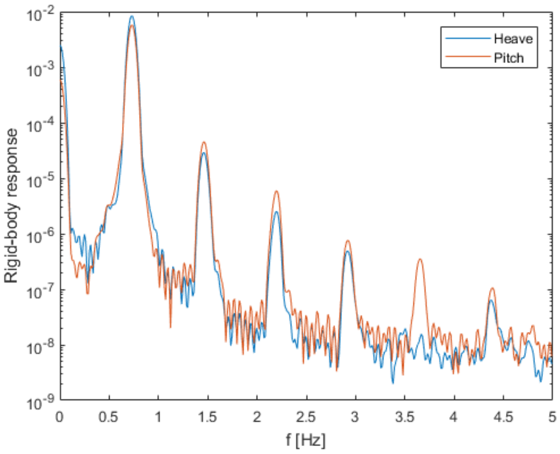

(c) Run 3

Figure 3.12: Power spectral densities of Heave and Pitch responses.

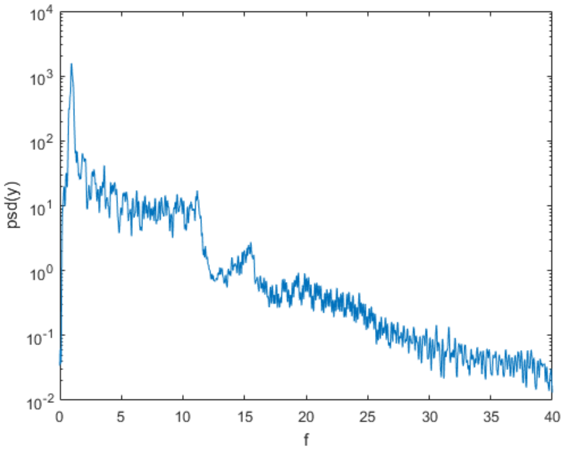

(a) Run 1

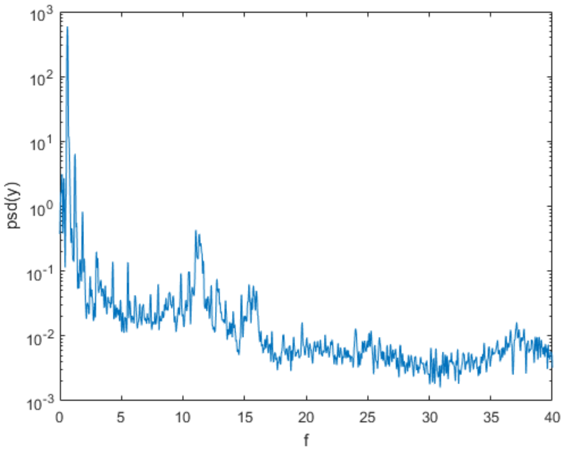

(b) Run 2

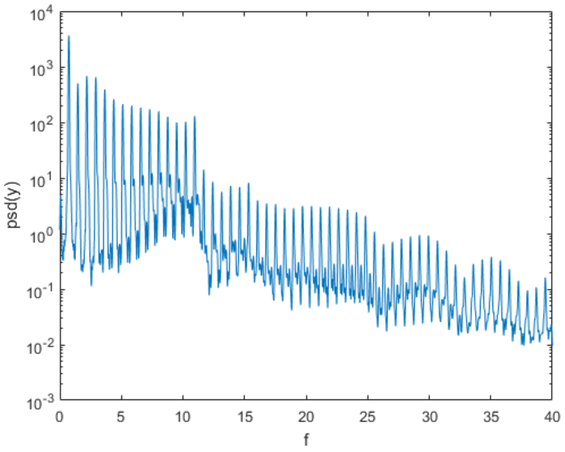

(c) Run 3

Figure 3.13: Sum of power spectral densities of strain gage data.

Run 1: irregular sea conditions with slamming

The first run is featured by an irregular sea condition, which has been performed by considering *JONSWAP* spectrum. The strain gages response is shown in Fig. 3.12b. The observer is then computed according to the method proposed in Sec. 3.2 and its quality is assessed by means of the quantities introduce in Sec. 2.4 (*i.e.*, TRAC and FRAC). TRAC and FRAC for this run are shown in Fig. 3.14. Because of all sensors are used for state updating, naturally we reach high values of TRAC and FRAC. The estimations of hydrodynamic loads on the right beam are shown in Fig. 3.15 by means of the PSDs of the vertical forces on the legs. The PSDs clearly show some peaks in correspondence of the wet natural frequencies. It could be due to modeling errors or other hydrodynamic behavior difficult to spotlight, such as the effects of added hydrodynamic mass and damping. The time response of the estimated vertical load acting on the second segment of the right hull is shown in Fig. 3.16 as compared with the vertical displacement of the same segment. It is worth to notice the sharp shape of the cyclic loads, likely owing to the shape of the hull that does not produce linear response according to the submersion. Moreover, in correspondence of slamming time instant (about 57 s and 60 s) the estimation presents a behavior at higher frequency. As before, modeling errors or other hydrodynamic phenomena could influence the estimation.

Further results concern the time-frequency domain response of the deflection field projected on the vibration modes. In Fig. 3.17 the response the principal vibration modes are shown by means of continuous wavelet transform. In that figures it is superimposed also the vertical displacement of the fore wetdeck center point relative the wave height. It is worth noticing the occurrence of slamming phenomena in correspondence of the negative peaks that exceed a certain threshold. In particular, Fig. 3.17a shows the response of the split mode. It can be noticed that the main frequency is contained in a range between 7 and 9 Hz, that is about the value came out from the vibration tests carried out with the wet configuration (see Fig. 3.5). It can be pointed out that the frequency trend swings following the trend of the relative displacement of the deck. Indeed, the split mode mainly involves the bow region and this particular behavior is owing to dynamic variation of hydrodynamic mass distribution caused by heave and pitch motion.

The vertical two-node bending mode, instead, presents evident wide-band instant responses due to the impacts in the wetdeck region. After the slamming, the wavelet spectrum shows an halo at about 12 Hz that is the trace left by the associated modal

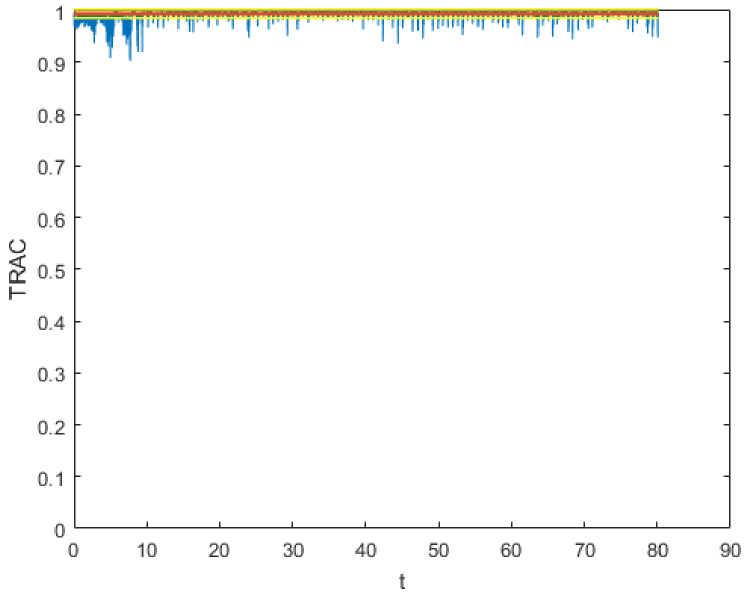

(a) Time response assurance criterion

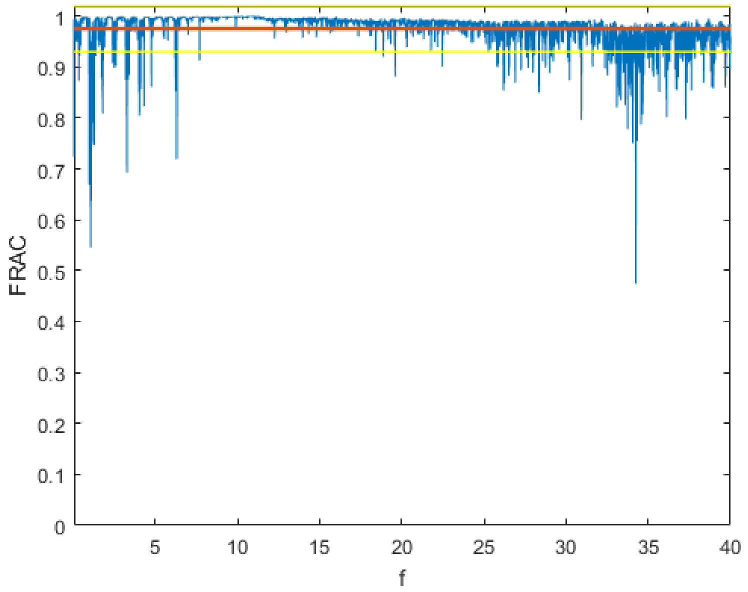

(b) Frequency response assurance criterion

Figure 3.14: Time and frequency response assurance criterion of strain outputs.

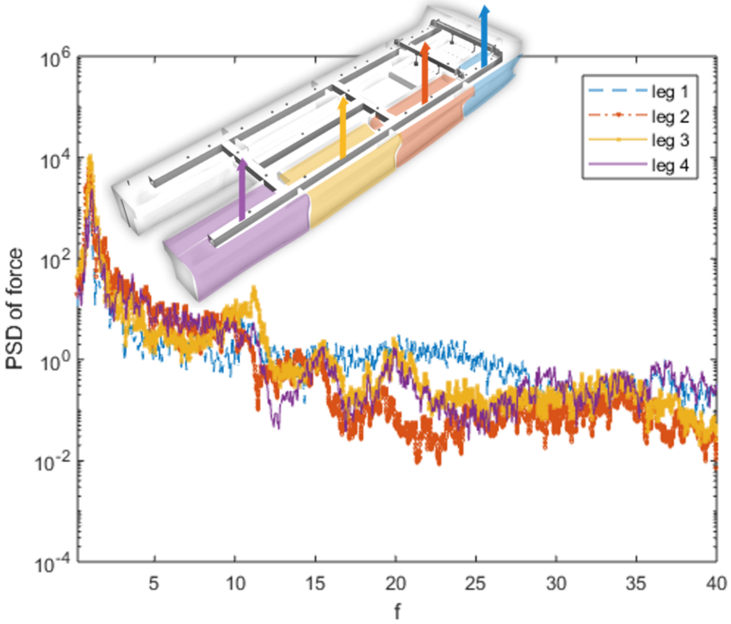

Figure 3.15: Run 1. Power spectral densities of the estimated concentrated forces on right beam legs. The legend is sorted starting from the bow to the stern.

response. It is worth noting that these two effects add up to the response of the wave load at very low frequencies.

An interesting result also concerns the sixth vibration mode. The trend of its natural frequency is highly dependent on the attitude of the structure with respect to the free surface. Indeed, the sixth mode (see in Fig.3.11) is featured by symmetrical torsion of the long beams at the bow, thus reflecting on an impressive increase of added modal mass when the fore region is submerged.

Run 2: regular sea conditions without slamming

The second run relates the response to long regular waves. It leads to a limited seakeeping response, which does not trigger impact phenomena in the wetdeck region. The heave and pitch frequency response can be appreciate in Fig. 3.12a. This sea condition leads to a moderate elastic response as shown in Fig. 3.13a. Note that the most of response is owing to wave loads. The observation process seems effective over time (see TRAC in Fig. 3.18a). However, the FRAC function shows lower value compared to the case in irregular sea, except for that frequency lines where the excitation is higher(see Fig. 3.18b). For this run, the most valuable result is the

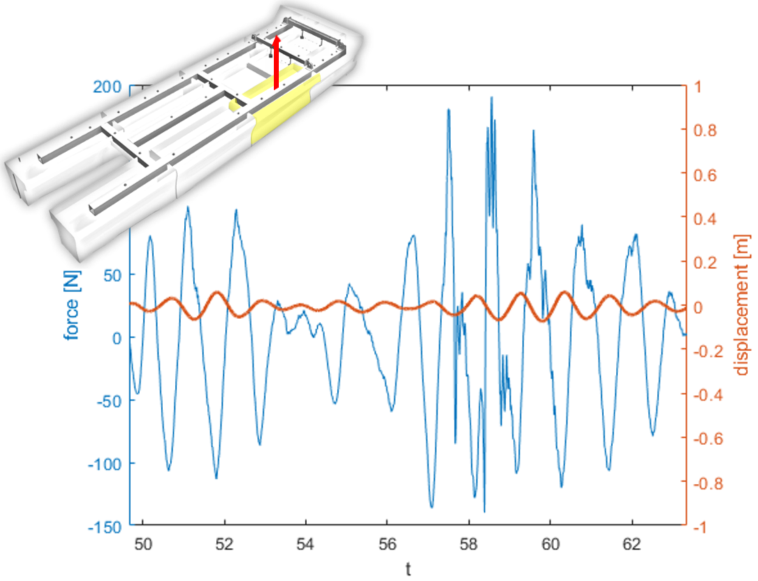

Figure 3.16: Run 1. Time response of the force on the second segment pointed out in the sketch above.

estimation of the loads exchanged at the interfaces with the hulls. In Fig. 3.19 the PSDs of the estimated concentrated forces on the right beam legs are shown where the main structural response is at the frequencies of the rigid-body modes.

Run 3: regular sea conditions with intense slamming

The third run is concerned with the catamaran response to short and high regular waves that lead the structure to experience slamming phenomena in the fore wetdeck region. In this case the rigid-body response shows sharp super-harmonic peaks exalted by the recurring impacts (see Fig. 3.12a). The resulting elastic response is clearly conditioned from these impacts such that the spectrum is highly conditioned by the presence of the spikes. The observer quality is assessed by means of the quantities introduce in Sec. 2.4. TRAC and FRAC are shown in Fig. 3.20. One of the most interesting results concerning this run is the extrapolation of the estimated forces in the wetdeck region, whose time response estimation is shown in Fig. 3.21. Although the sea conditions are completely different, the structural response is similar to that of run 1. Indeed, Fig. 3.22 underlines that also in this case the first two vibration modes present a behavior simile to the ones already shown for the irregular sea condition case, emphasizing the effectiveness of the observer also in assessing the

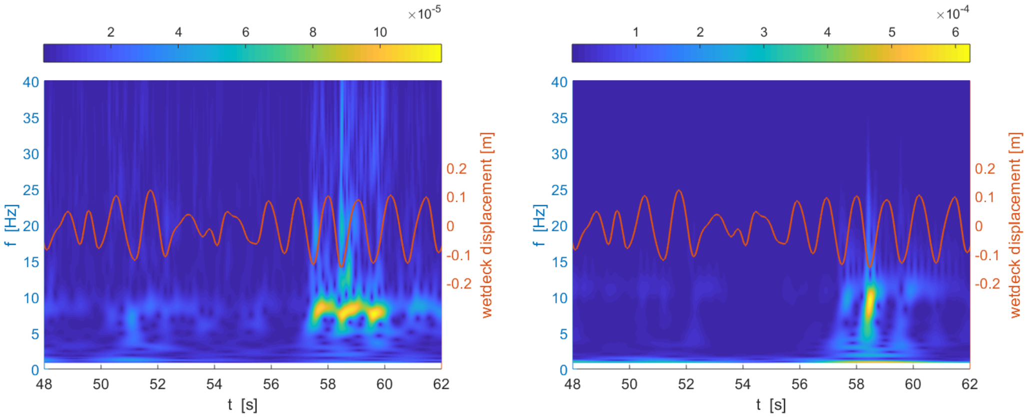

(a) First mode

(b) Second mode

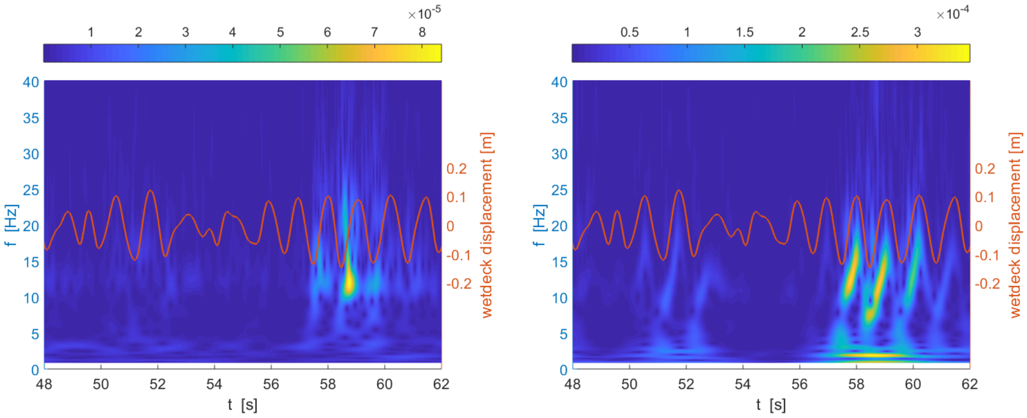

(c) Fifth mode

(d) Sixth mode

Figure 3.17: Run 1. Vibration modes wavelet spectrum. The red line represent the time domain response of vertical displacement of wetdeck center point relative to the wave height.

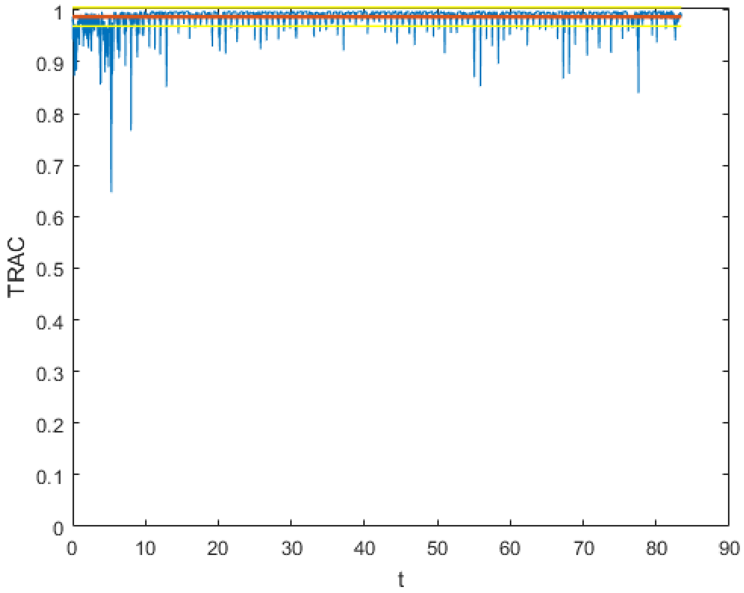

(a) Time response assurance criterion

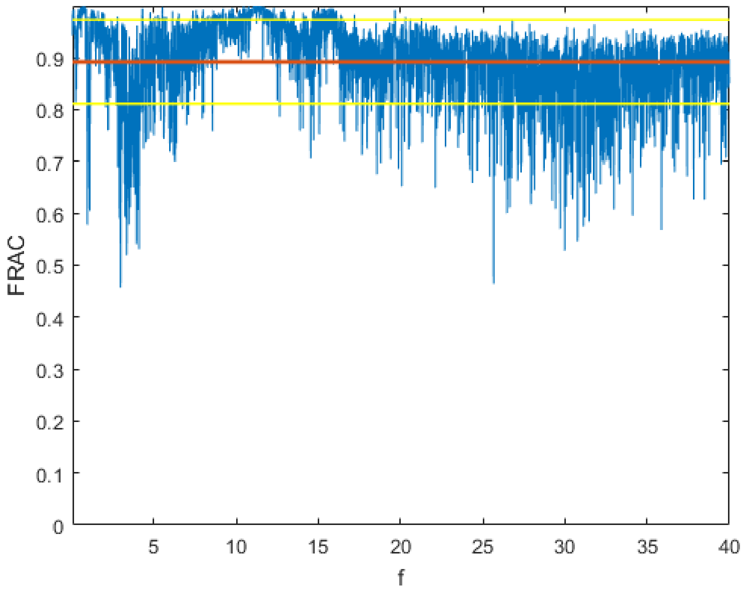

(b) Frequency response assurance criterion

Figure 3.18: Run 2. Time and frequency response assurance criterion of strain outputs.

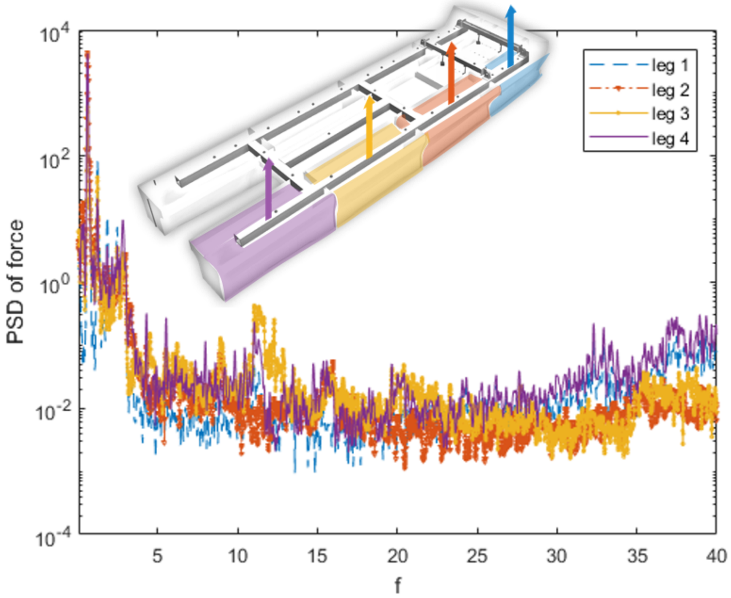

Figure 3.19: Run 2.Power spectral densities of the estimated concentrated forces on right beam legs. The legend is sorted starting from the bow to the stern.

response in different sea conditions.

3.3.2 Convergence analysis

According with the measurement set classification in Sec. 2.1.3, a sensitivity analysis on the spatial density of strain gages is carried out. In order to simplify the description of the current analysis, the available measurements are divided into 4 groups by considering the strain gages layout in Fig. 3.6:

g_1 : 1-36

g_2 : 1,3,5,7,9,12

g_3 : 16,18,22

g_4 : 14,25-29,30,32,34

The sensitivity analysis is then carried out by considering six cases obtained by combination of the four groups above (in accordance with the classification in Sec. 2.1.3) as reported in Tab. 3.3.

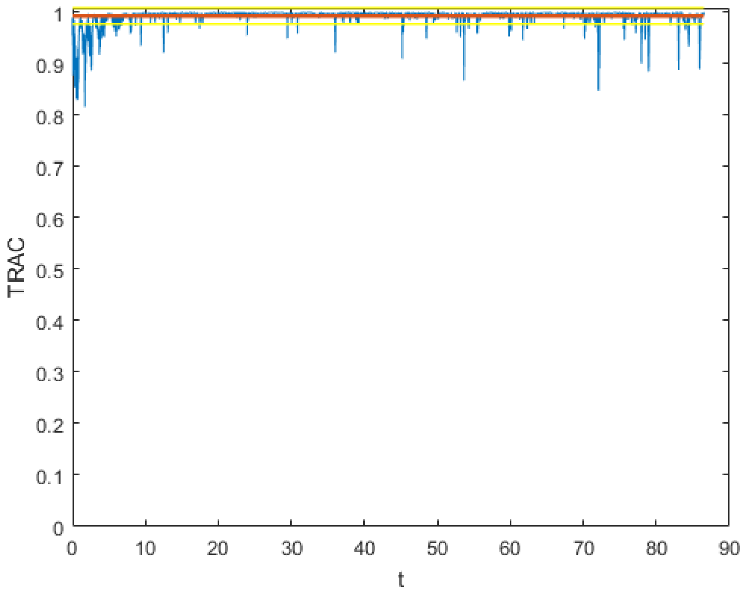

(a) Time response assurance criterion

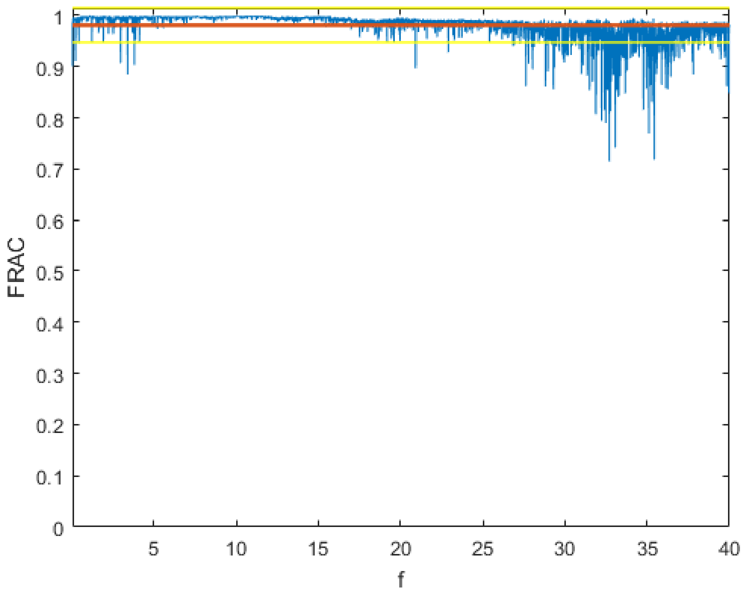

(b) Frequency response assurance criterion

Figure 3.20: Run 3. Time and frequency response assurance criterion of strain outputs.

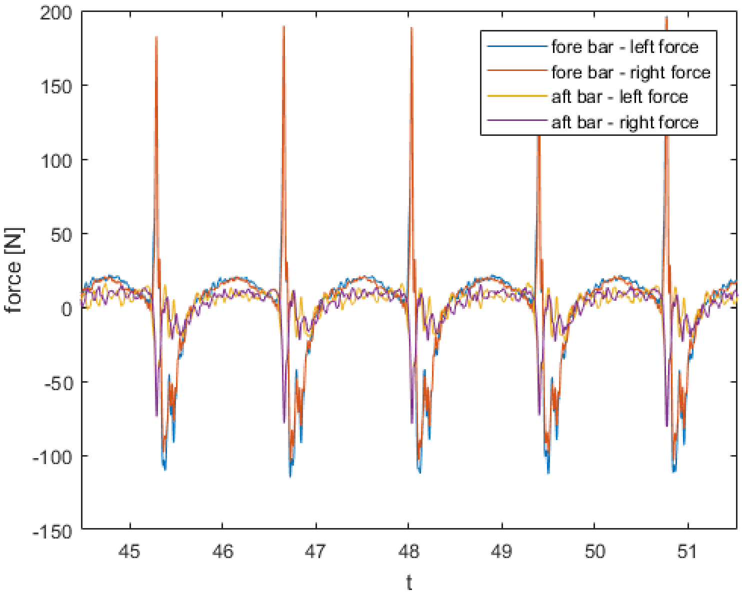

Figure 3.21: Run 3. Time histories of concentrated forces on wetdeck region.

subset	case 1	case 2	case 3	case 4	case 5	case 6
Active	g_1	$g_1 - g_2$	$g_1 - (g_2 \cup g_3)$	$g_1 - (g_2 \cup g_3 \cup g_4)$	$g_1 - (g_2 \cup g_3)$	$g_1 - (g_2 \cup g_3 \cup g_4)$
Stored	g_1	g_1	g_1	g_1	$g_1 - g_2$	$g_1 - (g_2 \cup g_3)$
Control	g_1	g_1	g_1	g_1	g_1	g_1

Table 3.3: Set classification.

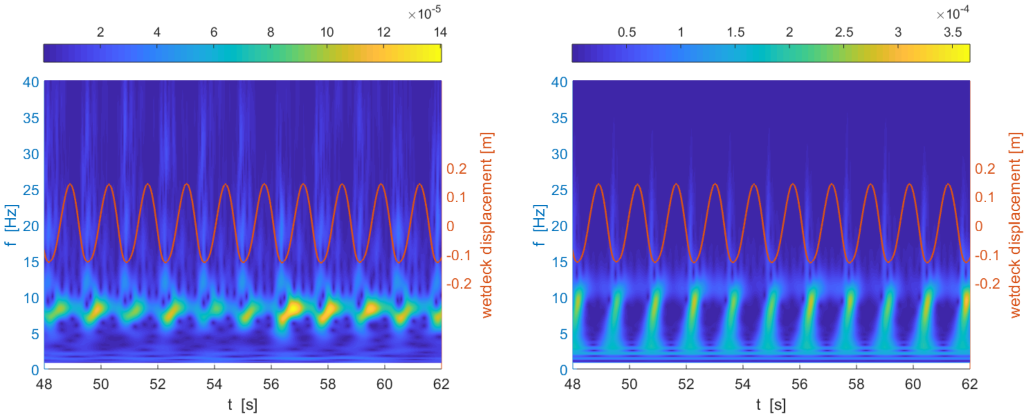

(a) First mode (b) Second mode

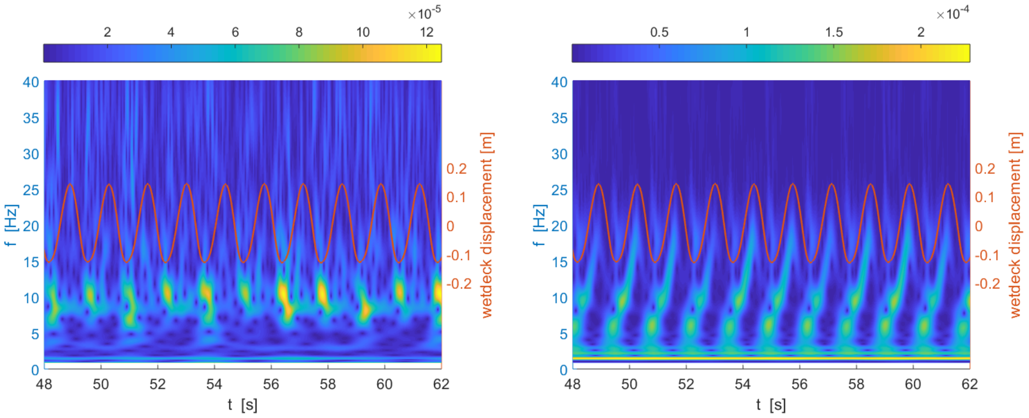

(c) Fifth mode (d) Sixth mode

Figure 3.22: Run 3. Vibration modes wavelet spectrum. The red line represent the time domain response of vertical displacement of wetdeck center point relative to the wave height.

Case	$\overline{TRAC}^{(1)}_{\mathsf{y_c\hat{y}_c}}$	$\overline{FRAC}^{(1)}_{\mathsf{y_c\hat{y}_c}}$	$\overline{TRAC}^{(2)}_{\mathsf{y_c\hat{y}_c}}$	$\overline{FRAC}^{(2)}_{\mathsf{y_c\hat{y}_c}}$	$\overline{TRAC}^{(3)}_{\mathsf{y_c\hat{y}_c}}$	$\overline{FRAC}^{(3)}_{\mathsf{y_c\hat{y}_c}}$
1	0.9922	0.9808	0.9873	0.8914	0.9932	0.9747
2	0.9875	0.9663	0.9776	0.7701	0.9874	0.9514
3	0.9587	0.9174	0.9310	0.7345	0.8531	0.8664
4	0.8635	0.8368	0.8710	0.6779	0.8505	0.8667
5	0.7135	0.7278	0.9241	0.7154	0.7526	0.8004
6	0.7137	0.7097	0.5952	0.5174	0.6713	0.7260

Table 3.4: Values of average FRAC for each run and each sea condition.

For each run and for each set of sensors, the values of $\overline{TRAC}_{\mathsf{y_c\hat{y}_c}}$ and $\overline{FRAC}_{\mathsf{y_c\hat{y}_c}}$ have been computed and reported in Tab. 3.4. The rows are related to the current classification of sensors while the columns refer the values of $\overline{TRAC}^{(i)}_{\mathsf{y_c\hat{y}_c}}$ and $\overline{FRAC}^{(i)}_{\mathsf{y_c\hat{y}_c}}$ for *i-th* run. Tab. 3.4 indicates that the higher the number of sensors used the better is the estimation. However, it shows that also reducing drastically the number of sensor (as in case 4 and 6) the average values of FRAC and TRAC still remain acceptable. However, case 4 presents a better estimation than case 6 despite it has the same number of active sensors. It demonstrates that the employment of sensors that are used only to guide the synthesis of the observer (such as $\mathsf{y_s}$) may improve the observation process.

Chapter 4

Application to a flexible aircraft

In this chapter we will investigate the problem of reconstruction of the elastic displacements of the structure by means of a purely numerical case concerning the aeronautical sector. In Sec. 4.1, the reference numerical model will be described while in Sec. 4.2 the generation of data will be discussed along with the results concerning the specific case study.

4.1 Numerical model description

The suitability of the observation methodology in Sec. 2.3.3 applied to flexible vehicles is assessed by means of the body-freedom flutter reference flying wing described in Refs. [40, 41] and shown in Fig. 4.1. This configuration shows relevant coupling effects due to the interaction between the short-period mode and the first aeroelastic mode, which eventually leads to body freedom flutter.

The case study concerns a truly existing model used to study this particular type of instability that, with the technological development that leads to the production of increasingly light-weight and more flexible airplanes, represents a constraint on the design of modern aircraft. The problem of the development of elastic deflections observer of this model has already been debated in [3] where a virtual sensing with modal filter has been realized as a necessary step for the designed control.

The model has been tuned to match the modal scenario described in [41] using the MSC Nastran gradient-based optimization solver [32]. The first six elastic mode shapes of the unrestrained structure are illustrated in Fig. 4.2. In Tab. 4.1 the main characteristics of the aircraft are listed.

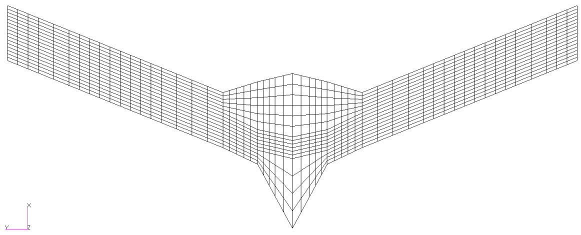

(a) Upper view

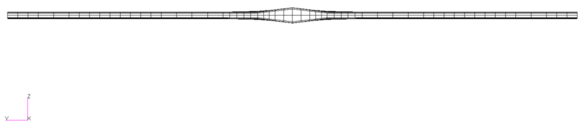

(b) Front view

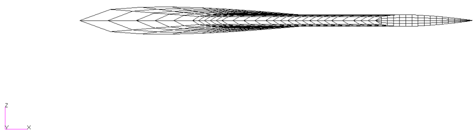

(c) Side view

Figure 4.1: FEM model of the flying-wing vehicle [42].

Variable	value
Mass	5.4571 Kg
span	3.04 m
$\bar{c}$	0.4 m
J_{11}	1.1427 Kg m^2
J_{22}	0.2324 Kg m^2
J_{33}	1.3707 Kg m^2

Table 4.1: Main aircraft parameters.

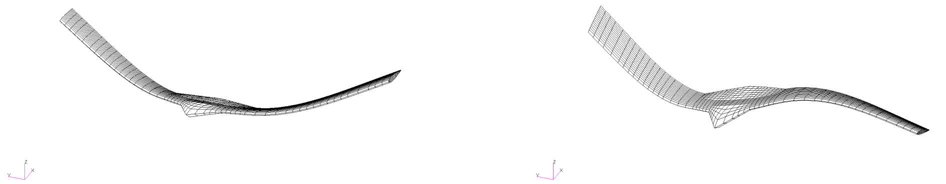

(a) $f_1 = 5.830$ Hz , $m_1 = 0.129$ kg m^2 (b) $f_2 = 8.831$ Hz, $m_2 = 0.145$ kg m^2

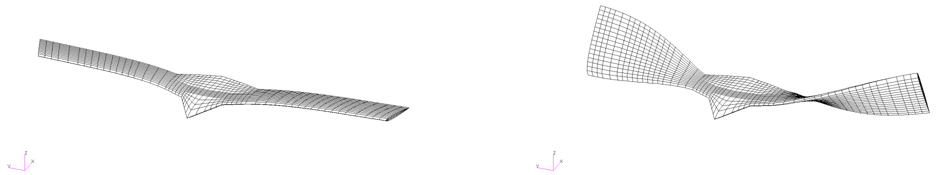

(c) $f_3 = 13.452$ Hz , $m_3 = 0.222$ kg m^2 (d) $f_4 = 19.817$ Hz , $m_4 = 0.004$ kg m^2

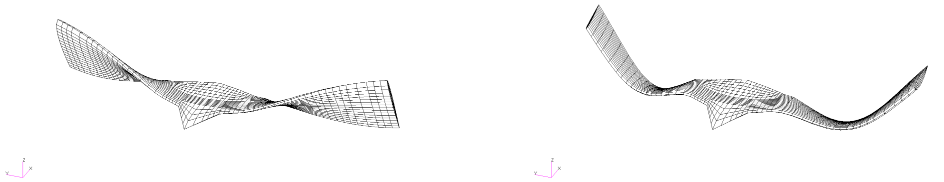

(e) $f_5 = 20.093$ Hz , $m_5 = 0.003$ kg m^2 (f) $f_6 = 23.727$ Hz , $m_6 = 0.002$ kg m^2

Figure 4.2: Elastic mode shapes of the flying-wing FEM model [42].

Stability analysis of the reference case study

The stability analysis of the present case study has been carried out by means of the approach presented in [42] and synthetically reported in Appendix D. The approach exploits an integrated modeling of aeroelasticity and flight dynamics that allows to get a full picture of the linearized dynamic behavior of a flying aircraft around any steady maneuver, providing a state space representation in terms of small perturbations. The state is expressed as follows:

$$\mathsf{x} = \begin{Bmatrix} \Delta \mathsf{x}_{\mathsf{G}} \\ \Delta \Theta \\ \Delta \mathsf{q} \\ \Delta \mathsf{v}_{\mathsf{G}} \\ \Delta \omega \\ \Delta \dot{\mathsf{q}} \\ \Delta \mathsf{a} \end{Bmatrix} \tag{4.1}$$

where x_{G} and $\Delta\Theta$ are, respectively, the perturbations of position of instantaneous center of mass and aircraft attitude, $\Delta\mathsf{v}_{\mathsf{G}}$ and $\Delta\omega$ are the perturbations of center of mass speed and angular velocity with respect to he body axes, $\Delta\mathsf{q}$ and $\Delta\dot{\mathsf{q}}$ are, respectively, the vector of generalized coordinates and velocities, whilst $\Delta\mathsf{a}$ is a vector of added aerodynamic states necessary to describe the unsteady aerodynamics. The state matrix is thus expressed as a function of speed U_∞, Mach number M_∞, altitude (density), and if non null, the steady angular velocity.

The stability analysis of the aircraft in steady rectilinear flight is carried out for $U_\infty = 15 \rightarrow 30$ m/s, $M_\infty = 0$ and sea level conditions. The root locus is shown in Fig. 4.3 along with the zoom on the poles associated to the critical modes. In figure, the circles represent the poles at the first parameter value of the root locus (*i.e.* at $U_\infty = 15$) with the name of the modes from which the poles originate, whereas the stars represent the poles at the flutter speed.

It can be deduced that the instability mainly arises due to the coupling between the first structural mode and the short period mode. The combined dynamics leads to flutter at $U_F^o = 20.91$ m/s. This speed value represents an upper limit for the analyses we are going to discuss showing the observer's efficiency even in cases where the dynamics presents coupled modes.

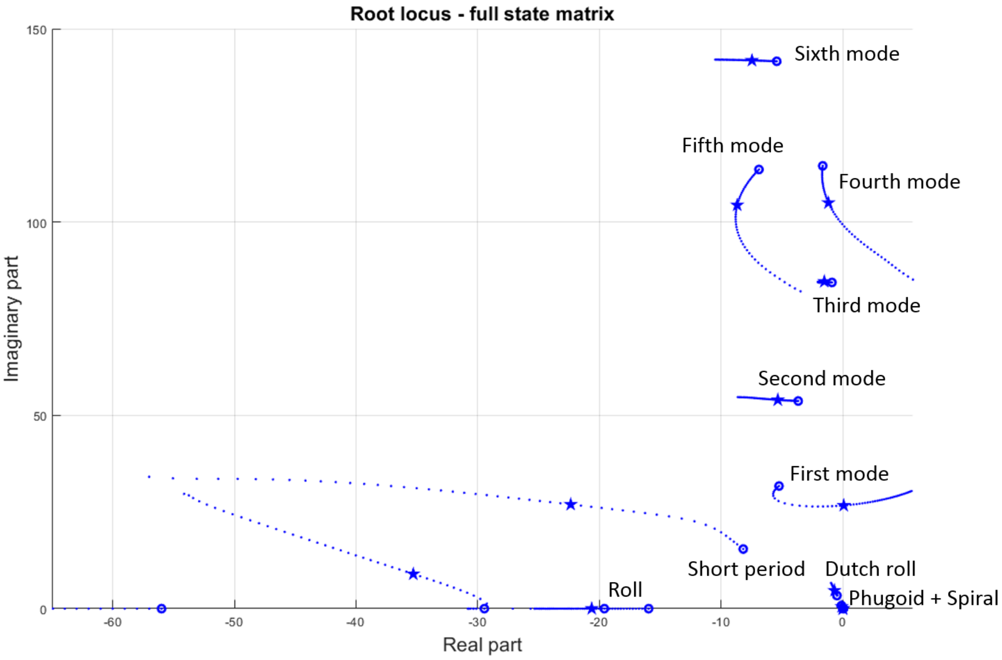

(a)

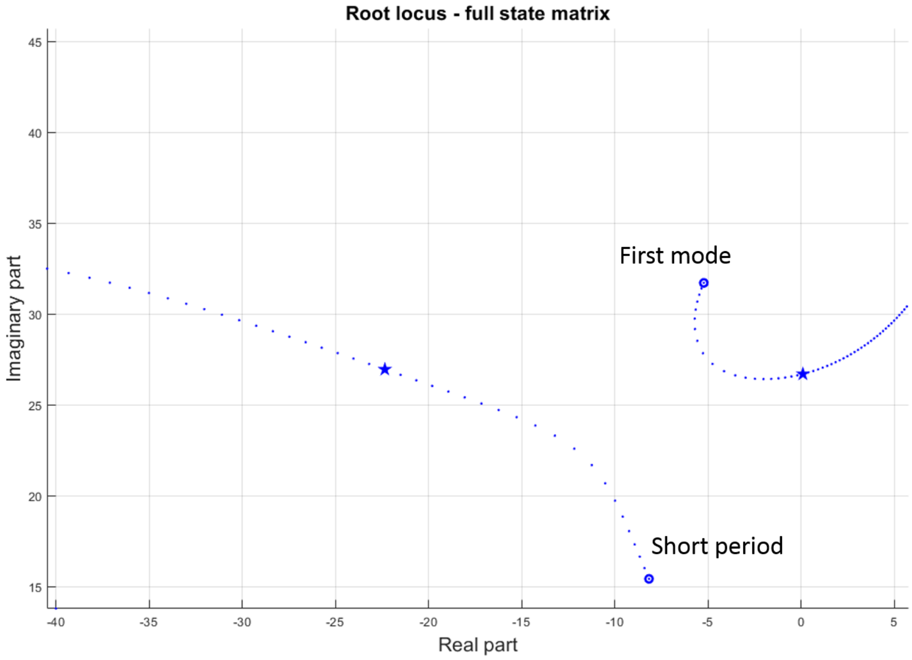

(b) Short-period and first aeroelastic mode

Figure 4.3: Root locus in steady rectilinear flight ($U_\infty = 15 \rightarrow 30$ m/s).

4.2 Virtual experiment of the aircraft

The strategy with which the response to the gusts are generated is important for having consistent data with the physics we want to observe. In this section the characteristics of the runs that we will examine and the various virtual measurements layouts are illustrated. Also, the response analyses have been performed through the approach presented in [42] and reported in Appendix D.

4.2.1 Virtual tests generation

In this case we want to excite the structure with loads that behaves similarly to that presented in Chap. 3 regarding the naval application. We have seen that for seakeeping trials in towing tank both regular and irregular sea condition were considered. The regular sea condition represented a deterministic excitation on the structure. On the other hand, irregular sea conditions excited the structure in a stochastic manner. On the other hand, aeronautical structures are concerned by gust conditions that can deterministic (usually of type 1-cosine) or stochastic. Also in this case, the gusts will be featured by characteristic wavelength and amplitude combined with the speed of the structure.

From one side, type *1-cosine* gusts are defined by the following time law

$$\mathsf{w}_g(t) = \begin{cases} \mathsf{w}_g^{max}\,\frac{1}{2}\Big[1-\cos(2\pi\frac{U_\infty}{L}t)\Big]\ , & 0<t<1/f_g \\ 0\ , & t \geq 1/f_g \end{cases}$$

where w_g^{max} is the vector collecting the maximum value of each speed component, and L is the length of the gust (see Fig. 4.4a).

On the other side, the stochastic gusts are featured by *Von Karman* spectra. Referring to the gust model in Appendix D (see Eq. (D.31)), each component of the gust is considered independent by each others. In such a way, the *i-th* component of the spectral density is expressed by

$$\Phi_{w_{g_i}}(\omega) = \sigma^2_{w_{g_i}}\frac{2L}{U_\infty}\frac{\Big[1+\frac{8}{3}\big(1.339\frac{2\pi L}{U_\infty}f\big)^2\Big]}{\Big[1+\big(1.339\frac{2\pi L}{U_\infty}f\big)^2\Big]^{11/6}}$$

where $\sigma_{w_{g_i}}$ is the root mean square of the *i-th* component and L is the characteristic length of the gust. The gust spectra are generated similarly to what happens in towing-tank experiments performed on the catamaran where the *JONSWAP* spec-

Run	Speed [m/s]	$\sigma_{w_{g3}}$ or w_{g3}^{max}	$\sigma_{w_{g4}}$ or w_{g4}^{max}	$L/\bar{c}$	Type
1 (reference)	17.7	0.5	0.05	1.	turbulence
2	15.0	0.5	0.	12.5	turbulence
3	17.4	0.5	0.	3.125	1-cosine

Table 4.2: Reference gust conditions.

trum was used to generate waves with determined ocean statistical properties (see Fig. 4.4b) [1].

In this work, two stochastic gust conditions and one deterministic gust will be considered as reference case study (see Tab. 4.2), where each of the simulations is 10 seconds long with a sampling frequency of 500 Hz. The structural response is obtained by considering 40 vibration modes.

4.2.2 Sensor layouts

A rich set of measures is considered as experimental output of the virtual model. The accelerometer and strain gage sets are introduced in Fig. 4.5. The recorded accelerations are considered to be directed along *z-axis*, whereas the strains measured parallel to the elastic axes of the wing. The power spectral density of the strain gage noise is assigned equal to $1e-1(\mu\text{strain})^2\text{Hz}^{-1}$ for each value of frequency up to the sampling frequency. Concerning the accelerometers, the noise PSDs are not constant in frequency but present values ten time greater for $f < 1$ Hz as in Fig. 4.6. This is done in order to consider the internal sensor dynamics of the commercial piezoelectric accelerometers. Specially we will perform the analyses by considering eleven different sensor layouts in accordance with the sensor positions shown in Fig. 4.5. Note that for this case study we mean only *active sensors* . Indeed, the assessment of the observation performance is carried out directly by means of comparison between estimated and simulated generalized coordinates response. The measurement datasets are thus listed below [2]:

ds_1 : strain gages 1-16 , accelerometers 1 6 7 12 13 [tot: 16+5] (reference)

ds_2 : strain gages 1 2 5 6 9 10 13 14, accelerometers 1 4-7 10-13 [tot: 8+9]

---

[1] Remind that the generated signal is only one sample of the several samples possible of gust obtainable with the same spectrum.

[2] **NB** As mentioned in *Assumption 1* in Sec. 2.2.3, the accelerations provided by the accelerometers are previously integrated to have displacement data (and consequently also the spectral densities are multiplied by a factor ω^{-2}).

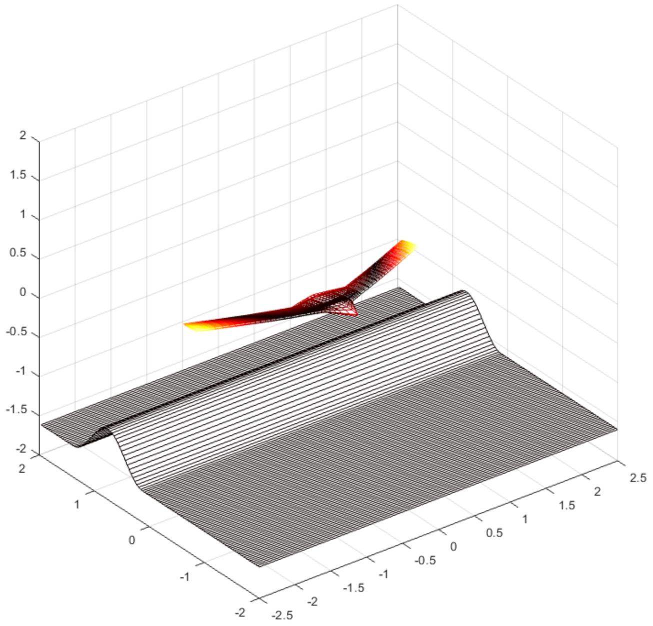

(a) 1-cosine gust

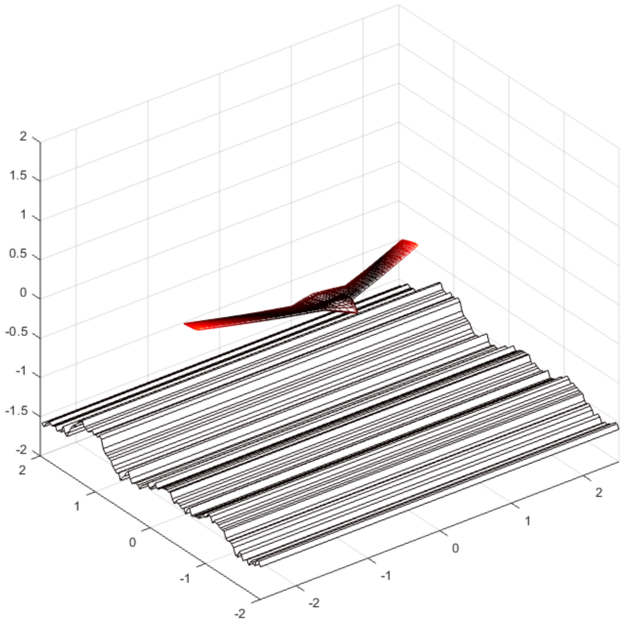

(b) Turbulence gust

Figure 4.4: Example of gust loads: the carpet below the aircraft represents the gust vertical velocity.

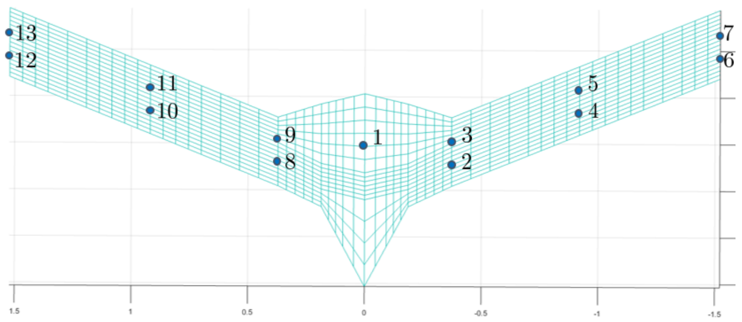

(a) Accelerometers

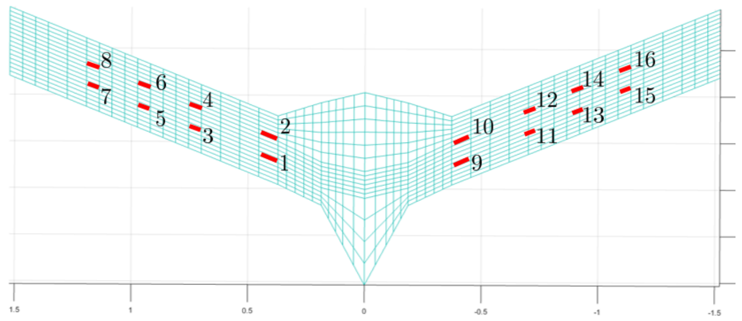

(b) Strain gages

Figure 4.5: Accelerometer and strain gage positions.

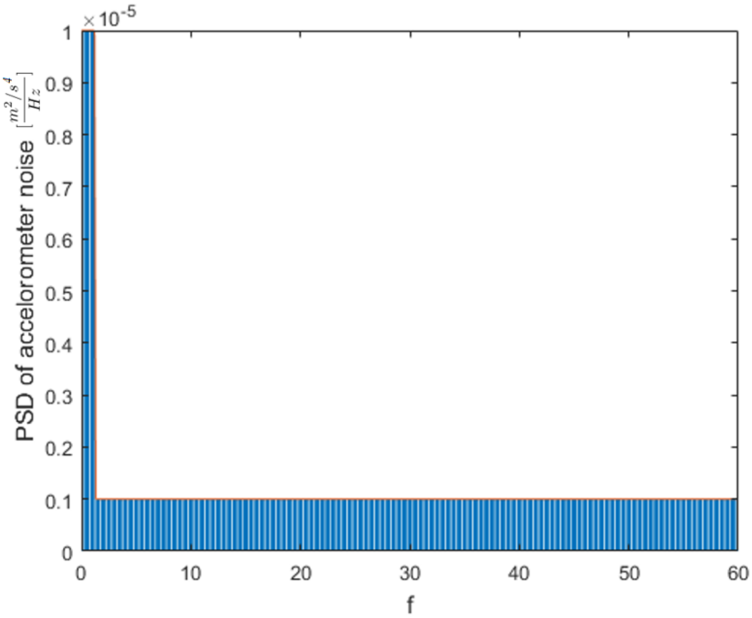

Figure 4.6: Power spectral density associated to accelerometer noise.

ds_3 : accelerometers 1-13 [tot: 0+13]

ds_4 : strain gages 1-16 [tot: 16+0]

ds_5 : strain gages 1-6 8-14 16 [tot: 14+0]

ds_6 : strain gages 1-5 8-13 16 [tot: 12+0]

ds_7 : strain gages 1 2 4 5 8-10 12 13 16 [tot: 10+0]

ds_8 : strain gages 1 4 5 8 9 12 13 16 [tot: 8+0]

ds_9 : strain gages 1 3-9 11-16 [tot: 14+0]

ds_{10} : strain gages 1 4-9 12-16 [tot: 12+0]

ds_{11} : strain gages 1 4 5 7 8 9 12 13 15 16 [tot: 10+0]

4.3 Illustrative results

In this section the results concerning the observation of the flexible aircraft response to different gust conditions will be investigated. The section is previously introduced by a paragraph where the hypothesis concerning the current observation problem are enunciated.

mode	$f_n[Hz]$	m_n[kg m^2]
7	24.222	0.123
8	27.189	0.023
9	55.145	0.007
10	57.304	0.006
11	57.949	0.027
12	60.754	0.003
13	60.836	0.003
14	65.185	0.026
15	92.669	0.003

Table 4.3: Natural frequencies and modal masses of modes from *7-th* to *15-th*.

4.3.1 Customization of the state observer for the present case study

The analysis of the flexible aircraft is different with respect to the experimental-one proposed in Chap. 3, since the flight data are simulated by means of an appropriate numerical framework (see [42]). The FE model of the observer coincides with that used for the simulation. This represents a mere simplification to the problem, albeit not strictly necessary. As a consequence, the modal base used for the observation is a subset of that used for the simulations. This simplifies the reading of the results in which it will be possible to directly link the *real* modal coordinates that are the output of the simulations with those provided by the estimation process [3]. However, numerical errors are included through the employment of *i)* a different damping model (between the simulation model and the one used to enhance the synthesis of the state observer) and *ii)* different flight and gust conditions. The measurement noise properties used to synthesize the observer are the same used to generate noisy data.

The *target* of the analysis is to estimate the response of the aircraft in terms of three rigid body modes (heave, pitch and roll) and 14 vibration modes. The number of modes have been chosen since the model presents an appropriate gap between the *14-th* and the *15-th* natural frequencies. Tab. 4.3 indeed lists the natural frequencies of the vibration modes missing from Fig. 4.2.

The objective of the present case study is the validation of the *multi-scale observer* described in Sec. 2.3.3. This procedure consists in subdividing the signal

---

[3] Even using a different model, it is very easy to project the displacements of the simulated modal response on the modal basis used in observation by knowing the mass matrix of the model used for the simulation and the modal mass matrix used by the observer plant.

into a certain number of sub-signals making the various observers $\mathsf{L}^{(j)}$ designed to be optimal for each specific frequency content. Here, 2 cases of multi-resolution to be compared were considered: *i)* a first (the reference one) in which the observer relies on 7-level decomposition and *ii)* another on 2-level decomposition. Once the sampling frequency is assigned, the frequency content of each wavelet level is easily obtained. In Fig. 4.7a the equivalent transfer functions of the approximation and details are shown for the present case. The first two level of detail (dot lines at higher frequencies) will not be considered for the present analysis. Indeed, the measurement noise for these scales is very high due to the response of the residual modes not included within the dynamics to be estimated [4]. The 2-level decomposition (see Fig. 4.7b) is considered for the comparison since its approximation signal includes all the details and the approximation levels considered in the 7-level decomposition.

$$\mathsf{y}^{(a_3)} = \mathsf{y}^{(a_7)} + \mathsf{y}^{(d_7)} + \mathsf{y}^{(d_6)} + \mathsf{y}^{(d_5)} + \mathsf{y}^{(d_4)} + \mathsf{y}^{(d_3)}$$

Note that this last case coincide with the case in which the observer is synthesized simply considering the whole output $\mathsf{y}(t)$ with a low-pass filter.

In the following analyses the simulated modal response (*true data*) will be compared with *i)* the estimated response obtained by means of 7-level multi-resolution decomposition and, *ii)* the estimated response obtained by synthesize the observer for the 2-level decomposition when it results useful for the evaluation of the effectiveness of the multi scale observer. In order to understand the results, let us remind that:

$$\begin{array}{rcccl}
\hat{\mathsf{q}} & = & \hat{\mathsf{q}}^{(a_7)} + \sum_{j=3}^{7} \hat{\mathsf{q}}^{(d_j)} & \equiv & \sum_{j=3}^{8} \hat{\mathsf{q}}^{(j)} \\
\hat{\mathsf{q}}^{(d_j)} & \neq & \hat{\mathsf{q}}^{(j)} & = & \mathsf{H}_O^{(j)}(t) * \mathsf{y}^{(d_j)} \qquad j \leq 7 \\
\hat{\mathsf{q}}^{(a_7)} & \neq & \hat{\mathsf{q}}^{(8)} & = & \mathsf{H}_O^{(8)}(t) * \mathsf{y}^{(a_7)}
\end{array}$$

If on the one hand $\hat{\mathsf{q}}^{(j)}$ are output directly from the estimation process, $\hat{\mathsf{q}}^{(d_j)}$ and $\hat{\mathsf{q}}^{(a_7)}$ can be estimated *a posteriori* from $\hat{\mathsf{q}}$. Moreover we will refer as $\hat{\mathsf{q}}_{cmp}$ (*i.e.* comparison results) the estimation obtained by means of 2-level decomposition observer. Also

---

[4] A detailed measurement noise modeling would lead to the synthesis of a very low gain for these levels of detail, thus producing an analogous result to neglect them as it is done in this case.

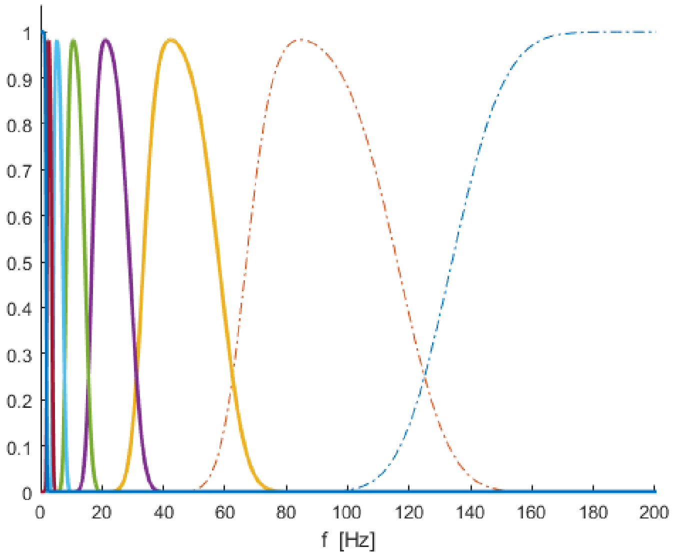

(a) 7-level decomposition

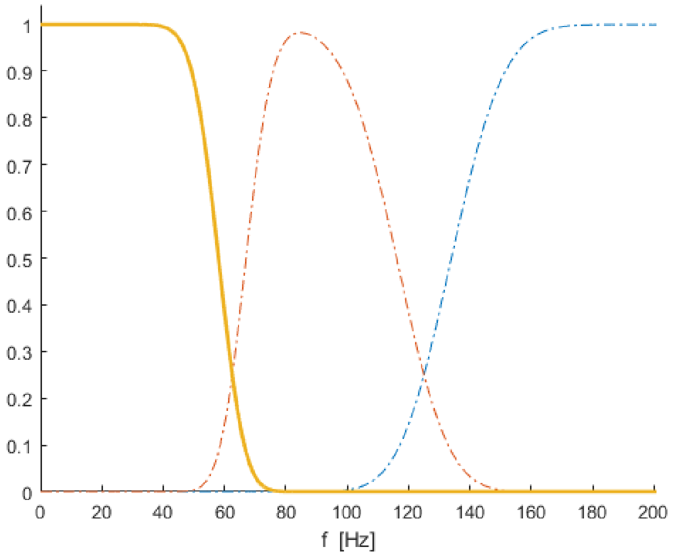

(b) 2-level decomposition

Figure 4.7: Absolute value of the equivalent frequency domain filtering transfer functions associated to the WMRA approximation and details used for the flexible aircraft case study.

$\hat{\mathsf{q}}_{cmp}$ can, in turn, be decomposed *a posteriori* in $\hat{\mathsf{q}}_{cmp}^{(d_j)}$ and $\hat{\mathsf{q}}_{cmp}^{(a_7)}$.

$$\hat{\mathsf{q}}_{cmp} \quad = \quad \hat{\mathsf{q}}_{cmp}^{(a_7)} + \sum_{j=1}^{7} \hat{\mathsf{q}}_{cmp}^{(d_j)} \quad \equiv \quad \hat{\mathsf{q}}_{cmp}^{(3)}$$

4.3.2 Run 1: response to high frequency turbulence

In this section the response of the aircraft to the condition expressed in the first row of Tab. 4.2 will be be investigated. The goal is to assess the performance of the proposed *multi-scale observer* and its dependency on sensor datasets.

Multi-level estimation

The first analysis is performed by considering only the first dataset ds_1. Fig. 4.8 shows the response of modes 1,4,5,6,9 and 18 that are the ones more excited by the load profile in Tab. 4.2. Here the blue lines represent the simulated modal response whilst the green lines represent the response obtained by means of an observer based on 7-level decomposition. The black lines represent the estimation provided by the observer based on 2-level decomposition. The observation based on 7-level decomposition shows a general improvement of the estimation process as it is possible to see a better correspondence between the green and the blue lines.

Fig. 4.8, instead, shows the power spectral densities related to the modal response and its estimation. Especially modes 4, 5 and 9 result to be significantly improved when an observation based on multi-resolution analysis is performed. This figure confirms qualitatively that the decomposition of the signal in several levels (as in Sec. 2.3.3) improves the estimate of elastic deflections.

In Fig. 4.10 the decomposition of the response of the *5-th* generalized coordinate is shown. It can be noticed that for any level of detail the estimation provided by the observer based 7-level decomposition is better than the one based on 2-level decomposition. This fact is easy to understand since every state observer $\mathsf{H}_O^{(j)}$ is optimized to estimate the state for the time scale of *j-th* level, even though the last level (*i.e.* the approximation) does not provide the expected response yet. It is worth to notice that the green and red lines are practically superimposed. This behavior validates (for this conditions) the hypothesis that has been made in Sec. 2.3.3 since the observer is sufficiently stiff to verify that $\hat{\mathsf{q}}^{(d_j)} \approx \hat{\mathsf{q}}^{(j)}$.

The improvements provided by *multi-scale observer* is quantified in Tab. 4.4. It is worth to notice that $\overline{TRAC}_{\mathsf{q}^{(d_j)}\hat{\mathsf{q}}^{(d_j)}}$ is better than $\overline{TRAC}_{\mathsf{q}^{(d_j)}\hat{\mathsf{q}}_{cmp}^{(d_j)}}$ for each level as discussed above.

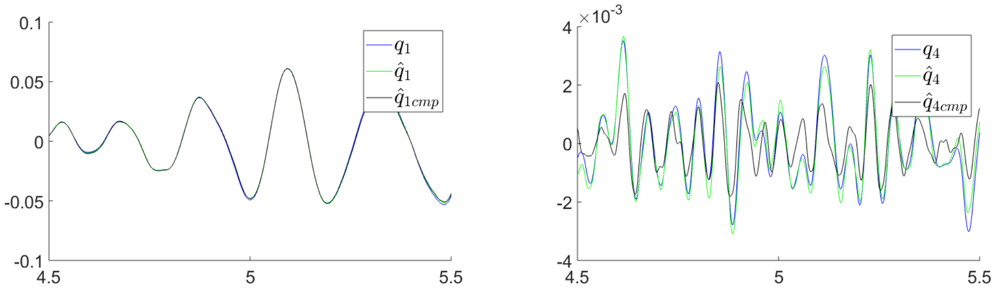

(a) mode 1 (b) mode 4

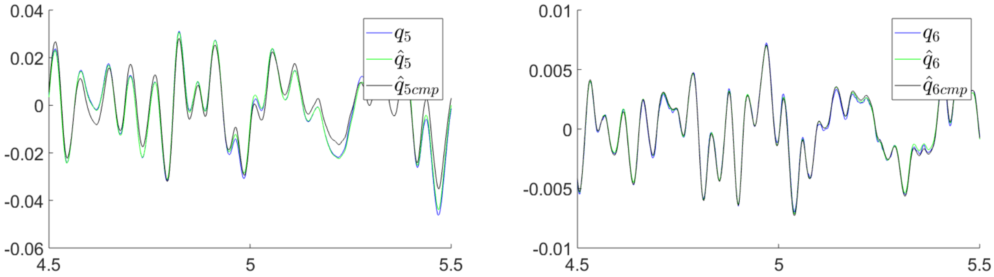

(c) mode 5 (d) mode 6

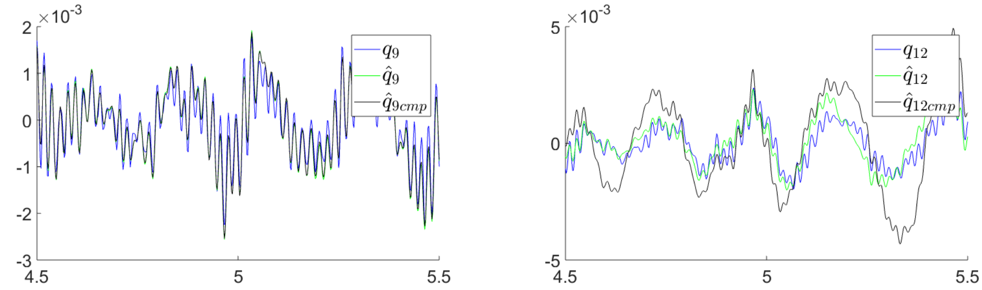

(e) mode 9 (f) mode 12

Figure 4.8: Run 1: simulated response of the more excited modal coordinates (blue) against their estimations by means of observers based on 7-level (green) and 3-level approximation (black).

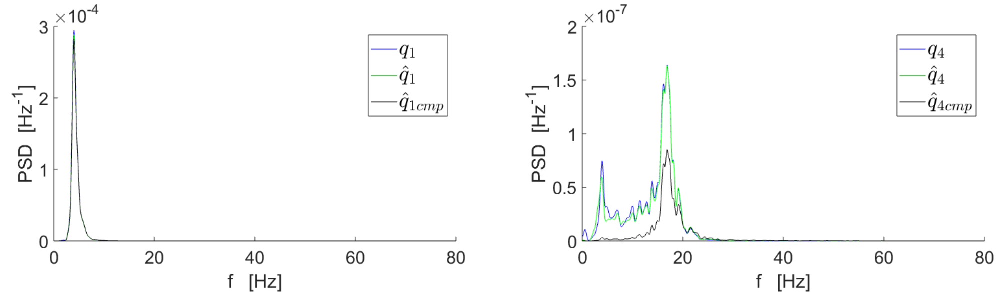

(a) mode 1 (b) mode 4

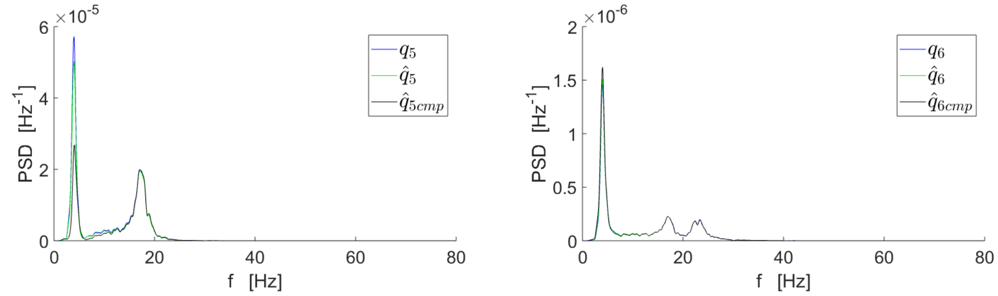

(c) mode 5 (d) mode 6

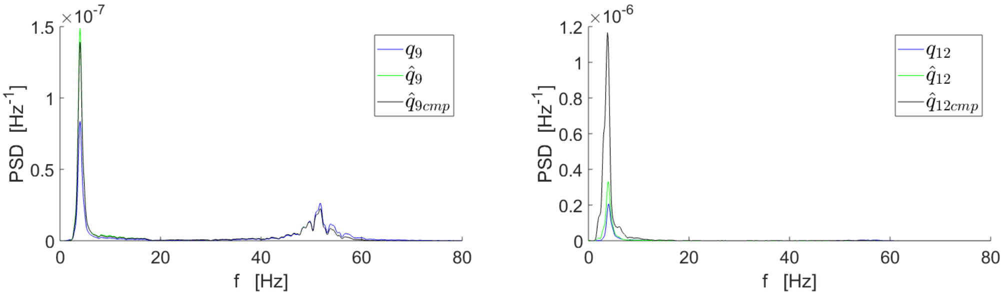

(e) mode 9 (f) mode 12

Figure 4.9: Run 1: PSD of simulated response of the more excited modal coordinates (blue) against their estimations by means of observers based on 7-level (green) and 3-level approximation (black).

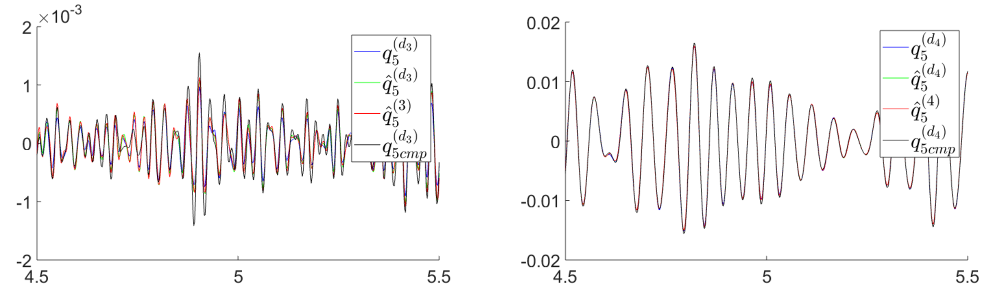

(a) detail 3 (b) detail 4

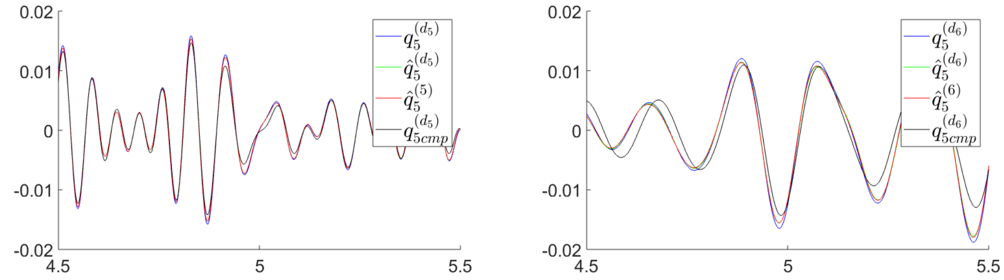

(c) detail 5 (d) detail 6

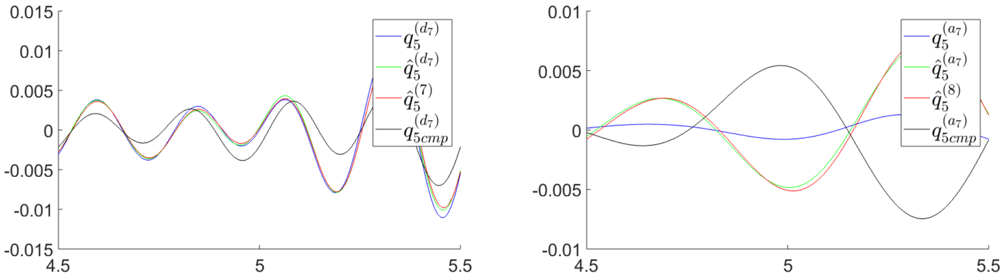

(e) detail 7 (f) approx. 7

Figure 4.10: Run 1: WMRA decomposition of simulated response of the *5-th* modal coordinate against its estimation at various levels of detail.

level	$\overline{TRAC}_{\mathsf{q}^{(d_j)}\hat{\mathsf{q}}^{(d_j)}}$	$\overline{TRAC}_{\mathsf{q}^{(d_j)}\hat{\mathsf{q}}^{(j)}}$	$\overline{TRAC}_{\mathsf{q}^{(d_j)}\hat{\mathsf{q}}_{cmp}^{(d_j)}}$
total	0.9862	0.9862	0.9713
d_3	0.8889	0.8907	0.8304
d_4	0.9969	0.9968	0.9870
d_5	0.9979	0.9978	0.9896
d_6	0.9981	0.9982	0.9920
d_7	0.9873	0.9881	0.9599
a_7	0.6983	0.6917	0.4681

Table 4.4: Mean values of TRAC for the between simulated response against estimation with 7-level decomposition (first and second column) and 2-level decomposition (third column) for each scale.

$ds_1 : \overline{TRAC}_{\mathsf{q}\hat{\mathsf{q}}}$	$ds_2 : \overline{TRAC}_{\mathsf{q}\hat{\mathsf{q}}}$	$ds_3 : \overline{TRAC}_{\mathsf{q}\hat{\mathsf{q}}}$
0.9862	0.9619	0.9241

Table 4.5: Mean values of TRAC for the 3 considered sensor layout.

Sensors layout dependency

The position of sensors (and consequently the number) is matter of another great problem that stands along the observation strategy, but that is not properly taken into account in this thesis. However, in this section a qualitative analysis on the spatial distribution and kind of sensors will be performed. First the dependency on the kind of data is considered. For this purpose only the first three sensor layouts in Sec. 4.2.2 are taken into account.

Fig. 4.11 shows the time response of the most exited modes for the three considered layouts. It can be noticed that the estimation is good for each set of measures, except for modes 9 and 12. In particular, the set ds_3 does not provide good estimates especially at low frequency. This behavior is due to *i)* the kind of data, since the set ds_3 is made up by only accelerometers (that are extremely noisy at low frequencies) and *ii)* by the number of sensors. Tab. 4.5 provides the values of TRAC for the 3 sensor layouts taken into account.

The second analysis concerns the number of sensors. In this case only strain measurements are considered. It means that rigid-body modes are not estimated together with the vibration modes. Moreover, in this analysis the target is to estimate only the first 8 vibration modes. In Fig. 4.12 the strain gage datasets are shown more explicitly (consider that the distribution is symmetric so that it is shown only

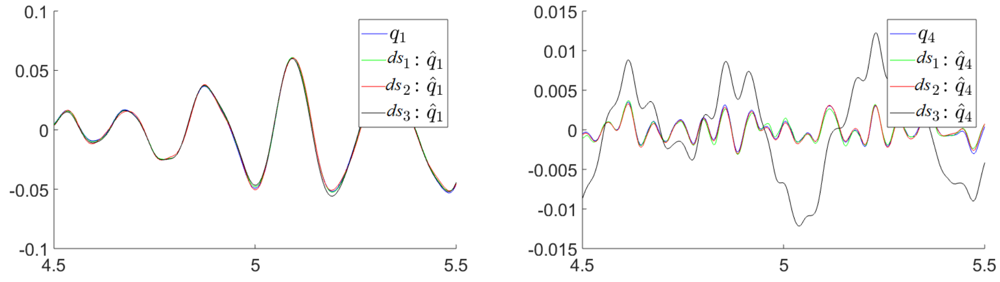

(a) mode 1 (b) mode 4

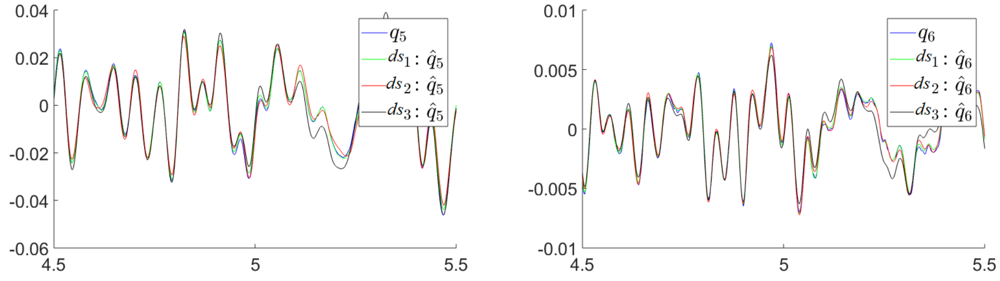

(c) mode 5 (d) mode 6

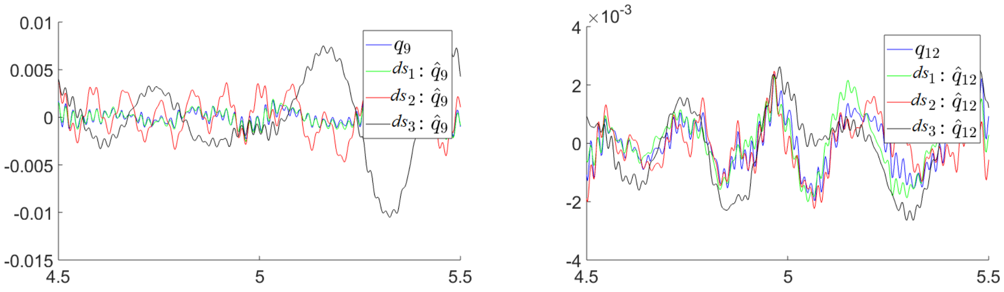

(e) mode 9 (f) mode 12

Figure 4.11: Run 1: simulated response of the more interesting modal coordinates against the their estimation by means of 7-level decomposition obtained with 3 different sensor layouts.

the left half of the aircraft). From dataset 4 to 8, a sensor is progressively removed starting from the tip in a zigzag pattern. From dataset 9 to 11, the sensor is removed from the root by following the same pattern.

Fig. 4.13 shows the trend of $\overline{TRAC}_{\mathsf{q}\hat{\mathsf{q}}}$ with respect to the number of strain gages involved and the two different patterns used for the remotion of the strain gages (blue line represent the pattern that starts from the tip, whereas the red one the case where the strain gages are removed starting from the root). It is worth noting that in addition to the number of sensors involved, also their distribution is important to obtain a good observation. The results in Fig. 4.13 show how the configuration with dataset 8 (which should be the worst in terms of number of sensors involved) provides better results than configurations with datasets 9-11. It appears as if the removal of sensors 2 and 10 is a critical point. In the transition from datasets 10 to 11, the removal of sensors 7 and 15 instead seems to drastically improve the estimate. This mechanism is still unclear and needs further investigation.

4.3.3 Run 2: response to medium frequency turbulence

In this analysis the aircraft is assumed flying at speed of 15.0m/s with a characteristic gust length of $12.5\bar{c}$ (see case 2 in Tab. 4.2). The observer performances are assessed also with different turbulence conditions by comparing the same multi-level observer synthesized for the gust conditions in Sec. 4.3.2 with the multi-level observer synthesized for the current gust condition. The comparison between the simulated response against the observation is shown in Figs. (4.14,4.15) by means of time response of modes 1,3,5,6,9,12 and their PSDs. The figures compares the simulated response (blue lines) with the estimated modal coordinates obtained by means of the observer based on the statistics of Run 1 condition(blue lines) with respect to the same quantities estimated by means of a multi-level observer specifically synthesized for the current gust condition. The figures show an accurate observation at low frequencies (except for mode 12). Quantitatively, the estimation is still good since the $\overline{TRAC}$ is 0.9096. However this value is lower than the one obtained by synthesizing the gain matrices specifically for run 2 condition that provides a $\overline{TRAC}$ equal to 0.9236. This result, that seems obvious, suggests the use of a different observation system for each gust condition. It allows to get always an accurate estimate of elastic deformations.

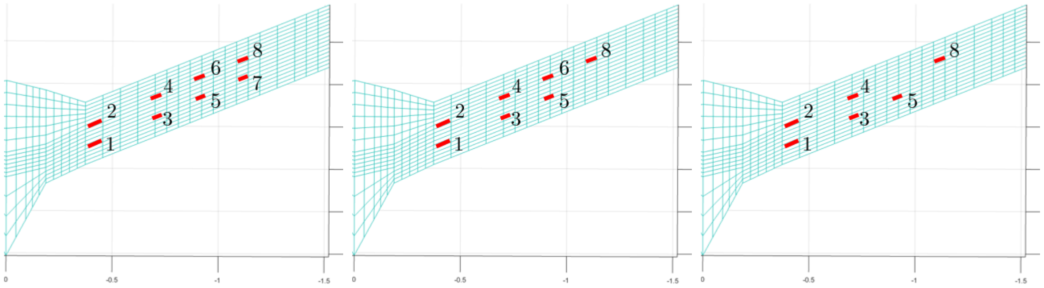

(a) dataset 4 (b) dataset 5 (c) dataset 6

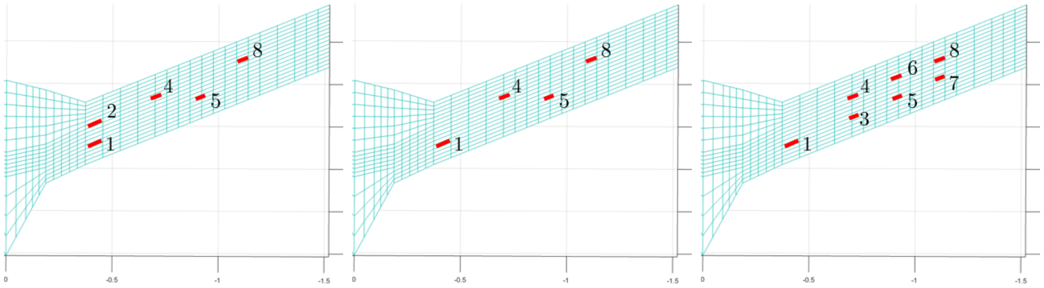

(d) dataset 7 (e) dataset 8 (f) dataset 9

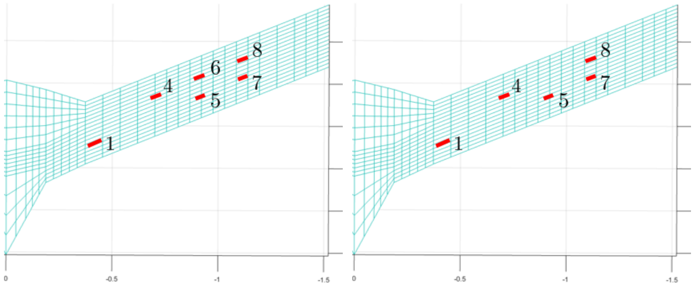

(g) dataset 10 (h) dataset 11

Figure 4.12: Strain gage datasets to be used for sensitivity analysis on the number and distribution of sensors.

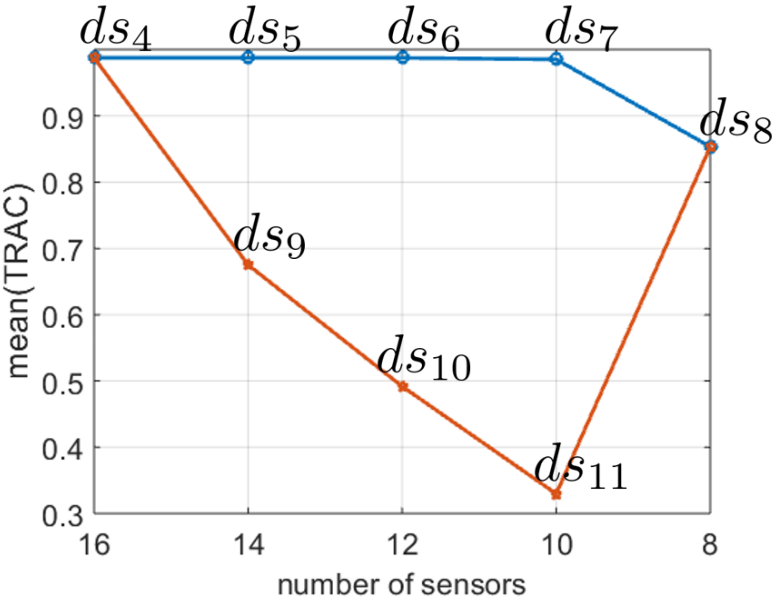

Figure 4.13: Dependency of the estimate with respect to the number of sensors.

4.3.4 Run 3: response to 1-cosine gust profile

The robustness of the observer in Sec. 4.3.2 is also evaluated by verifying what happens with a deterministic type of gust. In this analysis the aircraft is assumed to fly at speed of 17.4m/s. The *1-cosine* gust has a characteristic length equal to $3.125\bar{c}$. Fig. 4.16 shows the time response of simulated (blue lines) and observed systems (green lines). For this gust profile the excitation is practically mono-component. As a result, estimates at different frequencies will be significantly contaminated by noise (see Fig. 4.16f). For this run the $\overline{TRAC}$ is 0.3933. The value is influenced by the reduced length in time of the response. Being the most of response null, the estimate of the dynamics is highly influenced by measurement noise. Practically, at the beginning the TRAC is high and tends to zero as soon as the response goes to zero.

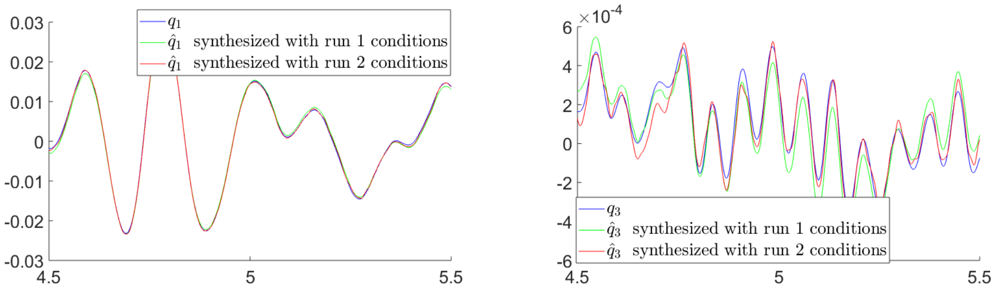

(a) mode 1 (b) mode 3

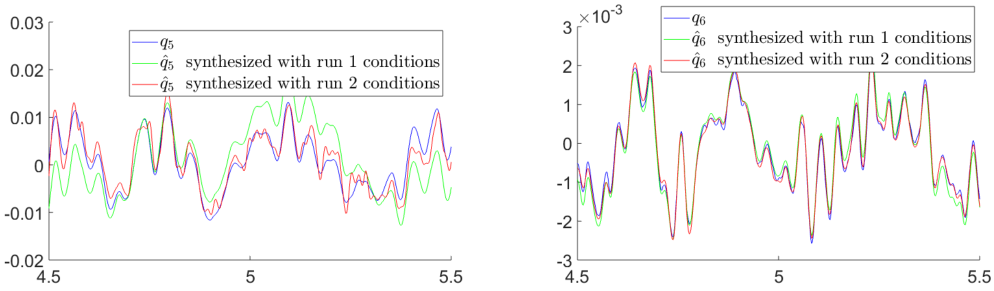

(c) mode 5 (d) mode 6

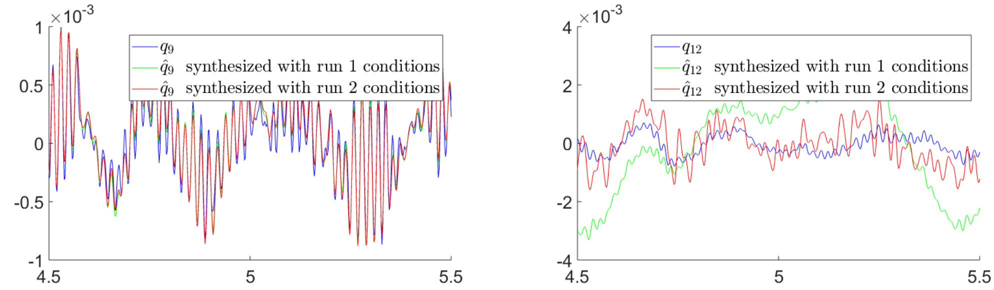

(e) mode 9 (f) mode 12

Figure 4.14: Run 2: simulated response of the more interesting modal coordinates against the their estimation by means of 7-level approximation synthesized specifically for run 1 and 2 gust conditions.

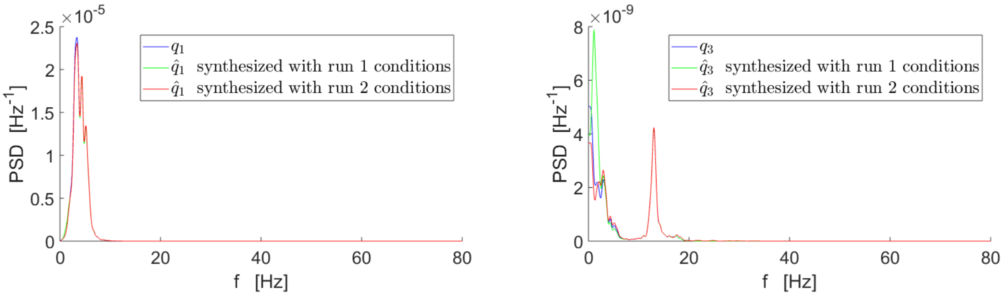

(a) mode 1 (b) mode 3

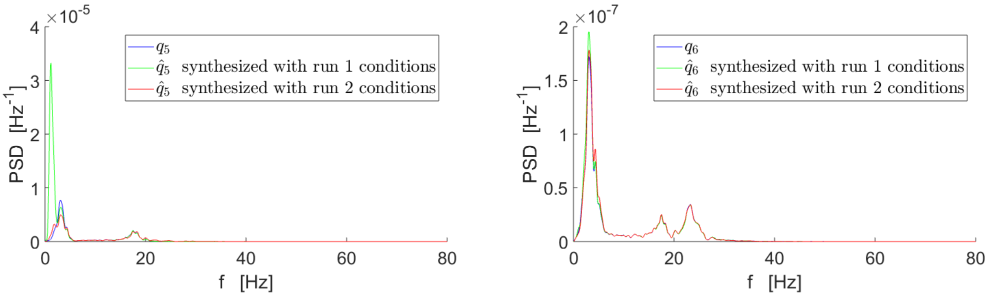

(c) mode 5 (d) mode 6

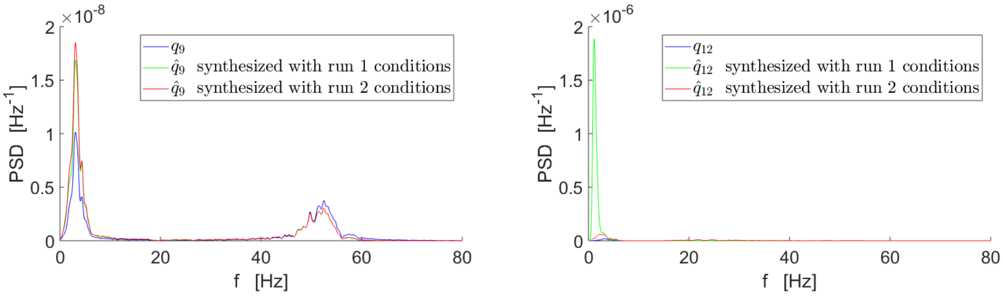

(e) mode 9 (f) mode 12

Figure 4.15: Run 2: PSD of simulated response of the more interesting modal coordinates against the PSD of their estimation by means of 7-level decomposition.

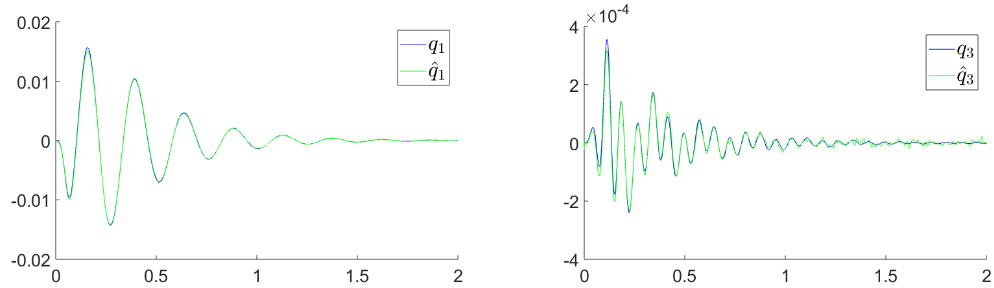

(a) mode 1 (b) mode 3

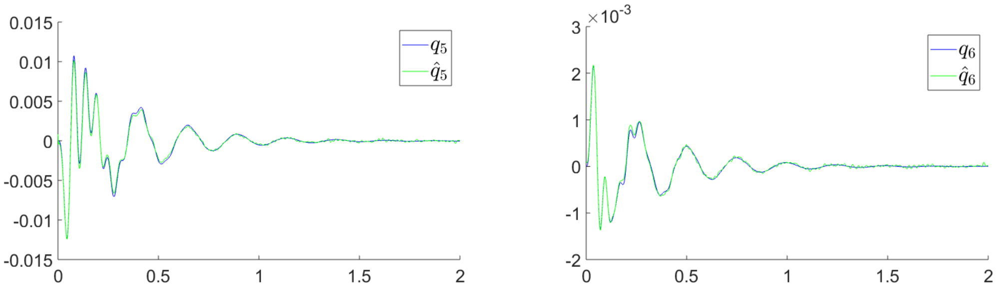

(c) mode 5 (d) mode 6

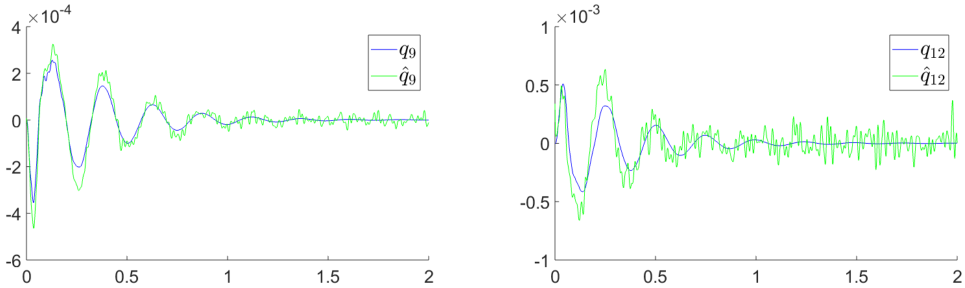

(e) mode 9 (f) mode 12

Figure 4.16: Run 3: simulated response of the more interesting modal coordinates against their estimation by means of 7-level decomposition.

Conclusions

The objective of this thesis was to yield methodologies for a real-time reliable estimation of loads and elastic deflections of marine and aeronautical structures, providing tools to improve the structural health monitoring vibration-based strategies. The methods generally used for SHM purposes are featured by signal processing of measures that aim to return parameters for the characterization of the structural health. However, a lack of spatial information remains. The virtual sensing strategies are inserted in this framework since they aim to provide physical quantities not directly accessible through measurement, such as displacement fields, external loads, stresses and strains that represent the core for a fine structural monitoring strategy.

The thesis activity has therefore had as its objective to develop virtual sensing methodologies that are more appropriate for the types of structure in question. The needful theoretical background for the development of these techniques lies in *i)* properly modeling the topology and the structural dynamics of the considered structures and *ii)* an in-depth knowledge of the environment where the considered structures operate and *iii)* of the type of data available through measurements. For the present purpose is fundamental that the numerical model (generally FEM) provides consistent data with the real behavior of the structure. Environmental models along with numerical or experimental frameworks are critical for the characterization of loads acting on the structures.

It has been seen that in literature the problem is generally dealt with by considering Kalman filter-based observers. These observers, however, are not tailored for the observation of structural dynamics of aircrafts and ships since they are not natural for mechanical systems and do not specifically use information on the environment. Indeed its knowledge is the key point of the observation strategies of structures operating under ambient loads that, in turn are the object of study and estimate.

After a careful review of the literature concerning problems of state estimation for structural problems, the works of Hernandez et al. were identified as the starting point for the development of the current observation techniques [18, 19, 20]. The thesis activity has led to the formulation of natural second order observers that better exploit the available measurement data and the intrinsic features of the system responses.

Therefore, two main developments have been proposed based on the general theory presented in [18].

1. The first proposal concerns the use of measurements stored during the so called *learning phase* prior to the observer's synthesis (see Sec. 2.3.1). The state estimators do not generally adapt to the stored data, but simply use the informations that *a priori* are provided to the observer, *i.e.*, the process noise (and therefore on external forcing) and measurement noise. In this activity it is proposed to use the measurements of the learning phase to guide the observer's synthesis. Please note that these measurements may be more than those currently available on board that are used for observation, thus enabling the convergence of the estimation even in the points no longer measured.

2. Next, it is proposed to combine the natural observer of the second order with the multi-resolution analysis. Structural systems generally behave differently at different scales based on the characteristics of external loads. Because of the state observers do not assume direct knowledge of external loads (but only their statistical distribution), they are generally designed to provide an estimate that minimizes the state error globally over the frequency domain. The use of multi-resolution analysis that decomposes the system into many sub-signals, each defined at a different time scale, can be used for the construction of multi-scale observer. This type of proposed observer is able to give back an estimation of the state by means of the synthesis of an optimal gain for each of the time scales on which the measurements are decomposed. This type of observation based on WMRA is only possible using a state observer like the one proposed in [18] that uses the PSDs to describe the statistics of external loads and noise.

The above mentioned methodologies have been applied to two different case studies: *i)* an experimental model of a surface vessel scaled model and *ii)* a flexible aircraft numerical model. The surface vessel model is a catamaran tested in towing-tank that experiences critical fluid-structure interaction phenomena such as slamming in the wetdeck region. It was used to validate the approach that employs the measurement statistics available from the *learning phase* . Three different experimental runs have been considered to show the effective use of this observer. A suitable reduced order model that employs the dynamic reduction technique was used to get a detailed description of the elastic deflections and loads exchanged at the interfaces between the segmented hulls and metallic backbone scaling the elastic behavior of the correspondent full-scale structure. The statistical properties to be included into the observation synthesis process were obtained by exploiting the same experimental data. The tool was proved to be useful for the study of hydroelastic phenomena occurring during the considered towing-tank tests and, specifically, to recognize particular structural dynamic behaviors in terms of elastic deflections and hydrodynamic loads. The definition of appropriate parameters, namely TRAC and FRAC, allowed to perform a rough sensitivity analysis on the distribution of the sensors, that, among the results confirms the capability of the proposed extension to improve the estimation when the statistics of removed sensors are inserted in the observer synthesis process. Furthermore, a quantification of the fatigue life reduction of each component during the towing-tank tests was provided by exploiting the reconstruction of the internal stress field together with the Miner's rule. This estimate of fatigue life reduction, although applied on scaled models, provides estimates of meaningless residual life values, can be tailored to full-scale structure, thus aiding the structure's maintenance.

The second case study concerned a flexible aircraft model freely inspired by Lockheed Martin X56-a *Body Freedom Flutter* [26]. It was used as numerical case study of the approach based on *multi-scale observer* . To this end, a virtual experiment was carried out using a toolbox developed during thesis activities for integrated modeling of aeroelasticity and flight dynamics. The observation synthesis was made by considering a model with the same mass and stiffness characteristics but with different damping features and, in some applications, also different flight conditions that may affect negatively the observation process. Goal of this case study was to demonstrate that the use of multi-resolution analysis generally provides better state estimation thanks to the specialization of the observer to each time-scale involved. Also for this case study, a sensitivity analysis was performed on the distribution and the number of sensors used that shows how the distribution of the sensors remains a critical problem for an effective observation strategy.

The methodologies presented are aimed at improving the estimation process and providing an observer that more broadly considers the amount of information available, exploiting the knowledge of known measurement data on the structure and the frequency definition of the assigned statistical properties. In this activity, we have acted on the core of the problem, that is, the state observer.

Nonetheless, potential margins for future development are still recognized. Specially, performing an observation that involves the optimal estimation of external loads as in Appendix B with a numerical/experimental application. The optimal estimation of external loads requires a more complex optimization process (which can eventually be carried out through multiple optimization processes in cascada). It also requires a detailed identification of process noise as a function of frequency, of which in this thesis activity only a rough description of the PSD has been assigned.

In the work some properties on the convergence properties of the observation remain to be understood. This problem is also closely related to the integration of optimal sensor placement strategies to the present methodologies.

The use of the present methodology on full-scale structures is still an open question which will require further steps. Based on the knowledge acquired from its application to a "laboratory" case, the present thesis has tried to highlight the requirements in order to apply the proposed technique to full-scale structures. The model uncertainties on the real structure, the presence of not modeled noise and any other unexpected effect may have an order of magnitude such to make the virtual sensing problem much more challenging but not impossible to be solved with the same approach.

The final goal of the research remains the monitoring of the health of the structure. If on one hand the monitoring of the loads and the fatigue life of each point is a goal already achievable with the virtual sensing patterns, the integration of virtual sensing for the recognition of damages and their location and quantification remains a goal on which continue to invest our energies.

Appendix A

Theoretical issues on wavelet and multi-resolution analysis

The aim of this appendix is to provide the theoretical background on wavelet multi-resolution analysis which is extensively applied to avoid some issues in the development of the involved techniques as applied to the framework of present work. For further details, the readers is addressed to [21, 43, 44].

A.1 Introduction remarks to wavelet transform

Wavelet analysis is a modern signal processing tool able to provide a picture of a function in time-scale (or in time-frequency). Its aim is the same of Short Time Fourier Transform (STFT) but the time-frequency picture is provided in a different way that makes wavelet analysis a more appealing approach for modern engineering applications. STFT is obtained performing the Fourier Transform in an user-defined time window in which the ratio between frequency and time resolution is suitably assigned. Let's consider a continuous-time signal $x(t) \in \mathcal{L}^2(\mathbb{R})$ that, for definition, has an infinite time resolution as well as a Fourier Transform with an infinite frequency resolution. When a sliding time window is applied to Fourier transform basis functions, making the time-frequency transform featured by two parameters t and f, the time-frequency resolution becomes finite (Heisenberg uncertainty principle). Assigning a time-window means fixing the time and frequency resolutions for the higher frequencies as for the lower-ones. A smarter time-frequency transform would adapt the time resolution as a function of the frequency. It is enabled by means of Continuous Wavelet Transform (CWT).

A.1.1 General remarks on Continuous Wavelet Transform

The wavelets are localized waves with a finite duration that are defined by dilating (stretching or compressing) and moving a chosen mother wavelet $\psi(t) \in \mathcal{L}^2(\mathbb{R})$ with $||\psi|| > 0$, that are not necessarily limited to exponential (or sinusoidal) functions as opposed to Fourier Transform. From the mother wavelet, a family of functions called daughter wavelets $\psi_{a,b}(t)$ such that

$$\psi_{a,b}(t) = \frac{1}{\sqrt{a}}\psi\left(\frac{t-b}{a}\right) \tag{A.1}$$

is defined as a function of the pair $(a, b) \in \mathbb{R}^+ \times \mathbb{R}$. The relationship in Eq. (A.1) respects the following properties

$$||\psi_{a,b}|| = ||\psi|| \tag{A.2a}$$

$$\lim_{(a,b)\to(a_0,b_0)} ||\psi_{a,b} - \psi_{a_0,b_0}|| = 0 \qquad \forall (a_0, b_0) \in \mathbb{R}^+ \times \mathbb{R} \tag{A.2b}$$

that represent, respectively, the norm conservation and the continuity. The coefficients a and b are, respectively, referred as the scale and translation parameters, namely the dilatation of the mother wavelet, and the time instant where the wavelet is centered over time axis. The family of wavelets $\psi_{a,b}$ allows to define the CWT of a function $x(t)$ by means of the following inner product:

$$CWT(a, b) = \int_{-\infty}^{\infty} \psi^*_{a,b}(t)\, x(t)\mathrm{d}t \tag{A.3}$$

that means the coefficients (a, b) measure the similarity between the function $x(t)$ and the wavelets $\psi_{a,b}$ that are limited in time and frequency. Evaluating the CWT at higher scales means performing the operation in Eq. (A.3) with more stretched wavelets meaning that the signal is evaluated at the lower frequencies. Being the wavelet more stretched, it is easy to infer that the higher is the scale, the higher is the frequency resolution as the lower is the time resolution.

A.1.2 Time-Frequency localization of wavelets

Taken a wavelet such that $t\psi(t) \in \mathcal{L}^2(\mathbb{R})$, it is possible to define the mean in time and the radius (standard deviation) as follow

$$\mu_\psi = \frac{1}{||\psi||^2}\int_{-\infty}^{\infty} t||\psi(t)||^2 \mathrm{d}t \tag{A.4a}$$

$$\Delta_\psi = \left(\frac{1}{||\psi||^2}\int_{-\infty}^{\infty} (t-\mu_\psi)^2||\psi(t)||^2 \mathrm{d}t\right)^{1/2} \tag{A.4b}$$

where the standard deviation is considered as an indicator of time resolution. It follows from Eqs. (A.1, A.4a, A.4b) that:

$$\mu_{\psi_{a,b}} = a\mu_\psi + b \tag{A.5a}$$

$$\Delta_{\psi_{a,b}} = a\Delta_\psi \tag{A.5b}$$

allowing to define the time-resolution and the center of the daughter wavelet according to the scale and translation parameters. Similarly, considered as $\tilde{\psi}$ the Fourier Transform of ψ, it is possible to identify the mean frequency and radius of the analyzing wavelet

$$\mu_{\tilde{\psi}} = \frac{1}{||\tilde{\psi}||^2}\int_{-\infty}^{\infty} t||\tilde{\psi}(\omega)||^2 \mathrm{d}\omega \tag{A.6a}$$

$$\Delta_{\tilde{\psi}} = \left(\frac{1}{||\tilde{\psi}||^2}\int_{-\infty}^{\infty} (\omega-\mu_{\tilde{\psi}})^2||\tilde{\psi}(\omega)||^2 \mathrm{d}t\right)^{1/2} \tag{A.6b}$$

and, in turn, the same quantities for the daughter wavelets:

$$\mu_{\tilde{\psi}_{a,b}} = \mu_{\tilde{\psi}}/a \tag{A.7a}$$

$$\Delta_{\tilde{\psi}_{a,b}} = \Delta_{\tilde{\psi}}/a \tag{A.7b}$$

defining the mean frequency and the frequency-resolution of the wavelets as a function of scale and translation parameters. As for the considerations on time-frequency resolution in STFT, the Heisenberg principle of indetermination states that $\Delta_\psi\Delta_{\tilde{\psi}} \geq 1/2$, namely, that it is not possible to be resolutive in frequency and in time at the same time [44]. In wavelet analysis, the mother wavelet is dilated and shifted maintaining the product $\Delta_\psi\Delta_{\tilde{\psi}}$ unmodified. Here, there is the great advantage of the CWT with respect the STFT, that tunes the time resolution, and, in turn, the frequency resolution as a function of the frequency content (see Eq. A.7b).

A.1.3 Toward Discrete Wavelet Transform

CWT also admits an own inverse transform

$$x(t) = \frac{1}{K_\psi} \int_{a=-\infty}^{a=\infty} \int_{b=-\infty}^{b=\infty} CWT(a,b) \psi_{a,b}(t) \frac{1}{a^2} \mathrm{d}b \mathrm{d}a \tag{A.8}$$

where K_ψ depends on the kind of wavelet involved. However, the daughter wavelets basis is more than complete leading to redundancy in CWT. In order to avoid the redundancy, the idea was to define a new family of wavelets by means of a discrete number of parameters, chosen among the integers $\mathbb{Z}$. The standard way to discretize wavelet transform is to use a set of discrete dilation and translation parameters expressed as in the following dyadic way:

$$\begin{aligned} a &= 2^{-j} \\ b &= k\,2^{-j} \end{aligned}$$

where the pair $(j,k) \in \mathbb{Z}$ refers to discrete scale and translation parameter. The daughter wavelets are defined as follows

$$\psi_{j,k}(t) = 2^{j/2} \psi\left(2^j t - k\right) \tag{A.9}$$

providing the following Discrete Wavelet Transform (DWT):

$$C_{j,k} = \langle\, \psi_{j,k}(t), x(t) \rangle \tag{A.10}$$

The mother wavelet $\psi(t)$ must be chosen so having that $\psi_{j,k}$ make up a Riesz [1] basis in $\mathcal{L}^2(\mathbb{R})$. If the wavelet ψ is such that $\psi_{j,k}$ is also an orthogonal basis, it is possible to obtain an orthogonal wavelet transform so having

$$x(t) = \sum_{j=-\infty}^{\infty} \sum_{k=-\infty}^{\infty} \langle\, \psi_{j,k}(t), x(t) \rangle \psi_{j,k}(t) \tag{A.13}$$

---

[1] it means that the linear span of $\psi_{j,k}(t)$ is dense in $\mathcal{L}^2(\mathbb{R})$ and there exists a dual basis $\bar{\psi}_{l,m}(t)$ such that

$$\langle\, \psi_{j,k}(t), \bar{\psi}_{l,m}(t) \,\rangle = \delta_{jl}\delta_{km} \qquad j,k,l,m \in \mathbb{Z} \tag{A.11}$$

and

$$\bar{\psi}_{j,k}(t) = 2^{j/2} \bar{\psi}\left(2^j t - k\right) \tag{A.12}$$

that allows to decompose a signal $x(t)$ by using a minimum number of parameters.

Now, consider the subspaces $\mathcal{W}_j$ generated by including $\psi_{j,k} : k \in \mathbb{Z}$ such that $\mathcal{W}_j \perp \mathcal{W}_l \; l \neq j$, given by the assumption that the $\psi_{j,k}$ form an orthogonal basis. The Hilbert space $\mathcal{L}^2(\mathbb{R})$ is given by

$$\mathcal{L}^2(\mathbb{R}) = \mathcal{W}_1 \oplus \mathcal{W}_2 \oplus ... + \mathcal{W}_j \oplus +... \tag{A.14}$$

At the same time, a signal $x(t) \in \mathcal{L}^2(\mathbb{R})$ can be decomposed as sum of sub-signals

$$x(t) = \sum_{j=-\infty}^{\infty} x^{(\mathcal{W}_j)}(t) \tag{A.15}$$

where $x^{(\mathcal{W}_j)}(t) \in \mathcal{W}_j \forall j \in \mathbb{Z}$. It is worth to notice that the frequency content of each level, namely $\mu_{\tilde{\psi}_{j,k}}$ and $\Delta_{\tilde{\psi}_{j,k}}$ is generated by the choice of the mother wavelet and its dilatation.

A.2 Wavelet multi-resolution analysis

Wavelet Multi-Resolution Analysis (WMRA) is a useful tool that allows to decompose a discrete signal $x(t)$ into various resolution scales. At a given scale j, the signal is represented by means of an approximation (containing the low-frequency features of the signal) plus a certain number of details.

Considering orthogonal wavelets, multi-Resolution Analysis is a series of closed subspaces $\mathcal{V}_j \in \mathcal{L}^2(\mathbb{R})$ that satisfy different properties than $\mathcal{W}_j$ [44]:

$$\mathcal{V}_j \subseteq \mathcal{V}_{j+1} \qquad \forall j \in \mathbb{Z} \tag{A.16a}$$

$$\cup_{j\in\mathbb{Z}} \mathcal{V}_j = \mathcal{L}^2(\mathbb{R}) \tag{A.16b}$$

$$\cap_{j\in\mathbb{Z}} \mathcal{V}_j = \{0\} \tag{A.16c}$$

$$f(t) \in \mathcal{V}_{j-1} \Longleftrightarrow f(2t) \in \mathcal{V}_j \tag{A.16d}$$

$$f(t) \in \mathcal{V}_j \Longleftrightarrow f(t - e^{-j}k) \in \mathcal{V}_j \qquad \forall k \in \mathbb{Z} \tag{A.16e}$$

It is worth to notice that, as opposed to the subspaces $\mathcal{W}_j$, the subspaces $\mathcal{V}_j$ are nested (see Eq. (A.16a)) that means the subspace at scale j includes the subspaces at previous levels. The subspace $\mathcal{V}_0$ is spanned by a scaling function (also called *father function*) $\phi(t) \in \mathcal{L}^2(\mathbb{R})$ by the orthogonal set $\{\phi_{0,k}\, k \in \mathbb{Z}\}$.

Given a signal $x(t) \in \mathcal{L}^2(\mathbb{R})$, the approximation at the scale j can be written as:

$$x^{(V_j)}(t) = \sum_{k=-\infty}^{\infty} c^{(j)}(k)\phi(2^j t - k) \tag{A.17}$$

with

$$c^{(j)}(k) = \langle \phi_{j,k}(t), x(t) \rangle_t \tag{A.18}$$

From Eq. (A.16a), being the subspace $\mathcal{V}^j$ nested in $\mathcal{V}^{j+1}$, it follows that it is possible to express the generating functions of $\mathcal{V}^{j+1}$ as linear combination of the ones of $\mathcal{V}^j$ and in particular:

$$\phi(2^j t) = \sum_{k=-\infty}^{\infty} h(k)\phi(2^{j+1} t - k) \tag{A.19}$$

The subspace $\mathcal{V}^{j+1}$ can be defined as the sum of $\mathcal{V}^j$ and the detail space $\mathcal{W}^j$:

$$\mathcal{V}_{j+1} = \mathcal{V}_j \oplus \mathcal{W}_j \tag{A.20}$$

The higher is the scale parameter j, the finer is the approximation $x^{(j)}(t)$ of $x(t)$. Eqs. (A.17, A.20) yield

$$x^{(V_{j+1})}(t) = x^{(V_j)}(t) + \sum_{k=-\infty}^{\infty} d^{(j)}(k)\psi(2^j t - k) \tag{A.21}$$

with

$$d^{(j)}(k) = \langle \psi_{j,k}(t), x(t) \rangle_t \tag{A.22}$$

Summarizing the concepts above, given a signal $x^{(\mathcal{V}_0)} \in \mathcal{V}_0$, the N-level approximation is given by:

$$x^{(\mathcal{V}_0)}(t) = x^{(\mathcal{V}_{-N})}(t) + \sum_{j=0}^{N-1} x^{(\mathcal{W}_{-N+j})}(t) \tag{A.23}$$

that is the sum of an approximation and N details.

The wavelets $\psi(2^j)$ are expressed by means of the following relationship:

$$\psi(2^j t) = \sum_{k=-\infty}^{\infty} g(k)\phi(2^{j+1}t - k) \tag{A.24}$$

From Eqs. (A.19, A.24) it is possible to recognize $h(k)$ and $g(k)$ as digital filter pair that are computed as:

$$h(k) = \int_{t=0}^{\infty} \phi(t)\phi^*(2t - k) \tag{A.25a}$$

$$g(k) = \int_{t=0}^{\infty} \psi(t)\phi^*(2t - k) \tag{A.25b}$$

$h(k)$ and $g(k)$ form a quadrature conjugate mirror filter pair, where $h(k)$ acts as low-pass and $g(k)$ as high-pass filter. Their relationship is given by

$$g(k) = (-1)^k h(-k + 1 + 2n) \qquad \forall n \in \mathbb{Z} \tag{A.26}$$

$g(k)$ and $h(k)$ along with Eqs. (A.18, A.22) allow to express the coefficients at level j as a function of the coefficients at the finer approximation:

$$c^{(j)}(k) = \sum_{n=-\infty}^{\infty} h^*(n - 2k)c^{(j+1)}(n) \tag{A.27a}$$

$$d^{(j)}(k) = \sum_{n=-\infty}^{\infty} g^*(n - 2k)c^{(j+1)}(n) \tag{A.27b}$$

The definitions in Eqs. (A.27a,A.27b) lead to the Mallat algorithm [21] for the fast calculation of DWT and reconstruction procedure. Indeed, different wavelets scales are computable by means of successive filtering and down sampling strategy.

In practical applications $x(t)$ is a sampled signal. It means that the finest approximation subspace depends on the sampling frequency. Let's consider a signal $x(t) \in \mathcal{V}_J$. Fig.A.1 illustrates a N-level decomposition tree. The discrete signal $x(t_k)$ is first decomposed by means of the digital filter pair in the first level of approximation and detail. After the down-sampling, the procedure is recursively applied to the approximations until the desired N-level is reached, providing a cost-effective strategy to compute the discrete wavelet coefficients. The DWT coefficients are then used in the reconstruction process by means of up-sampling and filtering procedure as shown in Fig. A.2.

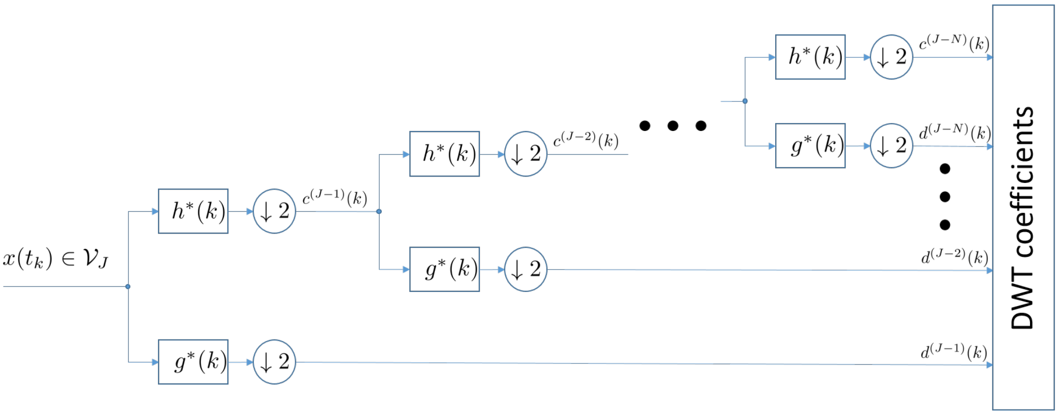

Figure A.1: WMRA decomposition diagram.

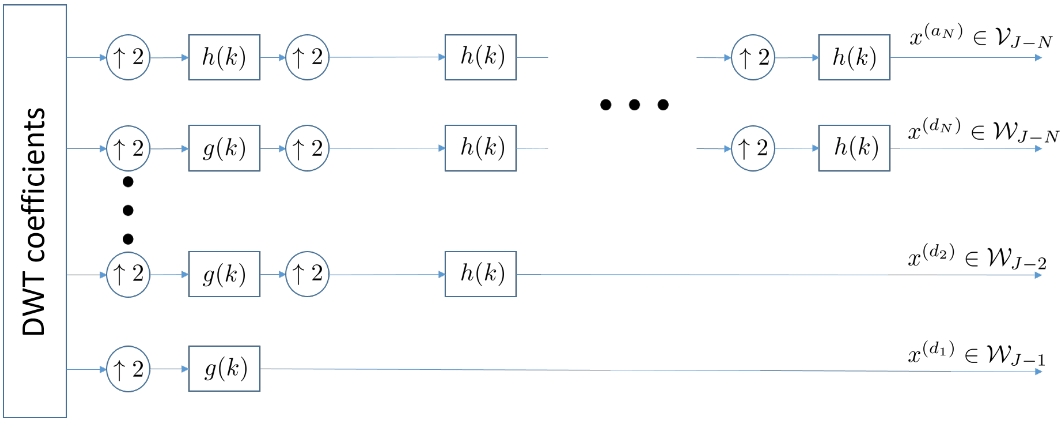

Figure A.2: WMRA reconstruction diagram.

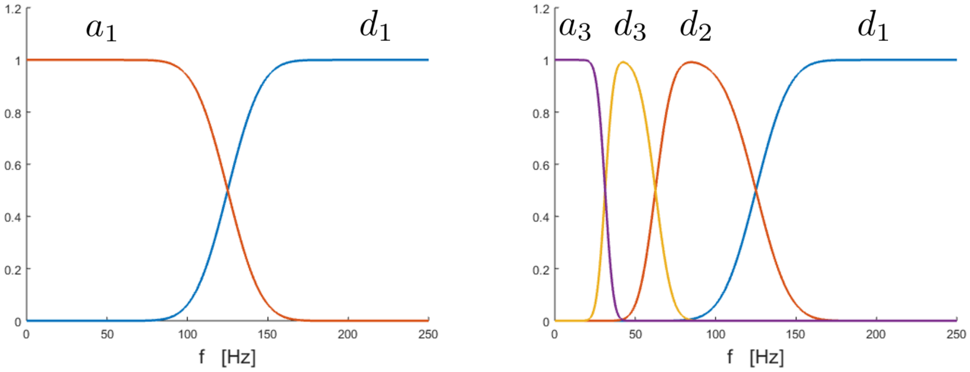

(a) 1-level approximation

(b) 3-level approximation

Figure A.3: Frequency domain representation of WMRA.

As a result of the reconstruction, N+1 sub-signals are obtained so having that:

$$x(t) = x^{(a_N)} + \sum_{j=1}^{N} x^{(d_j)} \tag{A.28}$$

It is worth to notice that, in order to be consistent with other engineering applications, the notation related to the sub-signals has been modified such that $x^{(a_N)} \equiv x^{(V_{J-N})}$ and $x^{(d_j)} \equiv x^{(W_{J-j})}$. This notation switching hides a subtlety to which the reader must pay attention. In the previous notation an increase of j implies a decrease of the time scale, while with the current-one an increase of j constitutes an increase in the time scale and therefore a lower frequency content of the *j-th* detail. The frequency of such a sub-signals is not unequivocally determinable since they are not computed by means of periodic functions, but their frequency content depend on the one of the scaling and wavelet function.

The quadrature mirror filters along with the Mallat algorithm provides a subdivision of the frequency content of the signal into N+1 scales. However, the frequency content between two contiguous scales presents a certain overlapping that can be seen in Fig. A.3 that is obtained by using *db12* wavelet [43]. This overlapping depends on the choice of particular wavelets and their vanishing moments [2]. In this

---

[2] The degree of continuity of a wavelet depends on the vanishing moment. A wavelet is said to have p vanishing moments if

$$\int_{-\infty}^{+\infty} t^k \psi(t) \mathrm{d}t = 0 \qquad k = 1, \ldots, p$$

figure the absolute value of equivalent filtering transfer functions in frequency domain are shown. They correspond to the absolute value of the Fourier transform of the wavelet at each scale. In Fig. A.3(a) the red line represents the transfer function of the approximation whilst the blue-one is the transfer function of the detail. In Fig. A.3(b) the transfer function of the approximation at level 3 is the purple line, the blue line is the same of Fig. A.3(a) and represent the transfer function of detail at level 1. The red and yellow lines represent the transfer function of the details of the discrete scales 2 and 3. Note that these two functions, along with the approximation can be obtained by means of multiple filters.

Appendix B

Optimal estimation of external forces

In Sec. 1.2.1 the Augmented Kalman filter was introduced to consider in the estimation process also the external forces. This section aims at the same goal: get an estimation of external forces in a similar way, but for a natural second order system. Recall Eq. (1.48) by adding the estimation of external forces:

$$\begin{aligned}
&\mathsf{M}\ddot{\hat{\mathsf{q}}} + \mathsf{D}\dot{\hat{\mathsf{q}}} + \mathsf{K}\hat{\mathsf{q}} = \hat{\mathsf{f}} + \mathsf{L}_v\mathsf{r} = \Big(\mathsf{L}_f + \mathsf{L}_v\Big)\mathsf{r} \\
&\hat{\mathsf{f}} = \mathsf{L}_f\mathsf{r} \\
&\hat{\mathsf{y}} = \mathsf{S}(t) * \hat{\mathsf{q}}
\end{aligned} \tag{B.1}$$

where L_v is the observer compensating the process noise and L_f is a gain matrix that attempts to estimate the external forces, that, in turn, reentries in the second order observation equation. Now, besides the state error $\varepsilon = \mathsf{q} - \hat{\mathsf{q}}$, let's define the external force error as

$$\varepsilon_{\mathsf{f}} = \mathsf{f} - \hat{\mathsf{f}} \tag{B.2}$$

and the classical second order gain matrix as $\mathsf{L} = \mathsf{L}_v + \mathsf{L}_f$. In this manner, it is possible to get a synthesis of L by minimizing the covariance associated to ε as in Sec. 1.2.1. Once L is synthesized, and we get $\Phi_{\varepsilon\varepsilon}(\omega)$, we want to find the values of L_f that minimize the external force error. By definition:

$$\varepsilon_{\mathsf{f}} = \mathsf{f} - \hat{\mathsf{f}} = \mathsf{f} - \mathsf{L}_f\mathsf{r} = \mathsf{f} - \mathsf{L}_f\Big(\mathsf{v} + \mathsf{S}(t) * \varepsilon\Big) \tag{B.3}$$

Defining as $\Phi_{\varepsilon_{\mathsf{f}}\varepsilon_{\mathsf{f}}}(\omega)$ the power spectral density of the external forces error, and considering that the state error is correlated with external forces and measurement noise (see Eq. (1.53)), we get:

$$\begin{aligned}\Phi_{\varepsilon_{\mathsf{f}}\varepsilon_{\mathsf{f}}} = \quad & \Phi_{\mathsf{ff}} + \mathsf{L}_f \Phi_{\mathsf{vv}} \mathsf{L}_f^{\mathsf{T}} + (\mathsf{L}_f \tilde{\mathsf{S}})^* \Phi_{\varepsilon\varepsilon} (\mathsf{L}_f \tilde{\mathsf{S}})^{\mathsf{T}} - (\mathsf{L}_f \tilde{\mathsf{S}} \tilde{\mathsf{H}}_O)^* \Phi_{\mathsf{ff}} \\ & + \Phi_{\mathsf{ff}} (\mathsf{L}_f \tilde{\mathsf{S}} \tilde{\mathsf{H}}_O)^{\mathsf{T}} + (\mathsf{L}_f \tilde{\mathsf{S}} \mathsf{H}_O \mathsf{L})^* \Phi_{\mathsf{vv}} \mathsf{L}_f^{\mathsf{T}} + \mathsf{L}_f^* \Phi_{\mathsf{vv}} (\mathsf{L}_f \tilde{\mathsf{S}} \mathsf{H}_O \mathsf{L})^{\mathsf{T}}\end{aligned} \tag{B.4}$$

In a similar way than in Secs. (1.2.1,2.3.1), we define the covariance of the external force error:

$$\Sigma_{\mathsf{ff}}^2 = \int_{-\infty}^{+\infty} \Phi_{\varepsilon_{\mathsf{f}}\varepsilon_{\mathsf{f}}}(\omega) \mathrm{d}\omega \tag{B.5}$$

As in Sec. 2.3.1 a multi-objective optimization can be performed considering the minimization of $tr(\Sigma_{\mathsf{ff}}^2)$ as one of the objectives. However, in this manner the number of free parameters are doubled so increasing the computational effort. Alternatively, it is possible to consider the minimization of ε_{f} less important than ε and, as a consequence, solve another optimization process in cascade with respect to the one associated to the state error.

Appendix C

Estimation of the accumulated damage

In this section, the elastic deflections estimated for the runs in Chap. 3 are used to enable the computation of the accumulated damage at every point of the structure. The estimation of accumulated damage is critical for predictive maintenance applications since they can provide useful information to understand which parts or components of the structure have reached or are about to reach the useful life limits. In this case the object of the present analysis is the load-bearing structure of the catamaran, namely the truss frame. However, the catamaran scaled model, even if it experiences considerable loads, will present internal stresses that are far from being comparable to those of the real structure, and consequently, also the fatigue life prediction presents results that are meaningless as compared to full-scale structures. Nonetheless, the qualitative results that have been obtained illustrates the potential of the approach based on stress field estimation. The estimation approach, indeed, aims to provide an estimation of the displacement field (and in turn of the stresses throughout the structure) by minimizing the errors given by disturbances and complexity of geometries. For the estimation of fatigue life reduction, it has been used the Basquin relationship, that links the number of fatigue cycles with the cyclic load σ_a (expressed in MPa and defined as the half of the amplitude of oscillation) on a logarithmic scale:

$$\sigma_a^m N = C$$

where N is the number of cycles and m and C are coefficients of the regression line that approximates the Wöhler curve. For this case study, m and C have been chosen equal to 4.1 and $3.15e + 14$, respectively.

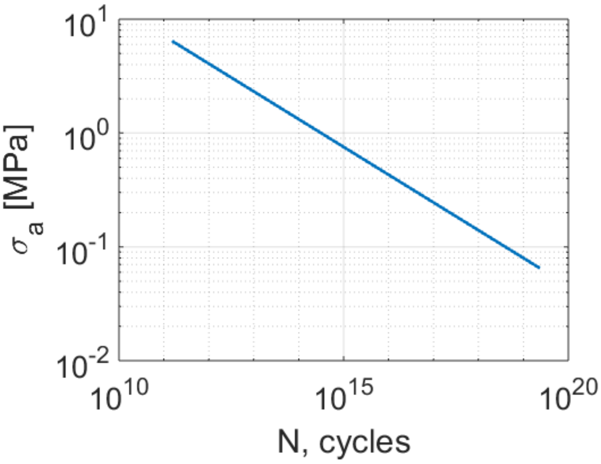

Figure C.1: Stress-cycles curve for the stress range of interest of the present case study. This plot does not provide realistic values for real structures.

Fig. C.1 shows the Stress-Cycles curve in the range of stress that the catamaran experiences. It can be noticed that, even if the structure experienced always the maximum of stress, more than 10^{11} cycles would be necessary to fulfill the fatigue life of the structure. The structure experiences loads at various levels of excitation. Each of these levels of load consumes the life with different number of cycles. Miner's rule [38] states that the damage accumulated D by the material due to the cyclic load is proportional to the ratio between the number of cycles that the structure has been undergone n_i and the number of cycles N_i that causes the failure at the *i-th* stress level σ_{a_i}:

$$D = \sum_{i=1}^{N_{stress}} \frac{n_i}{N_i}$$

This cumulative damage can be computed by means of traditional methods like *rain flow* [39]. By means of the estimation process presented in this thesis, it is possible to get a full picture of the stress loads throughout the structure. In particular, dealing with a complex 3-D structure, we need to recognize a principal stress direction to which we will apply the Miner's rule. However, the present structure has a main load directions in every point as it is suggested by the expected external loads. Without loss of generality we can state that the principal loads will be everywhere longitudinal to the truss directions. In this manner it is possible to plot the accumulated damage for each element of the metallic frame.

Fig. C.2 represents the damage accumulated by each element at the end of all the tests discussed above. The values highlighted in the color-bar are normalized with respect to the damage maximum value D_{max}, that is expressed in caption for each of the runs. It can be noticed that Run 1 and Run 3 accumulates much more damage than Run 2 due to the slamming phenomena present in the wetdeck region. In fact, the wetdeck fore bar is the most damaged area for both the runs. During Run 2 the structure accumulates more damage on the trusses (in particular on the left-one, likely due to estimated asymmetries of the external load).

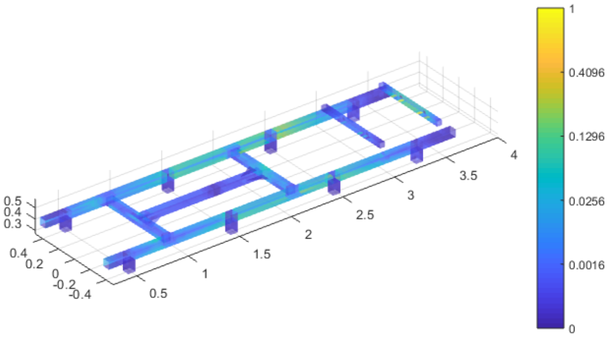

(a) Run 1: $D_{max} = 2.51e - 10$.

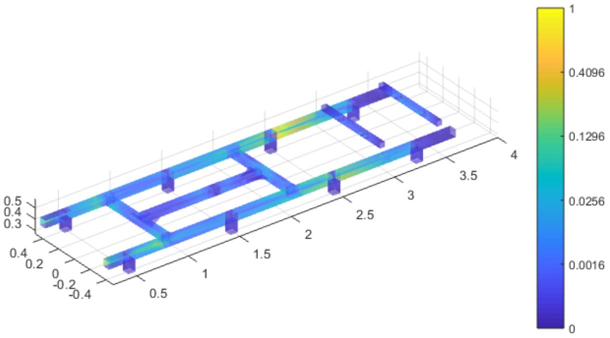

(b) Run 2: $D_{max} = 1.33e - 13$.

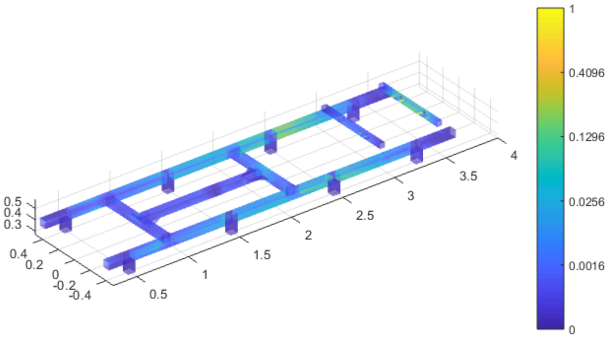

(c) Run 3: $D_{max} = 2.76e - 10$.

Figure C.2: Visualization of fatigue life consumption estimation. The color scale indicates the normalized life consumption for each element at the end of the run.

Appendix D

Integrated model of flight dynamics and aeroelasticity

The integrated model of flight dynamics and aeroelasticity developed in Ref. [42] assumes a set of body axes that verifies the practical mean-axis constraints [45] to describe the nonlinear motion of a flexible vehicle as a whole. Structural displacements with respect to these axes are assumed small and represented in terms of a modal decomposition. Inertial coupling between rigid-body and elastic degrees-of-freedom is described in terms of a reduced set of coefficients which can be evaluated using a FEM model of the aircraft. Fully nonlinear equations of rigid-body motion and structural dynamics are obtained by the weak formulation of Cauchy's equation for a generic unrestrained continuum [49] and linearized around steady maneuvers for stability and response analysis.

D.1 Kinematics

The motion of an unrestrained flexible vehicle is described by assuming a set of practical mean axes (PMAs) of unit vectors $\mathbf{e}_k$ $(k = 1, 2, 3)$ as body reference frame. A set of inertial axes of unit vectors $\mathbf{i}_k$ $(k = 1, 2, 3)$ is also introduced. According to the practical mean-axis constraints [45], the PMA frame has origin at the instantaneous aircraft center of mass and it is fixed to the undeformed configuration (see Fig. D.1).

The position of a generic vehicle material point P in the inertial coordinate

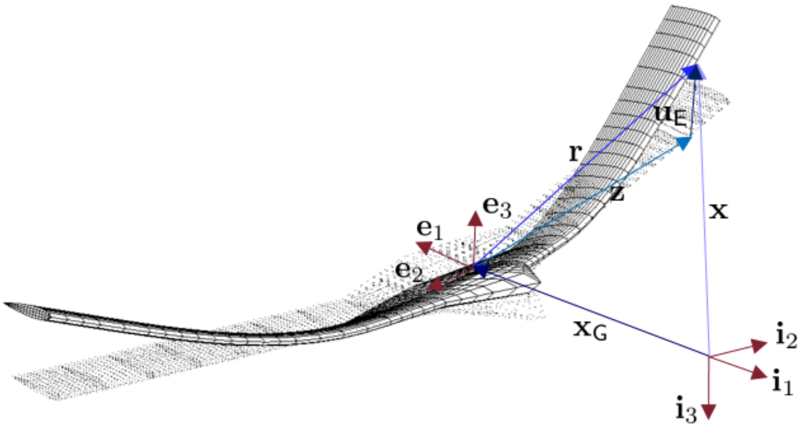

Figure D.1: Reference frames to describe the motion of an unrestrained flexible vehicle.

system is given by [1]

$$\mathbf{x} = \mathbf{x}_\mathsf{G} + \mathbf{z} + \mathbf{u}_\mathsf{E} \tag{D.1}$$

where $\mathbf{x}_\mathsf{G} = x_\mathsf{G}\mathbf{i}_1 + y_\mathsf{G}\mathbf{i}_2 + z_\mathsf{G}\mathbf{i}_3$ is the instantaneous position of the center of mass, $\mathbf{z} = z_1\mathbf{e}_1 + z_2\mathbf{e}_2 + z_3\mathbf{e}_3$ is the relative position of P in the PMAs in undeformed configuration, and

$$\mathbf{u}_\mathsf{E} = \sum_{n=1}^{\infty} q_n \boldsymbol{\phi}_n^\mathsf{E} \tag{D.2}$$

is the elastic displacement. In Eq. (D.2), $\boldsymbol{\phi}_n^\mathsf{E}$ is the nth elastic mode shape of the unconstrained structure and q_n the corresponding modal coordinate. The relative position of P with respect to the PMAs in *deformed* configuration is given by

$$\mathbf{r} := \mathbf{x} - \mathbf{x}_\mathsf{G} = \mathbf{z} + \mathbf{u}_\mathsf{E} \tag{D.3}$$

From Eqs. (D.1), (D.2), and (D.3), the absolute velocity and acceleration of P follow

---

[1] Note that this representation is not in conflict with the one of Sec. 1.1. Indeed:

$$\mathbf{x} = \mathbf{x}_\mathsf{G} + \mathbf{r}$$
$$\mathring{\mathbf{x}} = \mathbf{x}_\mathsf{G} + \mathbf{z}$$

as

$$\begin{aligned}\mathbf{v} &= \mathbf{v}_{\mathsf{G}} + \boldsymbol{\omega} \times \mathbf{r} + \mathbf{v}_{\mathsf{E}} \\ \mathbf{a} &= \dot{\mathbf{v}}_{\mathsf{G}} + \dot{\boldsymbol{\omega}} \times \mathbf{r} + \boldsymbol{\omega} \times (\boldsymbol{\omega} \times \mathbf{r}) + 2\boldsymbol{\omega} \times \mathbf{v}_{\mathsf{E}} + \mathbf{a}_{\mathsf{E}}\end{aligned} \tag{D.4}$$

where $\mathbf{v}_{\mathsf{G}} = u\mathbf{e}_1 + v\mathbf{e}_2 + w\mathbf{e}_3$ is the velocity of the center of mass, $\boldsymbol{\omega} = p\mathbf{e}_1 + q\mathbf{e}_2 + r\mathbf{e}_3$ is the angular velocity of the PMA frame with respect to the inertial frame, and

$$\mathbf{v}_{\mathsf{E}} = \sum_{n=1}^{\infty} \dot{q}_n \boldsymbol{\phi}_n^{\mathsf{E}} \qquad \mathbf{a}_{\mathsf{E}} = \sum_{n=1}^{\infty} \ddot{q}_n \boldsymbol{\phi}_n^{\mathsf{E}} \tag{D.5}$$

are the relative velocity and acceleration due to elastic motion.

D.2 Inertial coupling

Inertial coupling between rigid-body and elastic degrees of freedom vanishes when a mean-axis body reference frame is used [50], but not in the case of a PMA frame [51, 42]. In the present model, the residual inertial coupling terms in the equations of motion are not neglected (as frequently done, see Refs. [45, 46, 40]). This allows to study the influence of inertial versus aerodynamic coupling effects for each application without preliminary simplifications [42]. Coupling vectors and tensors to describe inertia coupling effects are introduced below for a generic continuous structure and can be evaluated for complex configurations described by a FEM model as reported in Ref. [42].

The aircraft inertia tensor in *deformed* configuration is written as

$$\mathbf{J} = \langle \mathbf{r} \otimes \mathbf{r} \rangle = \mathbf{J}_0 + 2\sum_{n=1}^{\infty} \mathbf{J}_n q_n + \sum_{n,m=1}^{\infty} \mathbf{J}_{nm} q_n q_m \tag{D.6}$$

having introduced the integral operator:

$$\langle \mathbf{a} \otimes \mathbf{b} \rangle := \iiint_{\mathcal{V}} \rho \left[(\mathbf{a} \cdot \mathbf{b})\, \mathbf{I} - \mathbf{a} \otimes \mathbf{b} \right] \mathrm{d}\mathcal{V} \tag{D.7}$$

In Eq. (D.6), $\mathbf{J}_0$ is the inertia tensor in *undeformed* configuration, while

$$\mathbf{J}_n := \frac{1}{2}\left[\langle \mathbf{z} \otimes \boldsymbol{\phi}_n^{\mathsf{E}} \rangle + \langle \boldsymbol{\phi}_n^{\mathsf{E}} \otimes \mathbf{z} \rangle \right] \qquad \mathbf{J}_{nm} := \frac{1}{2}\left[\langle \boldsymbol{\phi}_n^{\mathsf{E}} \otimes \boldsymbol{\phi}_m^{\mathsf{E}} \rangle + \langle \boldsymbol{\phi}_m^{\mathsf{E}} \otimes \boldsymbol{\phi}_n^{\mathsf{E}} \rangle \right] \tag{D.8}$$

are first- and second-order coupling tensors. The sensitivity of the inertia tensor (D.6) on the nth modal coordinate is described by the tensor

$$\mathbf{Y}_n := \operatorname{sym}\langle \mathbf{r} \otimes \boldsymbol{\phi}_n^{\mathsf{E}} \rangle = \mathbf{J}_n + \sum_{m=1}^{\infty} \mathbf{J}_{nm} q_m = \frac{1}{2}\frac{\partial \mathbf{J}}{\partial q_n} \tag{D.9}$$

The following inertial coupling vectors are also introduced:

$$\mathbf{b}_{nm} := \iiint_{\mathcal{V}} \rho \boldsymbol{\phi}_n^{\mathsf{E}} \times \boldsymbol{\phi}_m^{\mathsf{E}} \, \mathrm{d}\mathcal{V} = -\mathbf{b}_{mn} \tag{D.10}$$

Using Eqs. (D.6), (D.8), and (D.10), the angular momentum of a generic flexible body is written as

$$\mathbf{h}_{\mathsf{G}} = \iiint_{\mathcal{V}} \rho \mathbf{r} \times (\boldsymbol{\omega} \times \mathbf{r}) \, \mathrm{d}\mathcal{V} + \iiint_{\mathcal{V}} \rho \mathbf{u}_{\mathsf{E}} \times \mathbf{v}_{\mathsf{E}} \, \mathrm{d}\mathcal{V} = \mathbf{J}\boldsymbol{\omega} + \sum_{n,m=1}^{\infty} \mathbf{b}_{nm} q_n \dot{q}_m \tag{D.11}$$

D.3 Nonlinear equations of motion

Having assumed a PMA body frame, the equations of motion are as follows [42]:

1. Translational equations:

$$m \frac{\mathrm{d}\mathbf{v}_{\mathsf{G}}}{\mathrm{d}t} = \mathbf{f}_{\mathsf{T}} \tag{D.12}$$

2. Rotational equations:

$$\frac{\mathrm{d}\mathbf{h}_{\mathsf{G}}}{\mathrm{d}t} = \mathbf{m}_{\mathsf{G}} \tag{D.13}$$

3. Elastic equations:

$$m_n \ddot{q}_n - \frac{\mathrm{d}\boldsymbol{\omega}}{\mathrm{d}t} \cdot \sum_{m=1}^{\infty} \mathbf{b}_{nm} q_m - \boldsymbol{\omega} \cdot \mathbf{Y}_n \boldsymbol{\omega} - 2\boldsymbol{\omega} \cdot \sum_{m=1}^{\infty} \mathbf{b}_{nm} \dot{q}_m + k_n q_n = f_n \tag{D.14}$$

where m is the total aircraft mass, $\mathbf{f}_{\mathsf{T}} = X\mathbf{e}_1 + Y\mathbf{e}_2 + Z\mathbf{e}_3$ and $\mathbf{m}_{\mathsf{G}} = L\mathbf{e}_1 + M\mathbf{e}_2 + N\mathbf{e}_3$ are respectively the total force and the total moment with respect to the center of mass, m_n is the nth generalized mass, k_n the nth generalized stiffness, and f_n the nth generalized force obtained by projecting loads on the mode-shape functions.

Inertial coupling between rigid-body and structural dynamics stems from the angular momentum in Eq. (D.13) and due to the centrifugal, Coriolis, and angular acceleration terms in Eq. (D.14). Aerodynamic coupling occurs through the right-hand sides of Eqs. (D.12), (D.13), and (D.14). Equations (D.12), (D.13), and (D.14) have been also obtained in Ref. [51] using a Lagrangian approach, and they reduce to the ones in Refs. [45, 46, 40] by neglecting inertial coupling effects. Further details on the derivation of Eqs. (D.12), (D.13), and (D.14) are found in Ref. [42].

D.4 Linearized equations of motion

The nonlinear equations in Subsec. D.3 [Eqs. (D.12), (D.13), and (D.14)] are linearized for small disturbances with respect to a steady maneuver, defined by the trim translational and angular velocities $\mathbf{v}_{\mathsf{G}e}$ and $\boldsymbol{\omega}_e$ and by the corresponding linear aeroelastostatic deflection described by the modal coordinates at equilibrium q_{n_e}. Accordingly, the linearized model is as follows:

$$m\left(\Delta\dot{\mathbf{v}}_{\mathsf{G}} + \boldsymbol{\omega}_e \times \Delta\mathbf{v}_{\mathsf{G}} - \mathbf{v}_{\mathsf{G}e} \times \Delta\boldsymbol{\omega}\right) = \Delta\mathbf{f}_{\mathsf{T}} \tag{D.15}$$

$$\begin{aligned}
&\Delta\dot{\mathbf{J}}\,\boldsymbol{\omega}_e + \mathbf{J}_e\,\Delta\dot{\boldsymbol{\omega}} + \sum_{n,m=1}^{\infty}\mathbf{b}_{nm}q_{n_e}\Delta\ddot{q}_m - \mathbf{J}_e\,\boldsymbol{\omega}_e \times \Delta\boldsymbol{\omega} + \\
&\qquad + \boldsymbol{\omega}_e \times \left(\Delta\mathbf{J}\,\boldsymbol{\omega}_e + \mathbf{J}_e\,\Delta\boldsymbol{\omega} + \sum_{n,m=1}^{\infty}\mathbf{b}_{nm}q_{n_e}\Delta\dot{q}_m\right) = \Delta\mathbf{m}_{\mathsf{G}}
\end{aligned} \tag{D.16}$$

$$\begin{aligned}
&m_n\Delta\ddot{q}_n - \Delta\dot{\boldsymbol{\omega}} \cdot \sum_{m=1}^{\infty}\mathbf{b}_{nm}q_{m_e} - \boldsymbol{\omega}_e \cdot \Delta\mathbf{Y}_n\boldsymbol{\omega}_e + \\
&\qquad - 2\Delta\boldsymbol{\omega} \cdot \mathbf{Y}_{n_e}\boldsymbol{\omega}_e - 2\boldsymbol{\omega}_e \cdot \sum_{m=1}^{\infty}\mathbf{b}_{nm}\Delta\dot{q}_m + k_n\Delta q_n = \Delta f_n
\end{aligned} \tag{D.17}$$

where

$$\begin{aligned}
\mathbf{J}_e &= \mathbf{J}_0 + \sum_{n=1}^{\infty}\left(\mathbf{J}_n + \mathbf{Y}_{n_e}\right)q_{n_e} & \Delta\mathbf{J} &= 2\sum_{n=1}^{\infty}\mathbf{Y}_{n_e}\Delta q_n & \Delta\dot{\mathbf{J}} &= 2\sum_{n=1}^{\infty}\mathbf{Y}_{n_e}\Delta\dot{q}_n \\
\mathbf{Y}_{n_e} &= \mathbf{J}_n + \sum_{m=1}^{\infty}\mathbf{J}_{nm}q_{m_e} & \Delta\mathbf{Y}_n &= \sum_{m=1}^{\infty}\mathbf{J}_{nm}\Delta q_m
\end{aligned} \tag{D.18}$$

Equations (D.15), (D.16), and (D.17) are recast in matrix form by replacing the physical perturbation vectors $\Delta\mathbf{v}_{\mathsf{G}}$, $\Delta\dot{\mathbf{v}}_{\mathsf{G}}$, $\Delta\boldsymbol{\omega}$, $\Delta\dot{\boldsymbol{\omega}}$, $\Delta\mathbf{f}_{\mathsf{T}}$, and $\Delta\mathbf{m}_{\mathsf{G}}$ by the following vectors of their components in the PMA frame:

$$
\begin{aligned}
&\Delta\mathsf{v}_{\mathsf{G}} = \{\Delta u,\, \Delta v,\, \Delta w\}^{\mathsf{T}} && \Delta\omega = \{\Delta p,\, \Delta q,\, \Delta r\}^{\mathsf{T}} \\
&\Delta\mathsf{f}_{\mathsf{T}} = \{\Delta X,\, \Delta Y,\, \Delta Z\}^{\mathsf{T}} = \Delta\mathsf{f}_{\mathsf{A}} + \Delta\mathsf{f}_{\mathsf{W}} && \Delta\mathsf{m}_{\mathsf{G}} = \{\Delta L,\, \Delta M,\, \Delta N\}^{\mathsf{T}} = \Delta\mathsf{m}_{\mathsf{A}}
\end{aligned}
\tag{D.19}
$$

where $\Delta\mathsf{f}_{\mathsf{A}}$ and $\Delta\mathsf{f}_{\mathsf{W}}$ are respectively the perturbations of the aerodynamic and weight force and $\Delta\mathsf{m}_{\mathsf{A}}$ is the perturbation of the aerodynamic moment. Any other physical quantity in Eqs. (D.15), (D.16), and (D.17) is also represented in terms of the vector or matrix of its components in the PMA frame (for instance, the trim angular velocity $\boldsymbol{\omega}_e$ is replaced by the vector of its components ω_e). Equations (D.15), (D.16), and (D.17) are written in concise form as

$$
\mathsf{M}_e \begin{Bmatrix} \Delta\dot{\mathsf{v}}_{\mathsf{G}} \\ \Delta\dot{\omega} \\ \Delta\ddot{\mathsf{q}} \end{Bmatrix} + \mathsf{D}_e \begin{Bmatrix} \Delta\mathsf{v}_{\mathsf{G}} \\ \Delta\omega \\ \Delta\dot{\mathsf{q}} \end{Bmatrix} + \mathsf{K}_e \begin{Bmatrix} \Delta\mathsf{x}_{\mathsf{G}}^{\mathsf{B}} \\ \Delta\theta \\ \Delta\mathsf{q} \end{Bmatrix} = \begin{Bmatrix} \Delta\mathsf{f}_{\mathsf{T}} \\ \Delta\mathsf{m}_{\mathsf{G}} \\ \Delta\mathsf{f}_{\mathsf{E}} \end{Bmatrix}
\tag{D.20}
$$

The quantities

$$
\begin{aligned}
&\Delta\mathsf{q} = \{\Delta q_1,\, \ldots,\, \Delta q_N\}^{\mathsf{T}} && \Delta\mathsf{f}_{\mathsf{E}} = \{\Delta f_1,\, \ldots,\, \Delta f_N\}^{\mathsf{T}} \\
&\Delta\mathsf{x}_{\mathsf{G}}^{\mathsf{B}} = \left\{\Delta x_{\mathsf{G}}^{\mathsf{B}},\, \Delta y_{\mathsf{G}}^{\mathsf{B}},\, \Delta z_{\mathsf{G}}^{\mathsf{B}}\right\}^{\mathsf{T}} && \Delta\theta = \{\Delta\theta_1,\, \Delta\theta_2,\, \Delta\theta_3\}^{\mathsf{T}}
\end{aligned}
\tag{D.21}
$$

are respectively the perturbation vectors of the modal coordinates, generalized forces, center of mass position expressed in the PMAs, and rigid-body rotation about the PMAs. Once the generalized mass matrix $\overline{\mathsf{M}}$, the generalized stiffness matrix $\overline{\mathsf{K}}$, and the matrices

$$
\begin{aligned}
\mathsf{B}_e &:= \begin{bmatrix} \sum_{n=1}^{N} \mathsf{b}_{n1} q_{n_e} & \cdots & \sum_{n=1}^{N} \mathsf{b}_{nN} q_{n_e} \end{bmatrix} & \mathsf{Y}_e &:= 2\begin{bmatrix} \mathsf{Y}_{1_e}\omega_e & \cdots & \mathsf{Y}_{N_e}\omega_e \end{bmatrix} \\
\mathsf{F}_e &:= \begin{bmatrix} \omega_e^{\mathsf{T}} \mathsf{J}_{11}\omega_e & \cdots & \omega_e^{\mathsf{T}} \mathsf{J}_{1N}\omega_e \\ \vdots & \ddots & \vdots \\ \omega_e^{\mathsf{T}} \mathsf{J}_{N1}\omega_e & \cdots & \omega_e^{\mathsf{T}} \mathsf{J}_{NN}\omega_e \end{bmatrix} & \mathsf{G}_e &:= 2\begin{bmatrix} \omega_e^{\mathsf{T}} \mathsf{b}_{11} & \cdots & \omega_e^{\mathsf{T}} \mathsf{b}_{1N} \\ \vdots & \ddots & \vdots \\ \omega_e^{\mathsf{T}} \mathsf{b}_{N1} & \cdots & \omega_e^{\mathsf{T}} \mathsf{b}_{NN} \end{bmatrix}
\end{aligned}
\tag{D.22}
$$

are introduced, the matrices in Eq. (D.20) are written as

$$\begin{aligned}
\mathsf{M}_e &= \begin{bmatrix} m\mathsf{I} & 0 & 0 \\ 0 & \mathsf{J}_e & \mathsf{B}_e \\ 0 & \mathsf{B}_e^{\mathsf{T}} & \overline{\mathsf{M}} \end{bmatrix} \\
\mathsf{D}_e &= \begin{bmatrix} m\hat{\Omega}_e & -m\hat{\mathsf{V}}_{\mathsf{G}e} & 0 \\ 0 & \hat{\Omega}_e\mathsf{J}_e - \hat{\mathsf{H}}_{\mathsf{G}e} & \hat{\Omega}_e\mathsf{B}_e + \mathsf{Y}_e \\ 0 & -\mathsf{Y}_e^{\mathsf{T}} & -\mathsf{G}_e \end{bmatrix} \qquad \text{(D.23)} \\
\mathsf{K}_e &= \begin{bmatrix} 0 & 0 & 0 \\ 0 & 0 & \hat{\Omega}_e\mathsf{Y}_e \\ 0 & 0 & \overline{\mathsf{K}} - \mathsf{F}_e \end{bmatrix}
\end{aligned}$$

where $\hat{\Omega}_e$ and $\hat{\mathsf{V}}_e$ are, respectively, the skew-symmetric matrices associated with the cross product of ω_e and $\mathsf{v}_{\mathsf{G}e}$.

D.5 Small disturbance aerodynamics

Small disturbance aerodynamics is modeled via DLM, which is a potential-flow lifting surface aerodynamic model standardly used in commercial FEM aeroelastic solvers [52]. In these solvers, small disturbance unsteady aerodynamics is described in the frequency domain by the generalized aerodynamic force (GAF) matrix $\mathsf{E} := \mathsf{E}(k; M_\infty)$, where $k := \omega b/U_\infty$ is the reduced frequency, ω is the dimensional Fourier variable, b is the reference half chord, U_∞ is the freestream velocity, and M_∞ the freestream Mach number. In a fully unsteady description, the GAF matrix has a transcendental dependency on the reduced frequency due to lag effects associated with wake dynamics. This makes the linear aeroelastic system integrodifferential, so that it cannot be directly recast in state-space form. However, a state-space representation of the aeroelastic system can be achieved by approximating the GAF matrix by means of polynomials and rational functions of k [48, 53]. Using this approach, the aerodynamic terms on the right-hand side of Eq. (D.20) can be represented as functions of the non-dimensional Laplace variable p as follows [42]:

$$\begin{aligned}\begin{Bmatrix} \Delta\tilde{\mathsf{f}}_{\mathsf{A}} \\ \Delta\tilde{\mathsf{m}}_{\mathsf{G}} \\ \Delta\tilde{\mathsf{f}}_{\mathsf{E}} \end{Bmatrix} = \quad & \frac{1}{2}\,\rho_\infty U_\infty\, b\,(p\bar{\mathsf{A}}_2 + \bar{\mathsf{A}}_1) \begin{Bmatrix} \Delta\tilde{\mathsf{v}}_{\mathsf{G}} \\ \Delta\tilde{\omega} \\ \Delta\tilde{\dot{\mathsf{q}}} \end{Bmatrix} + \\ & q_D\, \bar{\mathsf{A}}_0 \begin{Bmatrix} \Delta\tilde{\mathsf{x}}^{\mathsf{B}}_{\mathsf{G}} \\ \Delta\tilde{\theta} \\ \Delta\tilde{\mathsf{q}} \end{Bmatrix} + q_D\, \bar{\mathsf{C}}\,(p\mathsf{I} - \bar{\mathsf{P}})^{-1}\, \bar{\mathsf{B}} \begin{Bmatrix} \Delta\tilde{\mathsf{x}}^{\mathsf{B}}_{\mathsf{G}} \\ \Delta\tilde{\theta} \\ \Delta\tilde{\mathsf{q}} \end{Bmatrix}\end{aligned} \tag{D.24}$$

where Laplace transforms are denoted by a tilde, $q_D = \rho_\infty U_\infty^2/2$ is the freestream dynamic pressure, and $\bar{\mathsf{A}}_0$, $\bar{\mathsf{A}}_1$, $\bar{\mathsf{A}}_2$, $\bar{\mathsf{B}}$ and $\bar{\mathsf{C}}$ are interpolative matrices for the $(6+N)\times(6+N)$ GAF matrix data obtained from a standard FEM/DLM flutter analysis [52]. The last term in Eq. (D.24) approximates the wake dynamics in terms of a finite number N_a of aerodynamic states [42]

$$\Delta\tilde{\mathsf{a}} := (p\mathsf{I} - \bar{\mathsf{P}})^{-1}\, \bar{\mathsf{B}} \begin{Bmatrix} \Delta\tilde{\mathsf{x}}^{\mathsf{B}}_{\mathsf{G}} \\ \Delta\tilde{\theta} \\ \Delta\tilde{\mathsf{q}} \end{Bmatrix} \tag{D.25}$$

D.6 State-space flexible-aircraft model

A state-space representation of the flexible-aircraft system is obtained from the linearized equations in Subsec. D.4 [Eqs. (D.15), (D.16), and (D.17)] and using the small disturbance finite-state aerodynamic model in Subsec. D.5 [Eqs. (D.24) and (D.25)]. The state-space model has order $[2(6+N)+N_a]$ and is associated to the state-space vector

$$\mathsf{x} = \begin{Bmatrix} \Delta\mathsf{x}_{\mathsf{G}} \\ \Delta\Theta \\ \Delta\mathsf{q} \\ \Delta\mathsf{v}_{\mathsf{G}} \\ \Delta\omega \\ \Delta\dot{\mathsf{q}} \\ \Delta\mathsf{a} \end{Bmatrix} \tag{D.26}$$

where

$$\Delta\mathsf{x}_{\mathsf{G}} = \{\Delta x_{\mathsf{G}},\, \Delta y_{\mathsf{G}},\, \Delta z_{\mathsf{G}}\}^{\mathsf{T}} \qquad \Delta\Theta = \{\Delta\phi,\, \Delta\theta,\, \Delta\psi\}^{\mathsf{T}} \tag{D.27}$$

are the perturbation vectors of the center of mass inertial coordinates and Euler angles.

D.6.1 State-space matrix

The linearized equations in Subsec. D.4 [Eqs. (D.15), (D.16), and (D.17)] are completed with the kinematic equations:

$$\begin{Bmatrix} \Delta\dot{\mathsf{x}}_{\mathsf{G}} \\ \Delta\dot{\Theta} \\ \Delta\dot{\mathsf{q}} \end{Bmatrix} = \mathsf{T}_1 \begin{Bmatrix} \Delta\mathsf{v}_{\mathsf{G}} \\ \Delta\omega \\ \Delta\dot{\mathsf{q}} \end{Bmatrix} = \begin{bmatrix} \mathsf{L}_e & 0 & 0 \\ 0 & \mathsf{T}_e & 0 \\ 0 & 0 & \mathsf{I} \end{bmatrix} \begin{Bmatrix} \Delta\mathsf{v}_{\mathsf{G}} \\ \Delta\omega \\ \Delta\dot{\mathsf{q}} \end{Bmatrix} \tag{D.28}$$

where L_e and T_e are respectively the linearized forms of the transformation matrix from the PMAs to the inertial axes and the matrix relating the Euler angles rates to the angular velocity components expressed in the PMAs. Using Eqs. (D.20), (D.24), and (D.25) and introducing the attitude stiffness matrix K_{W} to project the perturbation of the weight force onto the PMAs [42], the flexible-aircraft model is written in standard state-space form

$$\dot{\mathsf{x}} = \mathsf{A}\,\mathsf{x} \tag{D.29}$$

with state matrix [42]

$$\mathsf{A} = \begin{bmatrix} 0 & \mathsf{T}_1 & 0 \\ -\mathsf{M}^{-1}\mathsf{K} & -\mathsf{M}^{-1}\mathsf{D} & q_D\mathsf{M}^{-1}\bar{\mathsf{C}} \\ \frac{U_\infty}{b}\bar{\mathsf{B}} & 0 & \frac{U_\infty}{b}\bar{\mathsf{P}} \end{bmatrix} \tag{D.30}$$

where

$$\begin{aligned} \mathsf{M} &:= \mathsf{M}_e - \frac{1}{2}\,\rho_\infty b^2 \bar{\mathsf{A}}_2 \\ \mathsf{D} &:= \mathsf{D}_e - \frac{1}{2}\,\rho_\infty U_\infty\, b\, \bar{\mathsf{A}}_1 \\ \mathsf{K} &:= \mathsf{K}_e - q_D \bar{\mathsf{A}}_0 + \mathsf{K}_{\mathsf{W}} \end{aligned}$$

The state vector elements [Eq. D.26] describe the rigid-body motion of the PMA frame (12), structural displacements relative to the PMA frame ($2N$), and finite-state unsteady aerodynamics (N_a). The number of rigid-body state variables can be reduced to 9 in case aircraft flight path is out of interest for stability and response analysis [47] and the effect of the density gradient is neglected.

D.6.2 Gust inputs

In this framework, a quasi-steady gust is considered to have a quasi-uniform velocity profile in space that is given by:

$$\mathbf{v}_g = \sum_{i=1}^{3} v_{g_i}\mathbf{e}_i + \sum_{i=1}^{3} \omega_{g_i}\mathbf{e}_i \times \mathbf{z} \tag{D.31}$$

By projecting the gust velocity over the rigid-body and elastic mode shapes it is possible to rewrite Eq. (D.24) as

$$\left\{\begin{matrix} \Delta\tilde{\mathsf{f}}_{\mathsf{A}} \\ \Delta\tilde{\mathsf{m}}_{\mathsf{G}} \\ \Delta\tilde{\mathsf{f}}_{\mathsf{E}} \end{matrix}\right\} = \frac{1}{2}\,\rho_\infty U_\infty\, b\,(p\bar{\mathsf{A}}_2 + \bar{\mathsf{A}}_1) \left\{\begin{matrix} \Delta\tilde{\mathsf{v}}_{\mathsf{G}} - \tilde{\mathsf{v}}_g \\ \Delta\tilde{\omega} - \tilde{\omega}_g \\ \Delta\dot{\tilde{\mathsf{q}}} \end{matrix}\right\} + q_D\,\bar{\mathsf{A}}_0 \left\{\begin{matrix} \Delta\tilde{\mathsf{x}}^{\mathsf{B}}_{\mathsf{G}} \\ \Delta\tilde{\theta} \\ \Delta\tilde{\mathsf{q}} \end{matrix}\right\} + q_D\,\bar{\mathsf{C}}\,\Delta\tilde{\mathsf{a}} \tag{D.32}$$

where the linear gust velocity is assumed to be as $\tilde{\mathsf{v}}_g = [0 \;\; 0 \;\; \tilde{v}_{g3}]^{\mathsf{T}}$ and the rotational gust velocity as $\tilde{\omega}_g = [0 \;\; 0 \;\; \tilde{\omega}_{g3}]^{\mathsf{T}}$. This allows to represent non-symmetric gust profile with respect to the plane xz (as opposed to [54]). Therefore $\tilde{\mathsf{v}}_g$ and $\tilde{\omega}_g$ are merged in $\tilde{\mathsf{w}}_g$. In such a way $\tilde{\mathsf{w}}_g$ is a six component vector. Once Eq. (D.32) is developed as in Sec. D.6.1, the linearized system is written as

$$\dot{\mathsf{x}} = \mathsf{A}\,\mathsf{x} + \mathsf{B}_g\,\mathsf{u}_g \tag{D.33}$$

where the elements of the input vector $\mathsf{u}_g^{\mathsf{T}}$ are the gust velocity components and their time derivatives as it follows:

$$\mathsf{u}_g = \left\{\begin{matrix} \mathsf{w}_g \\ \dot{\mathsf{w}}_g \end{matrix}\right\} \tag{D.34}$$

and the input matrix is

$$\mathsf{B}_g = -\frac{1}{2}\,\rho_\infty U_\infty\, b \begin{bmatrix} 0 & 0 \\ \mathsf{M}^{-1}\bar{\mathsf{A}}_1^{(1,6)} & \frac{b}{U_\infty}\mathsf{M}^{-1}\bar{\mathsf{A}}_2^{(1,6)} \\ 0 & 0 \end{bmatrix} \tag{D.35}$$

The matrices $\bar{\mathsf{A}}_1^{(1,6)}$ and $\bar{\mathsf{A}}_2^{(1,6)}$ consist, respectively, of the first six columns of $\bar{\mathsf{A}}_1$ and $\bar{\mathsf{A}}_2$.

Bibliography

[1] Balageas, D., Fritzen, C.P., Güemes, A., *Structural Health Monitoring.* ISTE, 2006

[2] Smith, G. C., Clark, R. L., *A crude method of loop-shaping adaptive structures through optimum spatial compensator design.* J. Sound Vib. 247 (3), (2001), pp. 489-508.

[3] Suh, P. M., Chin, A. W., Mavris, D.N., *Virtual Deformation Control of the X-56A Model with Simulated Fiber Optic Sensors.* AIAA Atmospheric Flight Mechanics (AFM) Conference, August 2013, Boston, MA.

[4] Avitabile, P., Pingle, P., *Prediction of full field dynamic strain from limited sets of measured data.* Shock and Vibration 19, (2012), pp 765-785.

[5] Kullaa, J., *Virtual sensing of structural vibrations using dynamic substructuring.* Mechanical Systems and Signal Processing, Vol. 79, (2016), pp. 203-224.

[6] Hwang, J., Kareemb, A., Kim, W., *Estimation of modal loads using structural response.* Journal of Sound and Vibration, Vol. 326, (2009), pp. 522–539.

[7] Papadimitriou, C., Fritzen, C. P., Kraemer, P., Ntotsios, E., *Fatigue predictions in entire body of metallic structures from a limited number of vibration sensors using Kalman filtering.* Struct. Control Health Monit. (2011), 18, pp. 554–573.

[8] Lourens, E., Reynders, E., De Roeck, G., Degrande, G., Lombaert, G., *An augmented Kalman filter for force identification in structural dynamics.* Mechanical Systems and Signal Processing, Vol. 27, (2012), pp. 446–460.

[9] Naets, F., Cuadrado, J., Desmet, W., *Stable force identification in structural dynamics using Kalman filtering and dummy-measurements.* Mechanical Systems and Signal Processing, Vols. 50–51, (2015), pp. 235-248.

[10] Gillijns, S., De Moor, B., *Unbiased minimum-variance input and state estimation for linear discrete-time systems with direct feedthrough.* Automatica, Vol. 43 (2007), pp. 934–937.

[11] Lourens, E., Papadimitriou, C., Gillijns, S., Reynders, E., De Roeck, G., Lombaert, G., *Joint input-response estimation for structural systems based on reduced-order models and vibration data from a limited number of sensors.* Mechanical Systems and Signal Processing, Vol. 29, (2012), pp. 310-327.

[12] Balas, M.J., *Do all linear flexible structures have convergent second-order observer?.* Proceedings of the American Control Conference, Philadelphia, Pennsylvania, June 1998.

[13] Hashemipour, H.R., Laub, A.J., *Kalman filtering for second-order models.* Journal of Guidance, Control, and Dynamics, Vol. 11, No. 2 (1988), pp. 181-186.

[14] Belvin, W.K., *Second-Order State Estimation Experiments Using Acceleration Measurements.* Journal of guidance, control, and dynamics, Vol. 17, No. 1, (1994).

[15] Demetriou, M.A., *Natural second-order observers for second-order distributed parameter systems.* Systems & Control Letters, Vol. 51, (2004), pp. 225-234.

[16] Demetriou, M.A., *Using unknown input observer for robust adaptive fault detection in vector second-order systems.* Mechanical Systems and Signal Processing 19, (2005), pp. 291–309.

[17] Azad, M.M., Mohammadpour, J., Grigoriadis, K.M., *Observer-Type* H_∞ *Filter Design for Structural Systems.* AIAA Guidance, Navigation and Control Conference and Exhibit, Honolulu, Hawaii, 2008.

[18] Hernandez, E.M., *A natural observer for optimal state estimation in second order linear structural systems.* Mechanical Systems and Signal Processing, Vol. 25, (2011), pp. 2938-2947.

[19] Hernandez, E.M., *Optimal model-based state estimation in mechanical and structural systems.* Struct. Control Health Monit., Vol. 20, (2013), pp. 532–543.

[20] Erazo, K., Hernandez, E.M., *A model-based observer for state and stress estimation in structural and mechanical systems: Experimental validation.* Mechanical Systems and Signal Processing 43,(2014), pp. 141–152.

[21] Mallat, S.G., Zhang, G., *Matching Pursuits with Time-Frequency Dictionaries.* IEEE Transactions on Signal Processing, Vol 41, pp. 3397-415

[22] Parvez, S., Gao, Z., *A Wavelet-Based Multiresolution PID Controller.* IEEE Trans. on ind. app., VOL. 41, NO. 2, (2005), pp. 537-543

[23] Bampton, M.C.C., Craig, R.R. Jr., *Coupling of substructures for dynamic analyses.* AIAA Journal, Vol. 6, No. 7 (1968), pp. 1313-1319.

[24] Saltari, F., Dessi, D., Faiella, E., Mastroddi, F., *Load and Deflection Estimation of a Fast Catamaran Towing tank Model via reduced order modeling and Optimal Natural Observer.* Proceeding of International Conference on Noise and Vibration Engineering, Sept. 2018, Leuven, Belgium.

[25] Thomas, G., Davis, M. R., Holloway, D. S., Roberts, T., *The effect of slamming and whipping on the fatigue life of a high-speed catamaran.* Australian Journal of Mechanical Engineering, 3:2, (2006), pp. 165-174.

[26] https://www.lockheedmartin.com/en-us/products/X-56A.html

[27] Gèradin,M., Rixen, D., *Mechanical vibrations: theory and application to structural dynamics.* John Wiley and Sons Ltd.

[28] Maes, K., Smyth, A.W., De Roeck, G., Lombaert, G., *Joint input-state estimation in structural dynamics.* Mechanical Systems and Signal Processing, Vols. 70-71, (2016), pp. 445-466.

[29] Kalman, R.E., Bucy, R.S., *New results in linear filtering and prediction theory.* J. Basic Engineering Transactions on ASME, Series D 83 (3), pp 95 – 108.

[30] Shimkin, N., *The Continuous-Time Kalman Filter.* Lecture Notes, Fall 2009

[31] *Nonlinear Optimization.* Matlab & Simulink

[32] *MSC.Nastran Design and Optimization User's Guide.* MSC Software, Newport Beach, CA, (2012)

[33] Dessi, D., Faiella, E., Geiser, J., Alley, E., Dukes, J., *Design, assessment and testing of a fast catamaran for FSI investigation.* 31st Symposium on Naval Hydrodynamics Monterey, California, 11-16 September 2016.

[34] Peeters, B., Van der Auweraer, H., Guillaume, P., Leuridan, J., *The PolyMAX Frequency-Domain Method: A New Standard for Modal Parameter Estimation?.* Shock and Vibration, vol. 11, no. 3-4, pp. 395-409, 2004 .

[35] Dessi, D., Faiella, E., Geiser, J., Alley, E., Dukes, J., *Design and structural testing of a physical model for wetdeck slamming analysis.* Progress in the Analysis and Design of Marine Structures: Proceedings of the 6th International Conference on Marine Structures, Lisbon, 2017.

[36] Hasselmann K., Barnett, T.P., Bouws, E., Carlson, H., Cartwright, D.E., Enke, K., Ewing, J.A., Gienapp, H., Hasselmann, D.E., Kruseman, P., Meerburg, A., Mller, P. Olbers, D.J., Richter, K., Sell, W., Walden, H., *Measurements of wind-wave growth and swell decay during the Joint North Sea Wave Project (JONSWAP).* Ergnzungsheft zur Deutschen Hydrographischen Zeitschrift Reihe, A(8) (Nr. 12), p.95, 1973..

[37] Iliopoulos, A.N., Weijtjens, W., Van Hemelrijck, D., Devriendt, C., *Prediction of dynamic strains on a monopile offshore wind turbine using virtual sensor.* J. Phys.: Conf. Ser., Vol. 628, (2015), conf. 1.

[38] Miner, M.A., *Cumulative damage in fatigue.* Journal of Applied Mechanics, Vol 12, (1945)

[39] Downing, S.D., Socie, D.F., *Simple rainflow counting algorithms.* International Journal of Fatigue, Vol 4, (1982), pp. 31-40.

[40] Schmidt, D. K. *Stability Augmentation and Active Flutter Suppression of a Flexible Flying-Wing Drone.* Journal of Guidance, Control, and Dynamics, Vol. 39, No. 3, 2016, pp. 409–422.

[41] Burnet, E.L., Atkinson, C., Beranek, J., Sibbit, B., Holm-Hansen, B., Nicolai, L., *NDOF Simulation Model for Flight Control Development with Flight Test Correlation.* AIAA Paper 2010-7780, AIAA Modeling and Simulation Technologies Conference, 2 - 5 August 2010, Toronto, Ontario Canada.

[42] Saltari, F., Riso, C., De Matteis, G., Mastroddi, F., *Finite-Element Based Modeling for Flight Dynamics and Aeroelasticity of Flexible Aircraft.* Journal of Aircraft, Vol. 54, No. 6 (2017), pp. 2350-2366.

[43] daubechies, I., *Ten lectures on Wavelets.* CBMS-NSF Regional Conference Series in Applied Mathematics, 1992

[44] Kölzow, D., *Wavelets. A tutorial and a bibliography.* Workshop di Teoria della Misura e Analisi Reale, Grado (It), 1993

[45] Waszak, M. R., and Schmidt, D. K., *Flight Dynamics of Aeroelastic Vehicles.* Journal of Aircraft, Vol. 25, No. 6, 1988, pp. 563–571.

[46] Schmidt, D. K., and Raney, D. L., *Modeling and Simulation of Flexible Flight Vehicles.* Journal of Guidance, Control, and Dynamics, Vol. 24, No. 3, 2001, pp. 539–546.

[47] Etkin, B., *Dynamics of Atmospheric Flight.* Wiley, New York, 1972.

[48] Karpel, M., *Design for Active Flutter Suppression and Gust Alleviation Using State-Space Aeroelastic Modeling.* Journal of Aircraft, Vol. 19, No. 3, 1982, pp. 221-227.

[49] Morino, L., and Noll, R. B., *FCAP - A New Toll for the Performance and Structural Analysis for Complex Flexible Aircraft with Active Control.* Computers and Structures, Vol. 7, 1977, pp. 275–282.

[50] Milne, R. D., *Dynamics of the Deformable Aeroplane, Parts I and II.* Her Majesty's Stationery Office, Repts. and Memoranda 3345, London, Sept. 1962.

[51] Buttrill, C. S., Zeiler, T. A., and Arbuckle, P. D., *Nonlinear Simulation of a Flexible Aircraft in Maneuvering Flight.* AIAA Paper 87-2501-CP, AIAA Flight Simulation Technologies Conference, August 1987, Monterey, CA.

[52] Rodden, W. P., Johnson, E. H., *MSC.Nastran Aeroelastic Analysis User's Guide*, MSC.Software Corporation, 2010.

[53] Gennaretti, M., and Mastroddi, F., *A Study of Reduced-Order Models for Gust Response Analysis of Flexible Fixed Wings.* Journal of Aircraft, Vol. 41, No. 2, 2004, pp. 304–313.

[54] Hoblit, F.M., *Gust Loads on aircraft: Concepts and applications.* AIAA Education series, 1988.

Acknowledgements

After this three-years-period I feel I have considerably enriched my cultural baggage and I owe a lot to Daniele Dessi and Franco Mastroddi for this. I am also glad to consider them much more than just phD advisors. Although the topics addressed in Michigan were not included in this thesis, I very much have to thank Professor Collette for introducing me to the world of Bayesian networks and because in that environment I have learned things that I absolutely want to exploit in my next steps in the field of research. This work has been partially supported by the U. S. Office of Naval Research (ONR) for providing data useful for practical application of the proposed developments. Finally, I want to thank my parents for all of their special support.